Validity of Hydrostatic Equilibrium in Mass Estimates of Simulated Galaxy Clusters

Daichi Suto

Department of Physics, Graduate School of Science,
The University of Tokyo

January 2013

Abstract

Clusters of galaxies are among the most important sources of astrophysical and cosmological information especially on the formation history of the large scale structure and the estimates of cosmological parameters. Among others, mass of clusters is the most fundamental quantities. The most conventional method to estimate mass is based on X-ray observations of the intracluster medium (ICM) combined with the assumption that the ICM is in hydrostatic equilibrium (HSE) with the total gravity of the cluster. It is unlikely, however, that the HSE assumption strictly holds, especially for unrelaxed clusters given their on-going dynamical evolution. Therefore it is important to examine the validity of the HSE assumption, which has been mostly assumed just for simplicity.

In this thesis, we examine the validity of HSE using simulated clusters taken from a cosmological hydrodynamical simulation and a SPH simulation. First, we focus on the difference between the true mass and the mass estimated under the HSE assumption (the HSE mass). We define and evaluate several effective mass terms corresponding to the Euler equations of the gas dynamics, and quantify the degree of the validity of HSE in terms of the mass estimate. We find that the HSE mass deviates from the true mass by up to $\sim$ 30 %. We demonstrate that the overall gravity of the cluster is balanced by the thermal gas pressure gradient and the gas acceleration term and that the inertial term in the Euler equations makes a smaller contribution to the total mass.

Since observables in X-ray observations are projected properties of ICM, the mass constructed from them is further biased in addition to the intrinsic violation of HSE. To investigate this problem, we calculate the surface brightness and spectroscopic-like temperature using the simulation data and find density and temperature profiles which reproduce the observables by fitting. Then the mass constructed from the best-fit profiles is compared with the three-dimensional HSE mass. We show that the two-dimensionality of the observables only slightly affects the mass estimates. If, however, a simulated cluster has big substructures in outer regions, the mass of the cluster is underestimated at large radii.

Contents

Chapter 1

INTRODUCTION

Clusters of galaxies are important sources of various cosmological and astrophysical information especially on the formation history of the large scale structure and the estimates of cosmological parameters (Allen et al., 2011, for a recent review). Among others, mass of clusters is one of the most fundamental quantities in virtually all studies. The most conventional method is based on X-ray observations of the intracluster medium (ICM) combined with the assumption that the ICM is in hydrostatic equilibrium (HSE) with the total gravity of the cluster (We call the mass estimated by this method "the HSE mass"). It is unlikely, however, that the HSE assumption strictly holds, especially for unrelaxed clusters given their on-going dynamical evolution. Therefore it is important to examine the validity of the HSE assumption, which has been mostly assumed just for simplicity. The quantitative analysis of its validity and limitation is directly related to the applicability to the future scientific opportunities, including upcoming X-ray missions such as extended Röntgen Survey with Imaging Telescope Array[1] (eROSITA) and ASTRO-H[2], and observations of the Sunyaev-Zel'dovich effect performed by Atacama Cosmology Telescope[3] (ACT) and South Pole Telescope[4] (SPT).

The validity of the HSE assumption for observed clusters may be examined in a straightforward fashion by comparison of the HSE mass with the cluster mass estimated by other methods. In this respect, gravitational lensing is particularly suited because it directly probes the total gravitational mass without any assumption on dynamical states of dark matter. On the other hand, the lensing observations require a high angular resolution of the background galaxy images and are feasible only for a limited number of clusters located at $z \lesssim 0.5$. In addition, the estimated lensing mass corresponds to the cylindrical mass along the line of sight, and may include an extra contribution not associated with the cluster itself. Previous studies (e.g., Mahdavi et al., 2008; Zhang et al., 2008, for recent ones) show that the HSE mass is smaller by approximately 20 percent on average than the lensing mass, suggesting either HSE or lensing, or even both, should be systematically biased.

Another method to examine the validity of the HSE assumption that we pursue in this paper is to use numerical simulations, which enable us to make a detailed and critical comparison of the simulated data against the model prediction. Therefore we can locate the origin of systematic bias, if any, of the HSE assumption. This is useful because we may be able to apply the correction to the observational data eventually.

Of course there are a number of previous studies of HSE using simulated clusters, but their

[1] http://www.mpe.mpg.de/eROSITA
[2] http://astro-h.isas.jaxa.jp
[3] http://www.princeton.edu/act
[4] http://pole.uchicago.edu

results do not seem to be converged. For instance, let us focus on a couple of recent papers (Fang et al., 2009; Lau et al., 2009) that studied systematic errors in the HSE mass using the *same* set of 16 clusters simulated by Nagai et al. (2007). Fang et al. (2009) analyzed the gas particle data on the basis of the Euler equations, and evaluated the *effective* mass terms corresponding to several different terms in the equations. Lau et al. (2009) performed basically the same analysis, but used the Jeans equations instead of the Euler equations despite the fact that they considered the gas particles in the simulated clusters. Both reached the similar conclusion that the HSE mass underestimates the true mass of clusters systematically by $\sim$ 10–20 %. Nevertheless their physical interpretations of the origin of the bias are very different; Fang et al. (2009) claimed that the coherent rotation of gas plays a significant role as an additional support against the gravity, while Lau et al. (2009) concluded that the random gas motion is responsible for the departure from HSE, and the gas rotation makes a relatively negligible contribution.

The above discussion is on the validity of HSE using *three-dimensional* simulation data. In real observations, mass of clusters is estimated from *two-dimensional* observables. There can be systematic biases in mass estimates even if uncertainties from observational apparatuses are removed.

The purpose of this thesis is to investigate the validity using a hydrodynamical simulation by Cen (2012) and a SPH simulation by Dolag et al. (2009). First, we focus on intrinsic differences between the true mass and the HSE mass. In particular, we compare the two different analysis formulations adopted by Fang et al. (2009) and Lau et al. (2009), and argue that the Euler equations, rather than the Jeans equations modified by a gas pressure gradient term (Rasia et al., 2004; Lau et al., 2009), should be used in analyzing the gas dynamics. Next, we investigate biases in mass estimates from two-dimensional observables.

The rest of this thesis is organized as follows. We review structure formation in the universe and X-ray observations of galaxy clusters in Chapter 2 and 3, respectively. In these chapters, we summarize what roles galaxy clusters play in cosmology and astrophysics. In Chapter 4, we explain what kinds of simulations are used in this study. Using these simulations, we discuss in Chapter 5 the validity of hydrostatic equilibrium in three-dimensional space. In Chapter 6, we investigate biases in mass construction from two-dimensional mock observables combined with the results in Chapter 5. Finally we summarize the results and make a conclusion in Chapter 7.

Chapter 2

STRUCTURE FORMATION IN THE UNIVERSE

2.1 Background Universe

2.1.1 Friedmann-Robertson-Walker Model

In order to understand the behavior of cosmological fluctuations that dictates the evolution of clusters of galaxies. We briefly summarize the homogeneous and isotropic universe model in this section.

The cosmological principle states that at every point in the universe, an observer exists for whom the universe appears isotropic. We define comoving coordinates x^i as ones that move along with such an observer. Then the physical length is given by $a(t)x^i$, where $a(t)$ is called the scale factor. The metric of a homogeneous and isotropic universe is given by the Friedmann-Lemaître-Robertson-Walker metric:

$$ds^2 = -dt^2 + a^2(t)\left[dx^2 + S_K(x)\left(d\theta^2 + \sin^2\theta d\varphi^2\right)\right], \tag{2.1}$$

where

$$S_K(x) = \begin{cases} \dfrac{\sinh\sqrt{-K}x}{\sqrt{-K}} & ; \quad (K<0) \\ x & ; \quad (K=0) \\ \dfrac{\sin\sqrt{K}x}{\sqrt{K}} & ; \quad (K>0) \end{cases}, \tag{2.2}$$

and K is the curvature of the universe. Here $a(t)$ is normalized to unity at the present time t_0.

Through the Einstein equations, one obtains equations governing the dynamics of $a(t)$ in a perfect fluid of density ρ and pressure p as

$$\left(\frac{\dot{a}}{a}\right)^2 + \frac{K}{a^2} = \frac{8\pi G}{3}\rho + \frac{\Lambda}{3}, \tag{2.3}$$

$$\frac{\ddot{a}}{a} = -\frac{4\pi G}{3}(\rho + 3p) + \frac{\Lambda}{3}, \tag{2.4}$$

$$\dot{\rho} + 3\frac{\dot{a}}{a}(\rho + p) = 0, \tag{2.5}$$

where Λ is the cosmological constant. Equation (2.3) is called the Friedmann equation. Note that one of the above three equations can be derived from the other two.

Assume a matter component that obeys the time-independent equation of state:

$$p = w\rho, \tag{2.6}$$

then Equation (2.5) yields

$$\rho \propto a^{-3(1+w)} \quad (w \neq -1). \tag{2.7}$$

Now we consider some specific cases.

(a) Non-relativistic matter component

Non-relativistic matter has pressure much less than its mass energy: $p \ll \rho$, hence approximately given by

$$w = 0, \quad \rho_m \propto a^{-3}. \tag{2.8}$$

(b) Radiation component

The pressure of a relativistic component is a third of its energy density, $p = \rho/3$. Therefore

$$w = \frac{1}{3}, \quad \rho_r \propto a^{-4}. \tag{2.9}$$

(c) Cosmological constant

The cosmological constant can be regarded as a component whose density and pressure are given by

$$\rho = \frac{\Lambda}{8\pi G}, \quad p = -\frac{\Lambda}{8\pi G}, \tag{2.10}$$

which is equivalent to

$$w = -1, \quad \rho_\Lambda = \text{const.} \tag{2.11}$$

The standard model of the universe identifies the cosmological constant with the so-called dark energy.

Hereafter we take into account only the above three components.

2.1.2 Cosmological Parameters

We introduce the Hubble parameter H:

$$H = \frac{\dot{a}}{a}, \tag{2.12}$$

which describes the expansion (or contraction) rate of the universe. Next we define the critical density as the mean density in the flat universe ($K = 0$):

$$\rho_c = \frac{3H^2}{8\pi G}. \tag{2.13}$$

Using H and ρ_c, Equation (2.3) is rewritten as

$$1 = \Omega_m + \Omega_r + \Omega_\Lambda + \Omega_K, \tag{2.14}$$

where

$$\Omega_m = \frac{\rho_m}{\rho_c}, \quad \Omega_r = \frac{\rho_r}{\rho_c}, \quad \Omega_\Lambda = \frac{\rho_\Lambda}{\rho_c} \tag{2.15}$$

are the density parameters of matter, radiation and dark energy, respectively, and

$$\Omega_K = -\frac{K}{3H^2} \tag{2.16}$$

is the curvature parameter. Observations suggest (e.g. Hinshaw et al., 2012)

$$H_0 \simeq 70 \quad \text{km s}^{-1}\ \text{Mpc}^{-1}, \tag{2.17}$$

$$\Omega_{m,0} \simeq 0.28, \quad \Omega_{r,0} \simeq 0, \quad \Omega_{\Lambda,0} \simeq 0.72, \quad \Omega_{K,0} \simeq 0, \tag{2.18}$$

where the subscript '0' denotes the values of the parameters at the present time t_0. It is conventional to use the dimensionless Hubble constant h defined through

$$H_0 = 100h \quad \text{km s}^{-1}\ \text{Mpc}^{-1}. \tag{2.19}$$

Hereafter we neglect the radiation component. In this case, the Friedmann equation (2.3) is

$$H = H_0\sqrt{\Omega_{m,0}a^{-3} + \Omega_{\Lambda,0} + (1 - \Omega_{m,0} - \Omega_{\Lambda,0})a^{-2}}. \tag{2.20}$$

2.1.3 Models of the Universe

Here we show a few representative models of the universe with specific values of Ω_m and Ω_Λ.

(a) Einstein-de Sitter universe: $\Omega_m = 1, \Omega_\Lambda = 0$

$$a = \left(\frac{3}{2}H_0 t\right)^{2/3} \tag{2.21}$$

$$H = \frac{2}{3t} \tag{2.22}$$

$$\rho = \frac{1}{6\pi G t^2} \tag{2.23}$$

(b) Friedmann universe: $\Omega_\Lambda = 0$

$$\left.\begin{aligned} a &= \frac{\Omega_{m,0}}{2(1-\Omega_{m,0})}(\cosh\eta - 1) \\ H_0 t &= \frac{\Omega_{m,0}}{2(1-\Omega_{m,0})^{3/2}}(\sinh\eta - \eta) \end{aligned}\right\} \quad ; \quad (\Omega_{m,0} < 1) \tag{2.24}$$

$$\left.\begin{aligned} a &= \frac{\Omega_{m,0}}{2(\Omega_{m,0}-1)}(1 - \cos\eta) \\ H_0 t &= \frac{\Omega_{m,0}}{2(\Omega_{m,0}-1)^{3/2}}(\eta - \sin\eta) \end{aligned}\right\} \quad ; \quad (\Omega_{m,0} > 1) \tag{2.25}$$

(c) Flat universe: $\Omega_m + \Omega_\Lambda = 1$

$$a = \begin{cases} \left(\dfrac{\Omega_{m,0}}{1-\Omega_{m,0}}\right)^{1/3} \sinh^{2/3}\left(\dfrac{3}{2}H_0 t\sqrt{1-\Omega_{m,0}}\right) & ; \quad (\Omega_{m,0} < 1) \\ \left(\dfrac{\Omega_{m,0}}{\Omega_{m,0}-1}\right)^{1/3} \sin^{2/3}\left(\dfrac{3}{2}H_0 t\sqrt{\Omega_{m,0}-1}\right) & ; \quad (\Omega_{m,0} > 1) \end{cases} \tag{2.26}$$

2.2 Evolution Equations of Density Fluctuations

In this section we consider a multi component perfect fluid. In Newtonian dynamics, the motion of one of the components is governed by the continuity equation and the Euler equations:

$$\frac{\partial \rho}{\partial t} + \nabla \cdot (\rho \boldsymbol{u}) = 0, \tag{2.27}$$

$$\frac{\partial \boldsymbol{u}}{\partial t} + (\boldsymbol{u} \cdot \nabla)\boldsymbol{u} = -\frac{1}{\rho}\nabla p - \nabla \phi, \tag{2.28}$$

where u is the Eulerian velocity. The gravitational potential ϕ is related to the total density $\rho_{\rm tot}$ and pressure $p_{\rm tot}$ in the system through the Poisson equation:

$$\triangle \phi = 4\pi G(\rho_{\rm tot} + 3p_{\rm tot}). \tag{2.29}$$

In order to investigate the behavior of cosmological fluctuations, we rewrite the above equations in comoving coordinates. Let physical and comoving coordinates be $\boldsymbol{r}$ and $\boldsymbol{x}$. They are related as

$$\boldsymbol{r} = a\boldsymbol{x}. \tag{2.30}$$

Then the velocity $\boldsymbol{u} = \dot{\boldsymbol{r}}$ is rewritten as

$$\boldsymbol{u} = \dot{a}\boldsymbol{x} + \boldsymbol{v}, \tag{2.31}$$

where we defined

$$\boldsymbol{v} = a\dot{\boldsymbol{x}} \tag{2.32}$$

as the peculiar velocity and $\dot{a}\boldsymbol{x}$ is interpreted as a change in motion due to the cosmic expansion. Derivatives and the potential are transformed as

$$\frac{\partial}{\partial t} \to \frac{\partial}{\partial t} - \frac{\dot{a}}{a}\boldsymbol{x} \cdot \nabla, \quad \nabla \to \frac{1}{a}\nabla \tag{2.33}$$

and

$$\phi \to \phi + \frac{1}{2}a\ddot{a}x^2, \tag{2.34}$$

where the inertial force is incorporated in the potential. Using the above results, the continuity, Euler and Poisson equations are finally rewritten as

$$\frac{\partial \rho}{\partial t} + 3\frac{\dot{a}}{a}\rho + \frac{1}{a}\nabla \cdot (\rho \boldsymbol{v}) = 0, \tag{2.35}$$

$$\frac{\partial \boldsymbol{v}}{\partial t} + \frac{\dot{a}}{a}\boldsymbol{v} + \frac{1}{a}(\boldsymbol{v} \cdot \nabla)\boldsymbol{v} = -\frac{1}{a\rho}\nabla p - \frac{1}{a}\nabla \phi \tag{2.36}$$

and

$$\triangle \phi = 4\pi G a^2(\rho_{\rm tot} - \bar{\rho}_{\rm tot} + 3p_{\rm tot} - 3\bar{p}_{\rm tot}), \tag{2.37}$$

where $\bar{\rho}_{\rm tot}$ and $\bar{p}_{\rm tot}$ are the mean density and pressure which show up in the Friedmann equation:

$$\frac{\ddot{a}}{a} = -\frac{4\pi G}{3}(\bar{\rho}_{\rm tot} + 3\bar{p}_{\rm tot}). \tag{2.38}$$

Now we consider fluctuations in density and pressure of a specific component:

$$\rho(\boldsymbol{x}, t) = \bar{\rho}[1 + \delta(\boldsymbol{x}, t)], \tag{2.39}$$

$$p(\boldsymbol{x},t) = \bar{p} + \delta p(\boldsymbol{x},t)). \tag{2.40}$$

Substituting them into the continuity and Euler equations, one obtains

$$\frac{\partial \delta}{\partial t} + \frac{1}{a}\nabla[(1+\delta)\boldsymbol{v}] = 0, \tag{2.41}$$

$$\frac{\partial \boldsymbol{v}}{\partial t} + \frac{\dot{a}}{a}\boldsymbol{v} + \frac{1}{a}(\boldsymbol{v}\cdot\nabla)\boldsymbol{v} = -\frac{\nabla \delta p}{a\bar{\rho}(1+\delta)} - \frac{1}{a}\nabla\phi \tag{2.42}$$

and

$$\triangle\phi = 4\pi G a^2(\bar{\rho}_{\rm tot}\delta_{\rm tot} + 3\delta p_{\rm tot}). \tag{2.43}$$

For simplicity we consider small amplitude fluctuations. Combining Equations (2.41) and (2.42) and dropping off non-linear terms, one obtains

$$\frac{\partial^2 \delta}{\partial t^2} + 2\frac{\dot{a}}{a}\frac{\partial \delta}{\partial t} = \frac{\triangle \delta p}{a^2\bar{\rho}} + 4\pi G(\bar{\rho}\delta_{\rm tot} + 3\delta p_{\rm tot}). \tag{2.44}$$

This is the basic equation for the linear evolution of non-relativistic density fluctuations.

2.3 Jeans Instability

We assume that there is no fluctuations in entropy S of the universe and the pressure fluctuation can be written as

$$\delta p = \left(\frac{\partial p}{\partial \rho}\right)_S \bar{\rho}\delta = c_s^2\bar{\rho}\delta, \tag{2.45}$$

where c_s is the sound speed of the fluid. We also assume that fluctuations of other components are negligible. Then Equation (2.44) is

$$\frac{\partial^2 \delta}{\partial t^2} + 2\frac{\dot{a}}{a}\frac{\partial \delta}{\partial t} - \left(4\pi G\bar{\rho}\delta + \frac{c_s^2}{a^2}\triangle\delta\right) = 0. \tag{2.46}$$

If we Fourier transform the density fluctuation $\delta(\boldsymbol{x},t)$ as

$$\delta(\boldsymbol{x},t) = \frac{1}{(2\pi)^3}\int d^3k\ \tilde{\delta}(\boldsymbol{k},t)e^{i\boldsymbol{k}\cdot\boldsymbol{x}}, \tag{2.47}$$

the Fourier component $\tilde{\delta}(\boldsymbol{k},t)$ obeys the following equation:

$$\frac{\partial^2 \tilde{\delta}}{\partial t^2} + 2\frac{\dot{a}}{a}\frac{\partial \tilde{\delta}}{\partial t} - \left(4\pi G\bar{\rho} - \frac{c_s^2k^2}{a^2}\right)\tilde{\delta} = 0. \tag{2.48}$$

For simplicity we ignore the expansion of the universe for a while :

$$\frac{\partial^2 \tilde{\delta}}{\partial t^2} + \frac{c_s^2}{a^2}(k^2 - k_J^2)\tilde{\delta} = 0, \tag{2.49}$$

where

$$k_J = \frac{a}{c_s}\sqrt{4\pi G\bar{\rho}} \tag{2.50}$$

is the Jeans wavenumber. If $k > k_J$, $\tilde{\delta}$ oscillates and does not grow. If $k < k_J$, $\tilde{\delta}$ grows. The cosmic expansion behaves as a friction that prevents the gravitational contraction.

If we define the Jeans wavelength which corresponds to the Jeans wavenumber as

$$\lambda_J = a\frac{2\pi}{k_J} = c_s\sqrt{\frac{\pi}{G\bar{\rho}}}, \tag{2.51}$$

the Jeans mass

$$M_J = \frac{4\pi}{3}\bar{\rho}\left(\frac{\lambda_J}{2}\right)^3 = \frac{c_s^3}{6}\sqrt{\frac{\pi^5}{G^3\bar{\rho}}} \tag{2.52}$$

gives a measure of the minimum mass which can gravitationally grow.

2.4 Growth of Density Fluctuations

A density fluctuation with a larger scale than the Jeans scale obeys the following equation:

$$\left[\frac{d^2}{dt^2} + 2\frac{\dot{a}}{a}\frac{d}{dt} - 4\pi G\rho\right]\delta = 0. \tag{2.53}$$

This holds in both the real and Fourier spaces. From the Friedmann equations without relativistic components, one finds

$$\left[\frac{d^2}{dt^2} + 2\frac{\dot{a}}{a}\frac{d}{dt} - 4\pi G\rho\right]\dot{a} = 0. \tag{2.54}$$

Therefore $H = \dot{a}/a$ is one of the solutions of the equation (2.53):

$$D_- \propto H(t). \tag{2.55}$$

Since the Hubble parameter decreases with time, D_- corresponds to the decaying mode. The other solution is found from the general theory of second-order linear differential equations:

$$D_+ \propto H\int_0^a \frac{da}{a^3H^3}. \tag{2.56}$$

This solution increases with time and is often called the growing mode or the linear growth rate. The linear growth rate can be rewritten as

$$D_+ = \frac{5}{2}a\Omega_m\int_0^1 \frac{dx}{(\Omega_m/x + \Omega_\Lambda x^2 + 1 - \Omega_m - \Omega_\Lambda)^{3/2}}, \tag{2.57}$$

where the proportional coefficient is chosen so that $D_+ \to a$ as $a \to 0$. Let us consider some specific cases.

(a) Einstein-de Sitter universe

For an Einstein-de Sitter universe, the solution for Equation (2.57) can be easily found:

$$D_+ = a \propto t^{2/3}. \tag{2.58}$$

Therefore the time-dependence of the growing mode D_+ is the same as that of the scale factor a. We may add the decaying mode is proportional to the inverse of the time:

$$D_- \propto t^{-1}. \tag{2.59}$$

(b) Friedmann universe

For a universe with $\Omega_\Lambda = 0$,

$$D_+ = \frac{5}{2}\frac{a\Omega_m}{1-\Omega_m} \cdot \begin{cases} \dfrac{1+2\Omega_m}{1-\Omega_m} - \dfrac{3\Omega_m}{(1-\Omega_m)^{3/2}} \tanh^{-1}\sqrt{1-\Omega_m} & (\Omega_m < 1) \\ \dfrac{1+2\Omega_m}{\Omega_m - 1} - \dfrac{3\Omega_m}{(\Omega_m-1)^{3/2}} \tan^{-1}\sqrt{\Omega_m - 1} & (\Omega_m > 1) \end{cases} \tag{2.60}$$

(c) Flat universe

For a universe with $\Omega_m > 0$ and $\Omega_m + \Omega_\Lambda = 1$, we define $\chi = \Omega_m^{-1} - 1$ and substitute

$$x = \left(\frac{1-t}{1+\chi t}\right)^{1/3} \tag{2.61}$$

into Equation (2.57), resulting in

$$D_+ = \frac{5}{6} a \int_0^1 dt\ (1-t)^{-1/6}(1+\chi t)^{-1/3}. \tag{2.62}$$

Using the formula for Gauss's hypergeometric function ${}_2F_1(a,b,c;z)$:

$${}_2F_1(a,b,c;z) = \frac{\Gamma(c)}{\Gamma(a)\Gamma(c-a)} \int_0^1 t^{a-1}(1-t)^{c-a-1}(1-zt)^{-b} \tag{2.63}$$

for $|z| < 1$, one finds

$$D_+ = a\,{}_2F_1\left(1, \frac{1}{3}, \frac{11}{6}; -\chi\right), \tag{2.64}$$

where the domain of χ is analytically continued to $\chi \geq 1$.

Figure 2.1 shows the linear growth rates for the above three cases as functions of the scale factor a.

In general, the density fluctuation can be written in the following form:

$$\delta(\boldsymbol{x}, t) = D(t)\delta(\boldsymbol{x}, t_0) + \text{decaying mode}, \tag{2.65}$$

where $D(t) = D_+(t)/D_+(t_0)$ is the linear growth rate normalized at the present time.

2.5 Spherical Collapse Model

The spherical collapse model is a simple model to describe the non-linear growth of fluctuations. For simplicity, we consider the Einstein-de Sitter universe. Assume a sphere of constant mass M and time-varying radius $r(t)$ starts to expand from $r = 0$ at $t = 0$, then its motion is described by the following equation:

$$\frac{d^2 r}{dt^2} = -\frac{GM}{r^2}. \tag{2.66}$$

Integrating this over time, one obtains

$$\frac{1}{2}\left(\frac{dr}{dt}\right)^2 - \frac{GM}{r} = E, \tag{2.67}$$

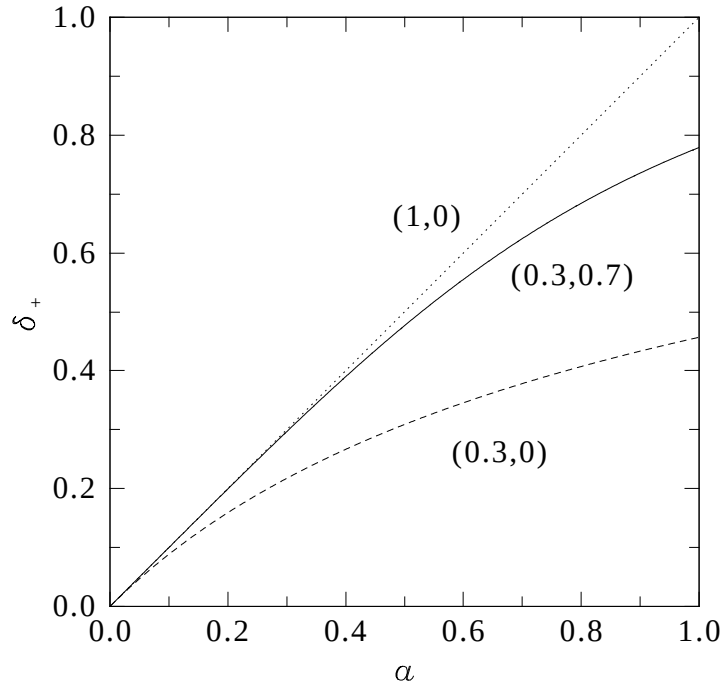

Figure 2.1: The linear growth rates δ_+ for three sets of values of density parameters $(\Omega_{m,0}, \Omega_{\Lambda,0})$ are shown as functions of the scale factor a. For dotted, dashed and solid lines, $(\Omega_{m,0}, \Omega_{\Lambda,0})$ are $(1,0)$, $(0.3,0)$ and $(0.3,0.7)$, respectively.

where E is the energy of the system. If $E < 0$, the expansion stops at some epoch point, and the sphere starts to collapse. Equation (2.67) has a parametric solution:

$$\begin{aligned} r &= \frac{GM}{-2E}(1-\cos\theta) = A(1-\cos\theta) \\ t &= \frac{GM}{(-2E)^{3/2}}(\theta-\sin\theta) = B(\theta-\sin\theta). \end{aligned} \tag{2.68}$$

Since the density of the sphere and the cosmic mean density are given by

$$\rho = \frac{3M}{4\pi r^3}, \quad \bar{\rho} = \frac{1}{6\pi G t^2}, \tag{2.69}$$

the density fluctuation is

$$\delta = \frac{\rho}{\bar{\rho}} - 1 = \frac{9GMt^2}{2r^3} - 1 = \frac{9}{2}\frac{(\theta-\sin\theta)^2}{(1-\cos\theta)^3} - 1. \tag{2.70}$$

When $\theta = \pi$, the sphere *turns around*. At this time,

$$t_t = \pi B, \quad r_t = 2A \tag{2.71}$$

and the density fluctuation is

$$\delta_t = \frac{9\pi^2}{16} \simeq 4.55. \tag{2.72}$$

The subscript t denotes the values at the turn-around time. When $\theta = 2\pi$, the sphere *collapses*, i.e., $r(t)$ becomes 0. At this time,

$$t_c = 2\pi B. \tag{2.73}$$

The subscript c denotes the values at the collapse time.

The virial theorem suggests

$$\langle U \rangle_t = \langle K \rangle_v + \langle U \rangle_v = \frac{1}{2} \langle U \rangle_v, \tag{2.74}$$

where $\langle U \rangle$ and $\langle K \rangle$ are the time averages of the potential and kinetic energy of the system and the subscript v denotes the values at the time when the system is virialized. Since the potential is proportional to r^{-1}, one finds

$$r_v = \frac{1}{2} r_t. \tag{2.75}$$

If we identify the virial time with the collapse time in the spherical collapse model, then

$$\delta_c = \frac{3M}{4\pi r_v^3 \rho_c} - 1 = 18\pi^2 - 1 \simeq 177. \tag{2.76}$$

Next we expand t and $r(t)$ for small θ:

$$\begin{aligned} r &= \frac{A}{2}\theta^2 + \mathcal{O}(\theta^4), \\ t &= \frac{B}{6}\theta^3 + \mathcal{O}(\theta^5). \end{aligned} \tag{2.77}$$

Then the density fluctuation is

$$\delta = \frac{3}{20}\theta^2 + \mathcal{O}(\theta^4) \simeq \frac{3}{20}\left(\frac{6t}{B}\right)^{2/3}. \tag{2.78}$$

Since $\delta \propto t^{2/3}$, this can be considered as the fluctuation in the linear theory. At the turn-around and collapse time,

$$\delta_t^{\rm linear} = \frac{3(6\pi)^{3/2}}{20} \simeq 1.06, \tag{2.79}$$

$$\delta_c^{\rm linear} = \frac{3(12\pi)^{3/2}}{20} \simeq 1.69. \tag{2.80}$$

These values correspond to δ_t and δ_c in the non-linear theory discussed above. Although we here consider only the Einstein-de Sitter universe, the value of $\delta_c^{\rm linear}$ is insensitive to models of the universe (see Appendix A).

2.6 Cooling Diagram

In this section, we consider the role of temperature of a fluid in the structure formation.

The potential energy U of a homogeneous sphere with density ρ and radius R is

$$U = -\int_0^R dr\, \frac{G}{r} M \left(\frac{r}{R}\right)^3 4\pi r^2 \rho = -\frac{3}{5}\frac{GM^2}{R} \tag{2.81}$$

From the virial theorem, the kinetic energy K is given by

$$K = -\frac{1}{2}U = \frac{3}{10}\frac{GM^2}{R}. \tag{2.82}$$

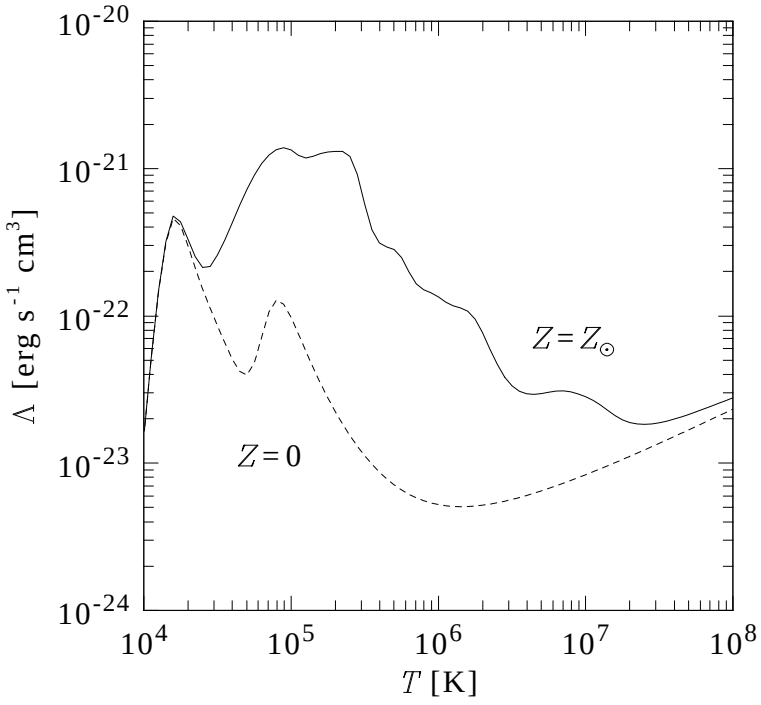

Figure 2.2: The cooling function $\Lambda(T)$ when the metalllicity Z is equal to the solar metallicity (solid) and zero (dashed). These curves are calculated using SPEX.

The kinetic energy is also written as

$$K = \int 4\pi r^2 dr \ \frac{\rho v^2}{2} = \frac{1}{2} M \sigma^2, \tag{2.83}$$

where

$$\sigma^2 = \frac{1}{\rho} \int 4\pi r^2 dr \ \frac{\rho v^2}{2} \tag{2.84}$$

is the velocity dispersion. Note that the mean velocity vanishes in the center-of-mass system. Equating the above two expressions of K, the virial mass M_v is defined as

$$M_v = \frac{5}{3} \frac{R\sigma^2}{G}. \tag{2.85}$$

For an ideal gas,

$$\frac{1}{2} \mu m_p \sigma^2 = \frac{3}{2} k_B T, \tag{2.86}$$

where μ is the mean molecular weight. For a gas with hydrogen and helium mass fractions of 3/4 and 1/4, $\mu = 16/27 \simeq 0.59$. Combining Equations (2.85) and (2.86), the virial temperature T_v is defined as

$$T_v = \frac{GM\mu m_p}{5Rk_B}. \tag{2.87}$$

Note that T_v loses the original meaning of temperature unless the system is in equilibrium.

In the spherical collapse model, a structure of any scale forms and its contraction is supposed to stop when it is virialized. In reality, however, the energy loss due to radiative processes allows further contraction. The energy loss rate per unit volume is described by the cooling function $\Lambda(T)$:

$$-\frac{dE}{dt} = n^2\Lambda(T) \tag{2.88}$$

Note that $\Lambda(T)$ strongly depends on the atomic composition of the gas. Figure 2.2 shows the behavior of $\Lambda(T)$ for the cases of solar metallicity and zero metallicity. The curves are calculated using a spectral fitting package SPEX[1].

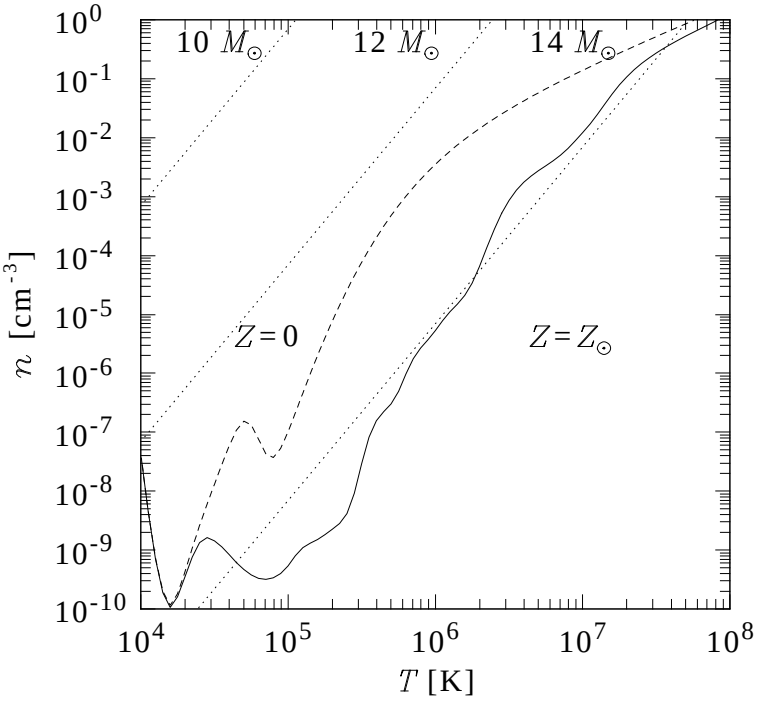

Figure 2.3: A cooling diagram. The free-fall time is equal to the cooling time on the solid and dashed curves when the metallicity is solar abundance and zero, respectively. It is assumed that the baryon fraction f_b is 0.1.

The time scale on which the thermal energy of gas $3nk_BT/2$ is lost due to the radiative processes is

$$\tau_{\rm cool} = \frac{3}{2}\frac{k_BT}{n\Lambda(T)}, \tag{2.89}$$

which is called the cooling time.

Let us compare $\tau_{\rm cool}$ with the free-fall time $\tau_{\rm ff}$ defined as

$$\tau_{\rm ff} = t_c - t_t = \frac{\pi}{2}\sqrt{\frac{r_t^3}{2GM}} = \sqrt{\frac{3\pi}{32G\rho_t}} = \sqrt{\frac{3\pi}{32G\mu m_p n}}, \tag{2.90}$$

[1]http://www.sron.nl/spex

where $\rho_t = 3M/4\pi r_t^3$. This is the time scale of a gravitational collapse of a homogeneous sphere.

Figure 2.3 demonstrates the curves on which $\tau_{\rm cool}$ is equal to $\tau_{\rm ff}$. In this figure, the baryon fraction is assumed to be 0.1, i.e., the free-fall time is $1/\sqrt{10}$ of that of the gas alone. Such a diagram is called the cooling diagram. In the region above the curve, $\tau_{\rm cool} < \tau_{\rm ff}$, i.e., the cooling process is fast enough for the gas to contract and form small-scale structures. On the other hand, in the region below the curve, where $\tau_{\rm cool} > \tau_{\rm ff}$, the gas quasi-statically contracts after the virial equilibrium. Figure 2.3 also shows lines on which the virial mass is constant and indicates that a gas with mass $\lesssim 10^{12} M_\odot$ can form small structures. This corresponds to the typical mass scale of galaxies. For an object with mass of $\sim 10^{14} M_\odot$, the radiative cooling is not efficient and the object quasi-statically contracts over a Hubble time, which corresponds to a cluster of galaxies.

2.7 Press-Schechter Theory

For most astrophysical and cosmological applications, statistical properties of clusters are needed. It is crucial, but difficult to estimate how much objects with a given mass exist in the universe since density fluctuations grow in the highly non-linear regime. Press & Schechter (1974) have proposed a treatment with combination of linear and non-linear models.

Given the probability distribution of the density fluctuations, we can theoretically estimate how much structures of mass M exist in the universe. Assume that the probability distribution function has a Gaussian form:

$$P(\delta)d\delta = \frac{1}{\sqrt{2\pi\sigma^2}} \exp\left(-\frac{\delta^2}{2\sigma^2}\right) d\delta. \tag{2.91}$$

The mass fluctuation δ_M is obtained by integrating the $\delta^{\rm linear}(\boldsymbol{q}, t)$ on Lagrangian coordinates $\boldsymbol{q}$:

$$\delta_M(\boldsymbol{q}, t) = \frac{3}{4\pi R^3} \int_{|\boldsymbol{q}-\boldsymbol{q}'|\le R} d^3q' \ \delta^{\rm linear}(\boldsymbol{q}', t). \tag{2.92}$$

Then the probability distribution of δ_M also has a Gaussian form:

$$P(\delta_M) = \frac{1}{\sqrt{2\pi\sigma_M^2}} \exp\left(-\frac{\delta_M^2}{2\sigma_M^2}\right) \tag{2.93}$$

The fraction of the Lagrangian region which is eventually incorporated into structures of mass $> M$ is

$$P(M) = \int_{\delta_c}^{\infty} d\delta_M \ P(\delta_M). \tag{2.94}$$

The lower bound of the integral is often chosen to be δ_c in the spherical model. Finally, the number density of structures of mass M is estimated as

$$\frac{dn}{d\ln M} = 2\bar{\rho}|P(M) - P(M + dM)| = 2\bar{\rho} \left|\frac{dP}{d\sigma_M}\right| \left|\frac{d\sigma_M}{dM}\right|. \tag{2.95}$$

The factor 2 comes from an *ad hoc* treatment in the Press-Schechter theory. Equation (2.95) is called the mass function. For a Gaussian distribution function,

$$\frac{dn}{d\ln M} = \sqrt{\frac{2}{\pi}} \frac{\bar{\rho}}{M} \left|\frac{d\ln\sigma_M}{d\ln M}\right| \frac{\delta_c}{\sigma_M} \exp\left(-\frac{\delta_c^2}{2\sigma_M^2}\right). \tag{2.96}$$

More recently, the mass function is predicted by N-body simulations. Equation (2.96) shows, however, the mass function depends on cosmological parameters through the linear growth rate of density fluctuations, the dispersion of mass fluctuations, etc. This is why clusters of galaxies play an important role in determining cosmological parameters.

Chapter 3

AN X-RAY VIEW OF CLUSTERS OF GALAXIES

3.1 Basic Properties of Clusters of Galaxies

Just as its name indicates, a cluster of galaxies consists of hundreds or thousands of galaxies in a diameter on the order of a few Mpc. However, galaxies account for only several percent of the total mass of the cluster, typically $\sim 10^{14} M_\odot$. A cluster is filled with a hot diffuse gas called a intracluster gas. The intraclsuter gas still occupies no more than a few ten percent of the total mass. The remaining mass is thought to reside in unknown dark matter.

The dynamical time scale $\tau_{\rm dyn}$ of a cluster is given as

$$\tau_{\rm dyn} = \frac{1}{\sqrt{G\rho}} \sim \mathcal{O}(1) \quad \text{Gyr}. \tag{3.1}$$

Compared to the age of the universe, $\sim$ 14 Gyr, $\tau_{\rm dyn}$ is short enough for a cluster to settle in dynamical equilibrium, but long enough to remember the initial conditions of the universe. This is a major reason why clusters can be strong cosmological probes.

The virial temperature T_v (defined in Section 2.6) is given by

$$k_B T_v = \frac{GM\mu m_p}{5R} \sim \mathcal{O}(1) \quad \text{keV}. \tag{3.2}$$

This temperature corresponds to the energy range of X-rays. In fact, the intracluster gas is the strongest diffuse X-ray emitter in the universe.

3.2 Radiative Processes

3.2.1 Bremsstrahlung

In the X-ray region, the most important radiative process in clusters is bremsstrahlung. If the gas has a thermal, i.e., Maxwellian velocity distribution characterized by temperature T, the total power $\epsilon^{\rm ff}$ per unit volume due to thermal bremsstrahlung is given by

$$\epsilon^{\rm ff} = \left(\frac{2\pi k_B T}{3m_e}\right)^{1/2} \frac{16}{3} \frac{e^6}{m_e \hbar c^3} Z^2 n_e n_i \bar{g}^{\rm ff}(T), \tag{3.3}$$

where n_e and n_i are electron density and ion density, respectively, Z is the atomic number of the ion, m_e is the electron mass and $\bar{g}^{\rm ff}(T)$ is a quantum correction called the Gaunt factor. We

emphasize that $\epsilon^{\rm ff}$ is proportional to the square of density. Compared to optical observations of galaxies where emissivity is proportional to density $n_{\rm gal}$ of galaxies, the signal-to-noise ratio in X-ray observations is higher by a factor $n_{\rm gal}/\langle n_{\rm gal}\rangle \sim 10^3$, where $\langle n_{\rm gal}\rangle$ is the mean galaxy density in the universe. This is why clusters are more clearly identified in X-ray observations.

3.2.2 Line Emission

Intracluster medium has a variety of spectra in the X-ray region, depending on atomic composition, temperature, ionization fraction, etc. The ionization energy E_I of a hydrogen-like ion is given by

$$E_I = -\frac{Z^2}{n^2}\frac{m_e e^4}{2\hbar^2} \simeq -13.6 \times \frac{Z^2}{n^2} \quad \text{eV}, \tag{3.4}$$

where n is the principal quantum number. For atoms from oxygen ($Z = 8$) to iron ($Z = 26$) which have relatively higher cosmic abundance, E_I is in the X-ray region. Generally, the emissivity of a line emission is proportional to densities of ions and electrons.

3.3 Observables

The most important observables of clusters in X-ray are surface brightness and spectroscopic temperature. The X-ray surface brightness I_X is defined as an integration of cooling function in the X-ray energy region along the ling-of-sight.

$$I_X = \int dl\ n_e n_p \Lambda_X(T). \tag{3.5}$$

The spectroscopic temperature $T_{\rm spec}$ is estimated by spectral fitting. Since the emissivities of the continuum (mainly bremsstrahlung) and line spectra are both proportional to the square of density, the ratio of line emission to continuum emission is independent of density and gives information on temperature alone. Then density can be derived from the surface brightness.

3.4 Hydrostatic Equilibrium

Given the density n and temperature T of a gas, its pressure p is obtained by

$$p = nk_B T. \tag{3.6}$$

In order to estimate the total mass $M(r)$ of the cluster within a sphere of radius r, the assumption of hydrostatic equilibrium (HSE) is usually made:

$$\frac{1}{\rho}\frac{dp}{dr} = -\frac{GM(r)}{r^2}, \tag{3.7}$$

where we have also assumed spherical symmetry of the system. Then the total mass can be written as

$$M_{\rm HSE}(r) = -\frac{rk_B T}{G\mu m_p}\left[\frac{d\ln\rho}{d\ln r} + \frac{d\ln T}{d\ln r}\right]. \tag{3.8}$$

Note that the mass is independent of the magnitude of the density.

Traditional analytic models of galaxy clusters assume isothermality since temperature gradient is difficult to measure. In this case, the second term of the parenthesis of Equation (3.8) is

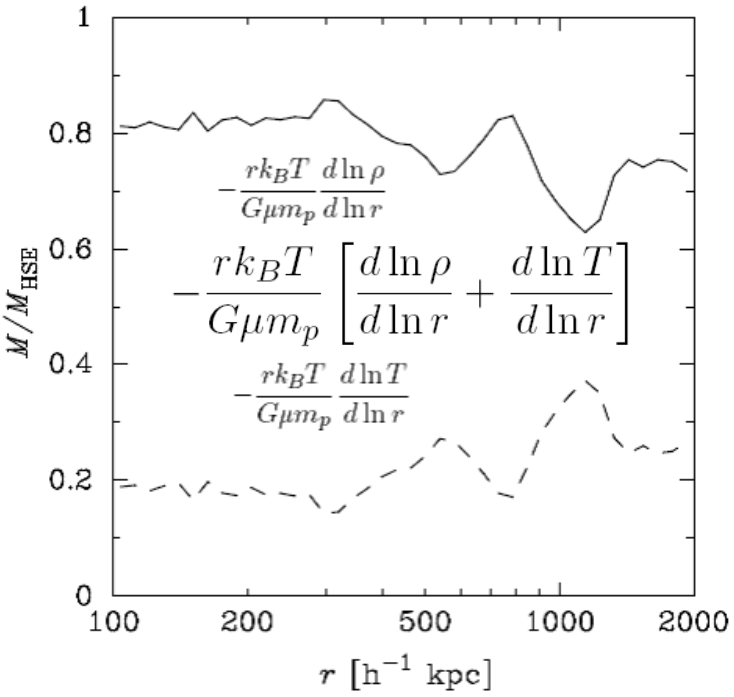

Figure 3.1: The ratio of the first (solid) and second (dashed) terms of (3.8) to the total HSE mass for the cluster g1542a (see Chapter 4). At each radius, the sum of the values of the two lines is unity. The range of r is divided into 40 logarithmically equal bins.

dropped off. Figure (3.1) illustrates fractions of the first and second terms of Equation (3.8) for the cluster g1542a from a SPH simulation described in Chapter 4. The cluster g1542a is apparently relaxed and has no big substructure. The mass due to temperature gradient contributes ~ 20 % to the total. This contribution would be too large for precise mass measurement. We do not assume isothermality in the following chapters.

Although the HSE assumption is widely used in conventional X-ray data analysis of clusters, its validity is not fully understood. A rough measure of the validity of HSE is provided by the sound crossing time scale $\tau_{\rm sc}$ defined as

$$\tau_{\rm sc} = \frac{R}{c_s} \sim \mathcal{O}(10^8) \quad \text{yr} \tag{3.9}$$

where R (~ 1 Mpc) is a characteristic length of a cluster and c_s is the sound speed in the ICM (For an ideal gas, $c_s^2 = \gamma k_B T/\mu m_p$ where μ is the mean molecular weight). If $\tau_{\rm sc} < \tau_{\rm dyn}$, pressure reacts fast enough to resettle the system in balance the gravitational collapse, and thus the HSE assumption is valid in the zeroth approximation. For a cluster, the sound crossing time scale is shorter, but not too shorter than the dynamical time scale (Equation (3.1)). Therefore the validity of HSE leaves much room for discussion. This is the main topic of this thesis.

Chapter 4

COSMOLOGICAL SIMULATIONS

In order to investigate the validity of the HSE assumption, we analyze clusters extracted from cosmological simulations. We use one cluster from an adaptive mesh refinement (AMR) hydrodynamical simulation performed by Renyue Cen and 11 clusters from a smoothed particle hydrodynamical (SPH) simulation performed by Klaus Dolag. Before presenting results of our analysis, we briefly summarize the main features of these two kinds of simulations in this chapter. We also show properties of the clusters to be analyzed.

4.1 AMR Hydrodynamical Simulation

The AMR simulation in this study was carried out with an Eulerian adaptive mesh refinement code, Enzo (Bryan, 1999; Bryan & Norman, 1999; O'Shea et al., 2004; Joung et al., 2009). We refer readers to Cen (2012) for more detail. The simulation was run first with a low resolution mode in a periodic box of 120 h^{-1} Mpc on a side. Then a region centered on a cluster with a mass of $\sim 2 \times 10^{14} h^{-1} M_{\odot}$ was resimulated with a higher resolution in an adaptively refined manner. The size of the refined region is $21 \times 24 \times 20 (h^{-1}\mathrm{Mpc})^3$. The mean interparticle separation and mass of dark matter particles in the refined region are 117 h^{-1} kpc (comoving) and $1.07 \times 10^8 h^{-1} M_{\odot}$, respectively.

Star particles are created according to the prescription of Cen & Ostriker (1992). Their typical mass is $\sim 10^6 M_{\odot}$. The simulation includes a metagalactic UV background (Haardt & Madau, 1996), shielding of UV radiation by neutral hydrogen (Cen et al., 2005) and metallicity-dependent radiative cooling (Cen et al., 1995). While supernova feedback is modeled following Cen et al. (2005), AGN feedback is not included in this simulation, which may cause unrealistically high abundance of baryons in the innermost region of the cluster. The cosmological parameters used in this simulation are $(\Omega_b, \Omega_m, \Omega_\Lambda, h, n_s, \sigma_8) = (0.046,\ 0.28,\ 0.72,\ 0.70,\ 0.96,\ 0.82)$, following the WMAP7-normalized ΛCDM model (Komatsu et al., 2011).

Then a cluster is identified and the cubic box of a side of $3.8h^{-1}$ Mpc surrounding the entire cluster is extracted from the simulation data. The dark matter and stars are represented by particles, and the temperature and density of gas are given on the 520^3 grids (the grid length is $7.324h^{-1}$kpc).

The radius r_{500} of the cluster is $\sim 640h^{-1}$ kpc (r_{500} is defined so that the mean density inside r_{500} is 500 times the critical density of the universe). The center-of-mass velocity of the cluster within r_{500} is set to vanish. The total mass M_{500} within r_{500} is $\sim 2 \times 10^{14} M_{\odot}$. The spherical average gas temperature at r_{500} is $\sim$ 2 keV, and the circular speed there is $v_{500} = \sqrt{GM_{500}/r_{500}} \sim 1000$ km s^{-1}.

Projected densities of gas, dark matter and stars on x-z plane are plotted in the left panels of Figure 4.1. The right panels of Figure 4.1 show the three-dimensional view of the three components. The left (right) plots are color-coded according to the surface (space) densities normalized by the fraction of each component averaged over the box, $\tilde{\Omega}_k$ ($k =$ gas, dark matter and stars). Note that the fraction $\tilde{\Omega}_k$ is different from the density parameter Ω_k because the box is selected preferentially around the cluster.

As is clear from Figure 4.1, the gas distribution is smoother but very well traces the underlying dark matter distribution. In contract, stars are more significantly concentrated in high density regions, and exhibit numerous small clumps, most of which are not identified/resolved in the gas distribution.

Figure 4.2 plots the radial density and mass profiles of the cluster. The stellar fraction in the inner region ($r < 200h^{-1}$kpc) is significantly higher than the typical observed value. This is a well-known common problem among current high-resolution cosmological simulations, and implies that some important baryon physics including high-energy phenomena and star formation is still missing in the simulation. We perform the analysis of cluster gas, *assuming* that this excessive star densities in the inner region does not affect our conclusions at outer radius.

Figure 4.3 represents velocity fields in x-y, y-z and z-x planes passing through the center of the cluster. The red/blue arrows have negative/positive radial velocity, showing that the gas in the outer regions ($r \gtrsim 1h^{-1}$ Mpc) falls toward the center while its direction is randomized in the inner region.

4.2 SPH Simulations

The SPH simulations used in this study were performed by K. Dolag using the TreePM/SPH code GADGET-2 (Springel et al., 2001, 2005). We refer readers to Dolag et al. (2006, 2009) for more detail. First, 10 regions containing massive halos were extracted from a lower resolution DM-only simulation performed by Yoshida et al. (2001). Then these regions were resimulated with higher resolution including baryon physics. The simulations include radiative cooling, heating due to a uniform redshift-dependent UV background according to Haardt & Madau (1996). Star formation and feedback processes are also included based on Springel & Hernquist (2003). The cosmological parameters in the simulations are based on a flat ΛCDM model with $\Omega_{m,0} = 0.3$, $H_0 = 70$ km s^{-1} Mpc^{-1}, $f_{\rm bar} = 0.13$ (the baryon fraction) and $\sigma_8 = 0.9$.

In this study, we use 5 regions named g1, g72, g1542, g3344 and g914. The regions g1 and g72 contain 6 and 2 clusters, respectively. The other regions have only one cluster for each, hence there are 11 clusters in total. The clusters in the same region is named a, b, c, ... in a decreasing order of mass. For the analysis in the subsequent chapters, we arrange mesh data for each cluster. A physical variable A defined at a point $\boldsymbol{x}$ is given by

$$A(\boldsymbol{x}) = \sum_i m_i \frac{A_i}{\rho_i} W(\boldsymbol{x} - \boldsymbol{x}_i, h), \tag{4.1}$$

where m_i, ρ_i and A_i are the mass, density, the physical variable of consideration defined for the SPH particle i and $W(\boldsymbol{x}, h)$ is the kernel function characterized by the smoothing length h. The kernel function W is often defined to be a Gaussian function:

$$W(\boldsymbol{x}, h) = \left(\frac{1}{h\sqrt{\pi}}\right)^3 \exp\left(-\frac{x^2}{h^2}\right) \tag{4.2}$$

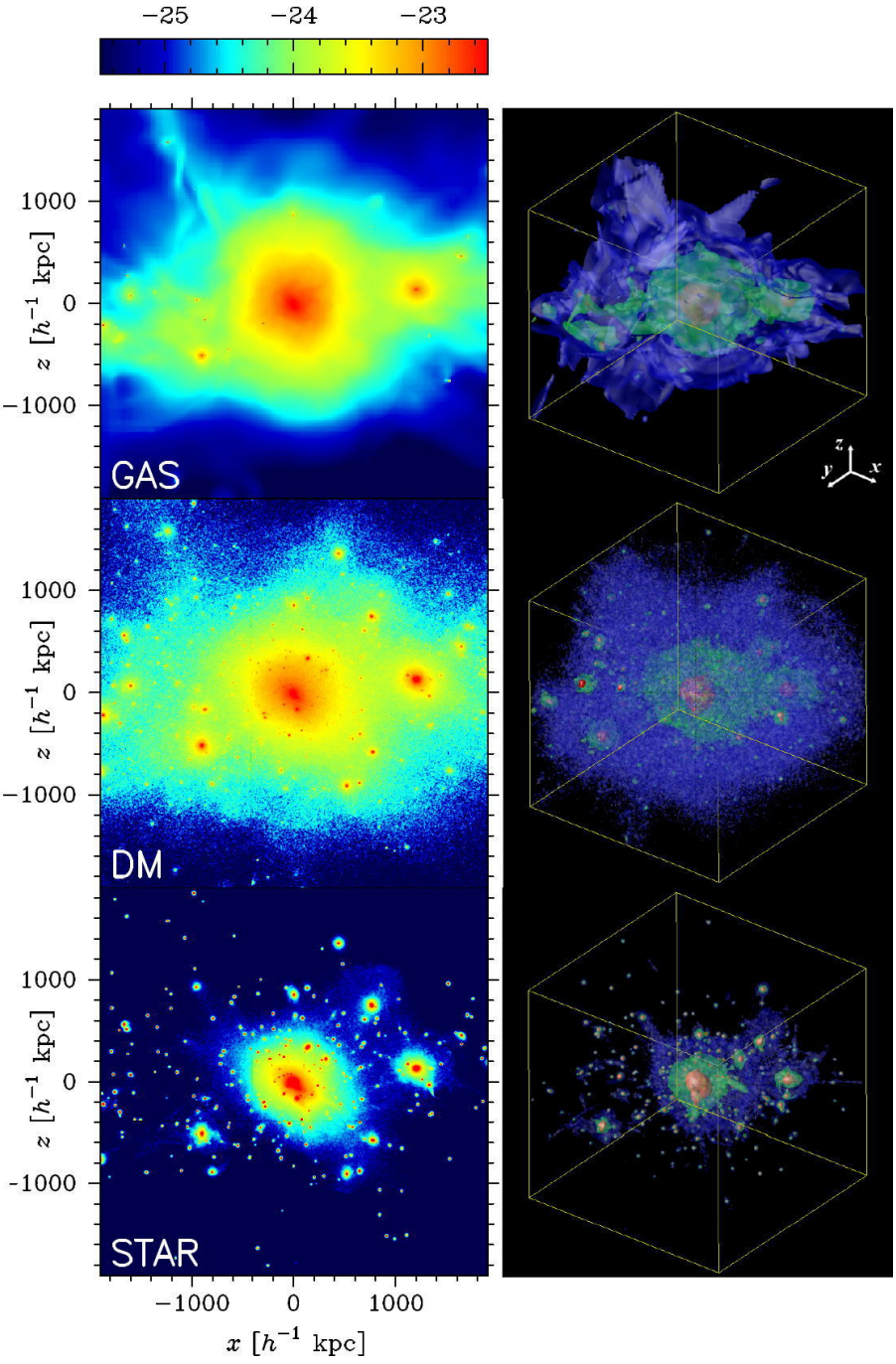

Figure 4.1: Densities of gas (top), dark matter (middle) and stars (bottom) are shown in two ways for each. *Left*: Projected surface densities on x-z plane normalized by the fraction of each component in the box: $\log_{10}[\int dl\ \rho_k \tilde{\Omega}_k^{-1}\ /(\mathrm{g\ cm^{-3}}\ h^{-1}\ \mathrm{kpc})]$, where k is one of gas, dark matter and stars and $\tilde{\Omega}_k$ is the fraction of k component in the box. *Right*: Equal-density surfaces for $\log_{10}[\rho_k \tilde{\Omega}_k^{-1}/(\mathrm{g\ cm^{-3}}\ h^{-1}\ \mathrm{kpc})]$=−28.0 (blue), −27.0 (green) and −26.0 (red). Densities are normalized in the same way as the left panel.

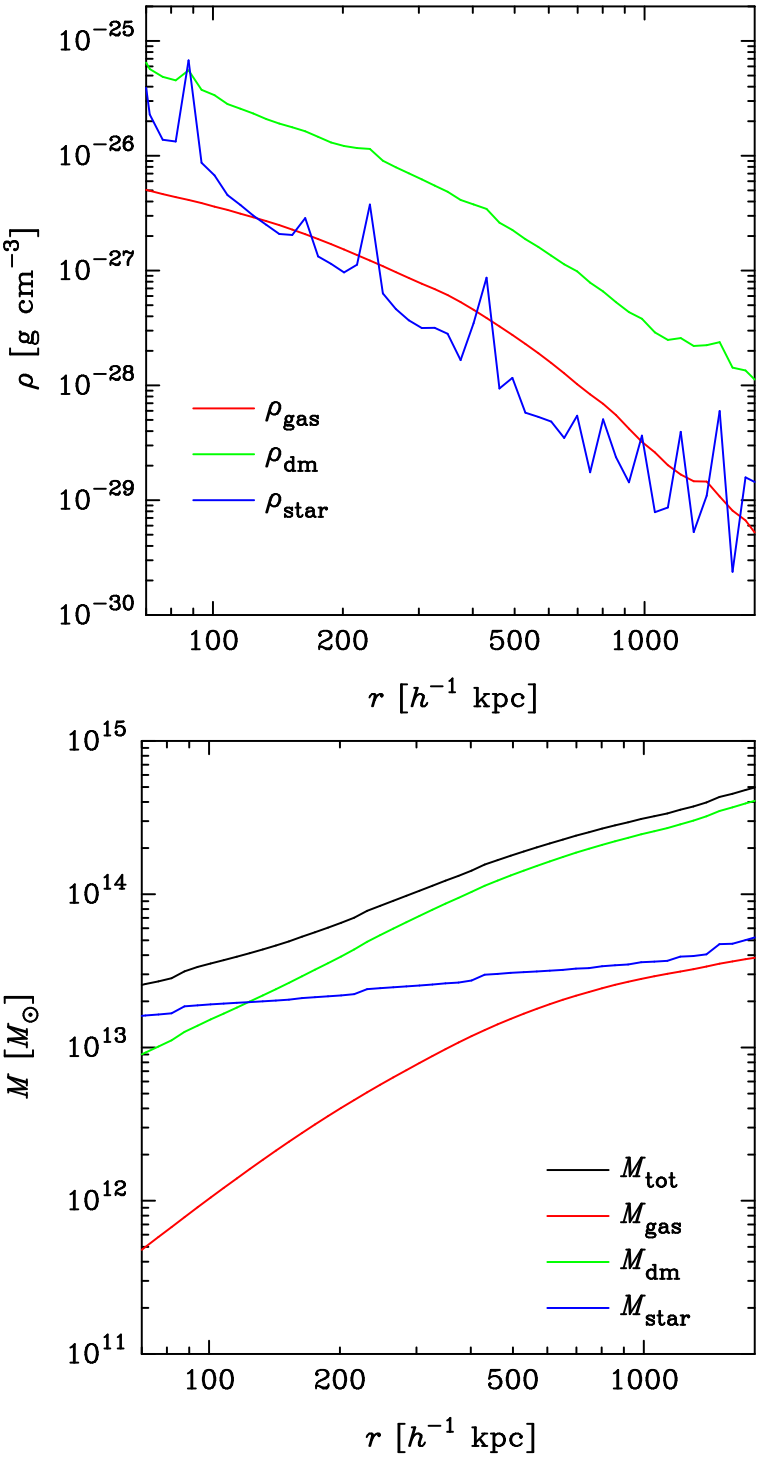

Figure 4.2: Radial profiles of densities (left) and masses (right) are shown for gas (red), dark matter (green) and stars (blue). The black line in the right panel shows the total gravitational mass; $M_{\rm tot} = M_{\rm gas} + M_{\rm dm} + M_{\rm star}$. The analysis is performed on the 50 logarithmically equal radial bins.

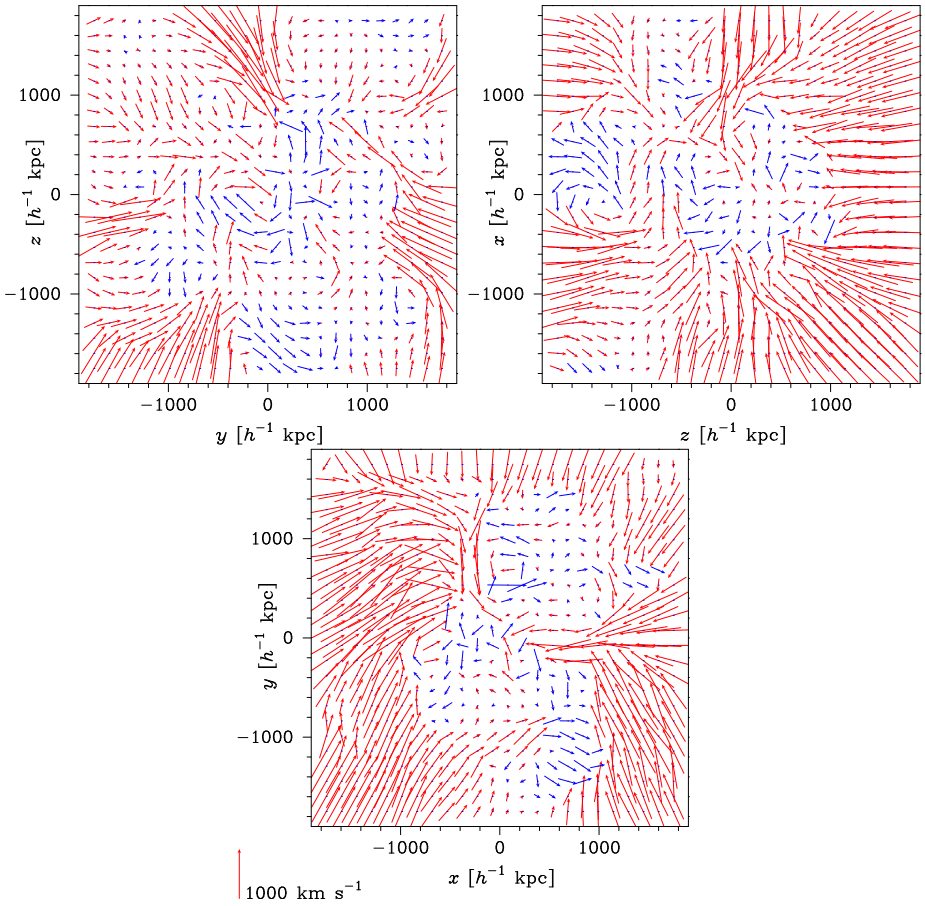

Figure 4.3: Velocity fields in x-y (left), y-z (middle) and z-x (right) planes passing through the center of the cluster. The arrow is red if $v_r < 0$, and blue if $v_r > 0$. The length of the arrow is proportional to the magnitude of the velocity. An arrow with a speed of 1000 km s^{-1} is shown for reference.

or a spline function:

$$W(\boldsymbol{x}, h) = \frac{3}{2\pi h^3} \cdot \begin{cases} \dfrac{2}{3} - \dfrac{x^2}{h^2} + \dfrac{1}{2}\dfrac{x^3}{h^3} & \left(0 \le \dfrac{x}{h} < 1\right), \\ \dfrac{1}{6}\left[2 - \dfrac{x^3}{h^3}\right] & \left(1 \le \dfrac{x}{h} < 2\right), \\ 0 & \left(2 \le \dfrac{x}{h}\right). \end{cases} \tag{4.3}$$

We use the latter form in this study. Figures 4.4 to 4.7 show the gas density and temperature on the x-y plane. Although the clusters g1b to g1f and g72b are substructures of the clusters g1a and g72a, respectively, their densities look not so much different from those of isolated clusters. On the other hand, the temperatures of substructures, especially of g1d, g1e and g1f show fairly irregular behaviors. This is because the hot gas of the central cluster is extended to the outer region.

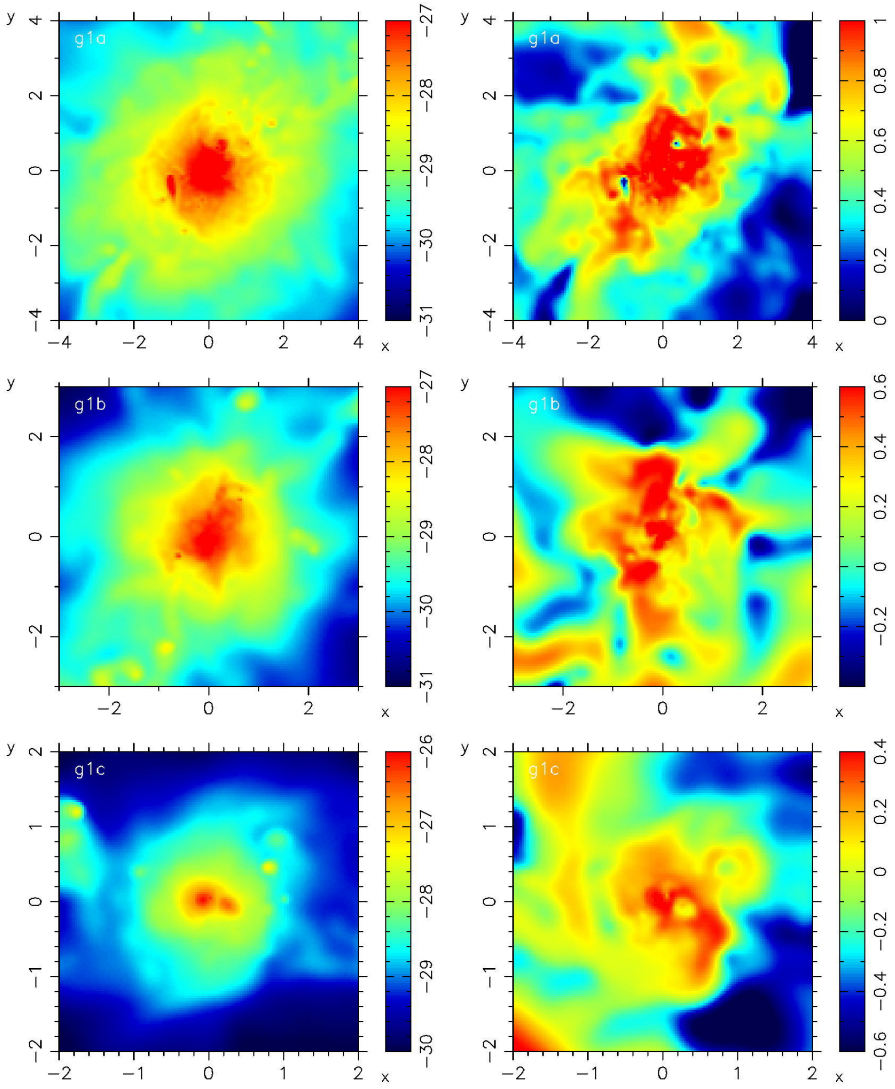

Figure 4.4: Density (*left*) and temperature (*right*) maps on the x-y plane of the clusters g1a (*top*), g1b (*middle*) and g1c (*bottom*)

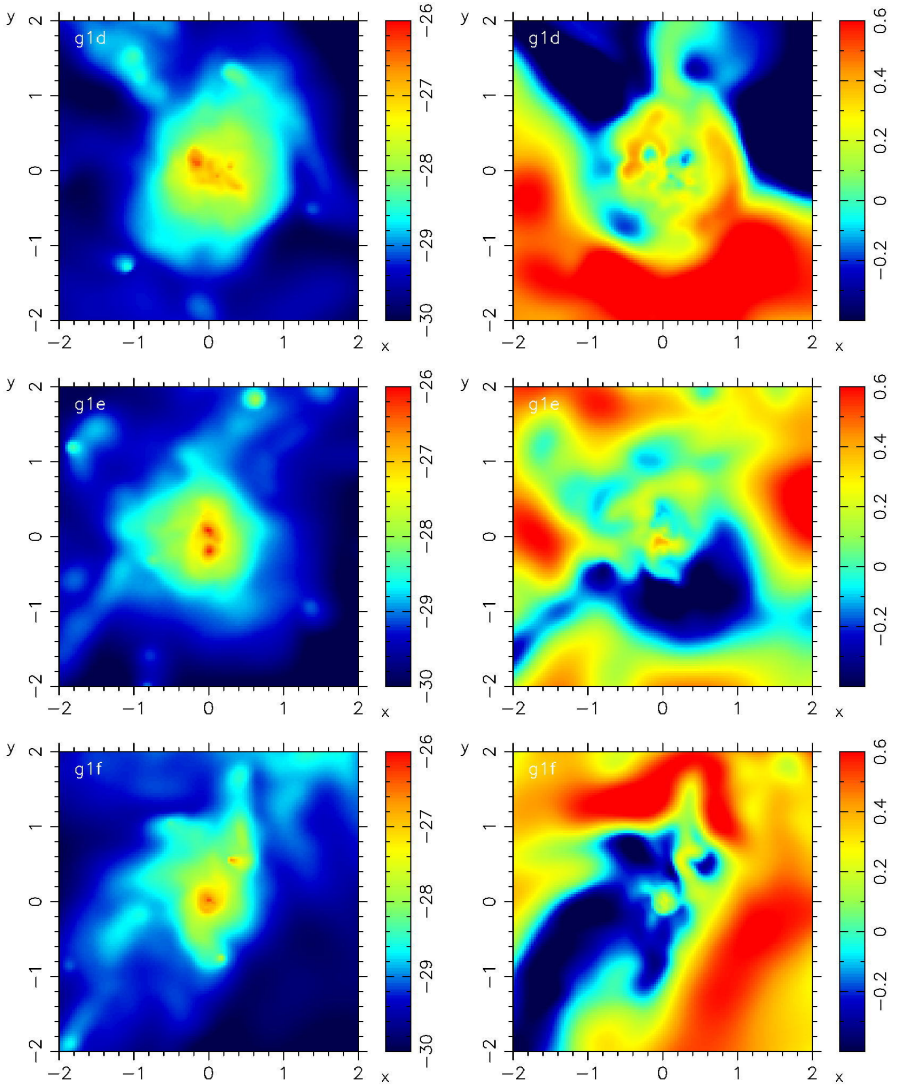

Figure 4.5: Density (*left*) and temperature (*right*) maps on the x-y plane of the clusters g1d (*top*), g1e (*middle*) and g1f (*bottom*)

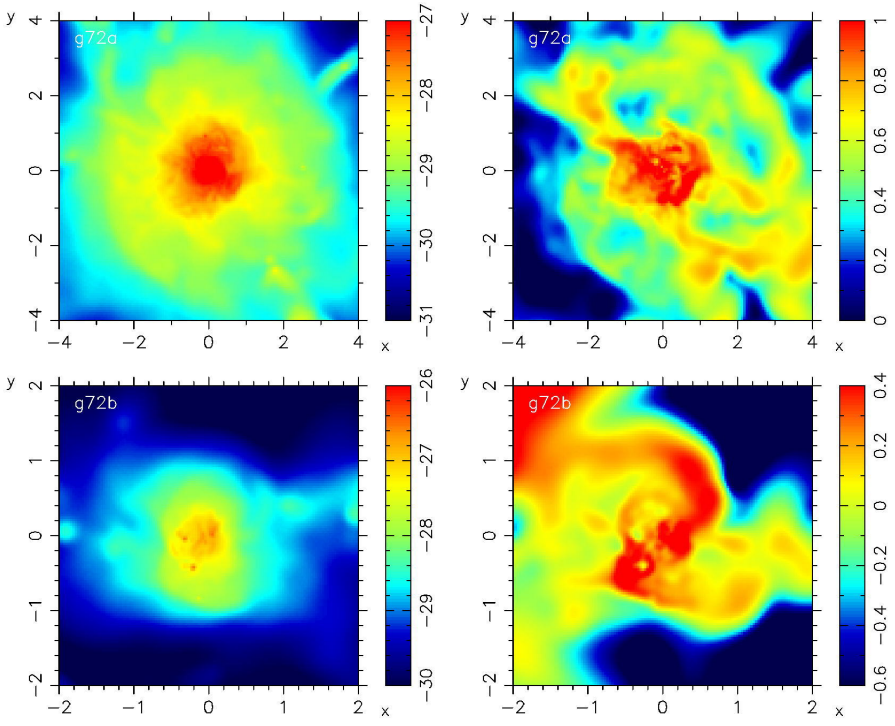

Figure 4.6: Density (*left*) and temperature (*right*) maps on the x-y plane of the clusters g72a (*top*) and g72b (*bottom*)

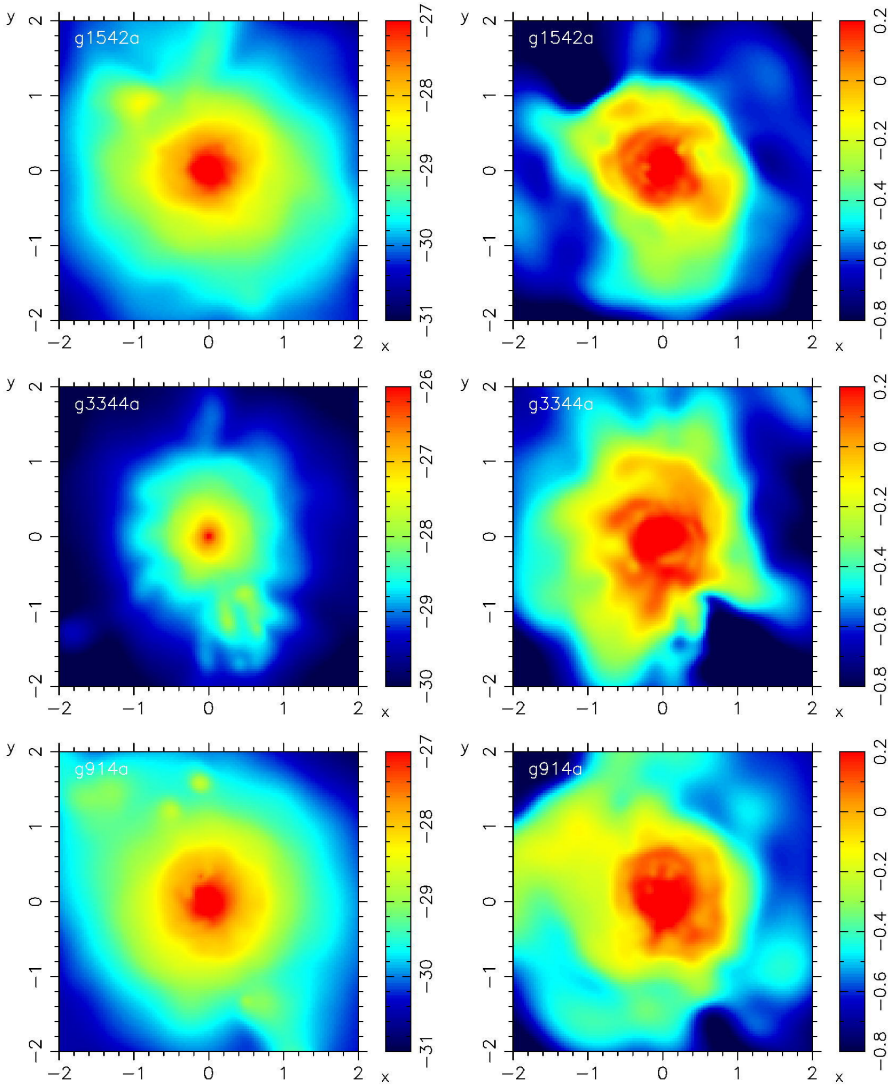

Figure 4.7: Density (*left*) and temperature (*right*) maps on the x-y plane of the clusters g1542a (*top*), g3344a (*middle*) and g914a (*bottom*)

Chapter 5

VALIDITY OF HYDROSTATIC EQUILIBRIUM

5.1 Method to Examine the Validity of HSE

Our analysis method to discuss the validity of HSE using gases in simulated clusters is based on the Euler equations:

$$\frac{\partial \boldsymbol{v}}{\partial t} + (\boldsymbol{v}\cdot\nabla)\boldsymbol{v} = -\frac{1}{\rho_{\rm gas}}\nabla p - \nabla\phi, \tag{5.1}$$

where ϕ is the gravitational potential, and $\rho_{\rm gas}$, $\boldsymbol{v}$ and p are the density, velocity and pressure of gas. While the Jeans equations do not describe the gas dynamics in their original form, Rasia et al. (2004) and Lau et al. (2009) added the gas pressure gradient term to the Jeans equations, and adopted the resulting equations in analyzing simulated clusters. We argue in the next subsection that this is not justified, and present the result based on the Jeans equations but using collisionless dark matter particles in Appendix C, for reference. We define the total mass $M_{\rm tot}$ of a cluster inside a volume V as

$$M_{\rm tot} = \int_V d^3x\ \rho_{\rm tot}, \tag{5.2}$$

where $\rho_{\rm tot}$ is the total density of the cluster. For the simulated cluster considered throughout this paper, $\rho_{\rm tot}$ consists of densities of gas, dark matter and stars, i.e., $\rho_{\rm tot} = \rho_{\rm gas} + \rho_{\rm dm} + \rho_{\rm star}$. The total mass can be rewritten in terms of p and $\boldsymbol{v}$ using Poisson's equation and Gauss's theorem:

$$M_{\rm tot} = \frac{1}{4\pi G}\int_{\partial V} d\boldsymbol{S}\cdot\nabla\phi = \frac{1}{4\pi G}\int_{\partial V} d\boldsymbol{S}\cdot\left[-\frac{1}{\rho_{\rm gas}}\nabla p - (\boldsymbol{v}\cdot\nabla)\boldsymbol{v} - \frac{\partial \boldsymbol{v}}{\partial t}\right], \tag{5.3}$$

where ∂V is the surface surrounding the volume V and we have used equation (5.1) in the second equality. Now the total mass is evaluated by the gas quantities alone, without any knowledge on dark matter and stars. This is why the present method is applicable, in principle, to the X-ray data of galaxy clusters.

If we adopt a spherical surface as ∂V, the total mass can be decomposed into the following four *effective* mass terms:

$$M_{\rm tot} = M_{\rm therm} + M_{\rm rot} + M_{\rm stream} + M_{\rm accel}, \tag{5.4}$$

where

$$M_{\rm therm} = -\frac{1}{4\pi G}\int_{\partial V} dS\ \frac{1}{\rho_{\rm gas}}\frac{\partial p}{\partial r}, \tag{5.5}$$

$$M_{\rm rot} = \frac{1}{4\pi G}\int_{\partial V} dS\ \frac{v_\theta^2 + v_\varphi^2}{r}, \tag{5.6}$$

$$M_{\rm stream} = -\frac{1}{4\pi G}\int_{\partial V} dS\ \left[v_r\frac{\partial v_r}{\partial r} + \frac{v_\theta}{r}\frac{\partial v_r}{\partial \theta} + \frac{v_\varphi}{r\sin\theta}\frac{\partial v_r}{\partial \varphi}\right], \tag{5.7}$$

and

$$M_{\rm accel} = -\frac{1}{4\pi G}\int_{\partial V} dS\ \frac{\partial v_r}{\partial t}. \tag{5.8}$$

We emphasize here that the above set of equations does not assume spherical symmetry of the system; we just take a spherical surface as the integral surface and write down equation (5.3) in spherical coordinates.

The first term, $M_{\rm therm}$, originates from the thermal pressure gradient of gas. If the gas motion is negligible, $M_{\rm therm}$ should be equal to the total mass $M_{\rm tot}$, and thus regarded as a cluster mass estimated under the HSE assumption. In other words, the difference between $M_{\rm tot}$ and $M_{\rm therm}$ is a quantitative measure of the departure from the HSE assumption.

The inertial term $(\boldsymbol{v}\cdot\nabla)\boldsymbol{v}$ in the Euler equations reduces to $M_{\rm rot}$ and $M_{\rm stream}$. If there exists a coherent rotational motion around the center of the cluster, $M_{\rm rot}$ can be interpreted as the centrifugal force term. Without such a motion, however, the local tangential velocity of different directions at different locations on the sphere could make $M_{\rm rot}$ significantly large. During the course of the cluster evolution, gas generally falls toward the center of the cluster with larger streaming speed with increasing radius from the center. In this case, $M_{\rm stream}$ becomes *negative* and cannot be neglected. On the other hand, it becomes positive and/or negligible, especially in the innermost region where the gas velocity is more randomized than that in the outer regions.

Finally the acceleration term, $M_{\rm accel}$, corresponds to the $-\partial v_r/\partial t$ term in the Euler equations, and becomes positive/negative when gas is decelerating/accelerating.

All the mass terms are invariant with respect to the choice of the axis of the spherical coordinates, but are not necessarily positive. Note also that $M_{\rm rot}$ and $M_{\rm stream}$, corresponding to the inertial term, are not invariant with respect to the Galilei transformation. Thus we evaluate those in the center-of-mass frame of the entire simulated cluster.

5.2 Comparison with Analysis Methods Adopted by Previous Work

The set of basic equations that we adopt in this paper is essentially identical to that of Fang et al. (2009), except the fact that they interpreted the difference between $M_{\rm tot}$ and $M_{\rm therm} + M_{\rm rot} + M_{\rm stream}$ as "turbulent gas motion" while we call it the acceleration term $M_{\rm accel}$ as directly implied from equation (5.1), and evaluate it from the residual, $M_{\rm accel} = M_{\rm tot} - M_{\rm therm} - M_{\rm rot} - M_{\rm stream}$.

We are not sure why they ascribed the term to the turbulent motion. It is true that part of the gas acceleration would be due to the turbulent gas motion, but not entirely. Furthermore the numerical simulation does not include any physical processes directly related to the turbulent motion. Even if the turbulent motion might be important for real clusters, it should come from some physics below the subgrid scales that cannot be properly resolved in the numerical simulation. Effects of gas random motion above the resolved scales should be included in $M_{\rm rot}$ and $M_{\rm stream}$. We note, however, that the different interpretation of $M_{\rm accel}$ does not affect at all

the conclusion of Fang et al. (2009) that gas rotation is the most important term to describe the origin of departure from HSE in their simulated clusters. As we will show below, this is not consistent with our result.

In previous literature, the Jeans equations are sometimes used in analyzing the gas motion in simulated clusters. For that purpose, a thermal pressure gradient term is added by hand to the basic equations (e.g., Rasia et al., 2004; Lau et al., 2009). Assuming the steady state, i.e., $\partial \boldsymbol{v}/\partial t = 0$, the Jeans equations in r-direction (B.20) is now replaced by the following equation:

$$\begin{aligned}
&\left[v_r \frac{\partial}{\partial r} + \frac{v_\theta}{r}\frac{\partial}{\partial \theta} + \frac{v_\varphi}{r\sin\theta}\frac{\partial}{\partial \varphi}\right] v_r + \frac{1}{\rho_{\rm gas}}\left[\frac{1}{r}\frac{\partial(\rho_{\rm gas}\sigma^2_{r\theta})}{\partial\theta} + \frac{1}{r\sin\theta}\frac{\partial(\rho_{\rm gas}\sigma^2_{r\varphi})}{\partial\varphi}\right] \\
&+ \frac{\sigma^2_{r\theta}\cot\theta}{r} - \frac{v_\theta^2 + v_\varphi^2}{r} \\
&= -\frac{1}{\rho_{\rm gas}}\frac{\partial(\rho_{\rm gas}\sigma^2_{rr})}{\partial r} - \frac{2\sigma^2_{rr} - \sigma^2_{\theta\theta} - \sigma^2_{\varphi\varphi}}{r} - \frac{1}{\rho_{\rm gas}}\frac{\partial p}{\partial r} - \frac{\partial \phi}{\partial r},
\end{aligned} \tag{5.9}$$

where σ^2_{ij} denotes the ij-component of the velocity dispersion tensor. Lau et al. (2009) converted each term of equation (5.9) to mass term; see equations (6) to (11) of Lau et al. (2009). Then they interpreted that the first two terms in the right hand side of the above equation originate from "random gas motion". It is, however, difficult to justify such a treatment *in analysing simulated clusters* for the following reason.

Equation (5.9) implicitly assumes that the ICM consists of two distict components; the ordinary thermalized component described by the Euler equations, and the unthermalized component described by the Jeans Equations (D. Nagai, private communication). As shown in Appendix B, diagonal components of the velocity dispersion tensor in the Jeans equations correspond to thermal pressure in the Euler equations. Hence a pressure gradient term is included in the Jeans equations, resulting in Equation (5.9).

It is certainly true that actual clusters would contain the unthermalized gas component such as the cold gas accreting along with galaxies into clusters, and therefore the Jeans equations may provide better descriptions for that component. It has not been proved that the multi-component gas obeys Equation (5.9). Equation (5.9) assumes that the two kinds of gases have the same density, but it is not always the case. Nor is there reason that the multi-component gas obeys a single dynamical equation.

Even if a *real gas* obeys Equation (5.9) or some dynamical equation, all the *gases in current numerical simulations* obey the Euler equations. The equality $M_{\rm tot} = M_{\rm therm} + M_{\rm rot} + M_{\rm stream} + M_{\rm accel}$ holds and there is no room for other terms to contribute, apart from numerical artifacts. Therefore the analysis of the simulated clusters should use the Euler equations. It is of course important to consider the proper treatment of the unthermalized gas in numerical simulations, but is beyond the scope of the present paper.

5.3 Results

First we evaluate the *effective* mass terms defined in Section 5.1 for the cluster from the AMR simulation (hereafter the AMR cluster), which is plotted in Figure 5.1; the left panel shows the mass profiles, while the right panel indicates their fractional contribution to the total mass within the radius.

The total mass $M_{\rm tot}(r)$ is computed by directly summing up all the dark matter and star particles and gas of grids within the sphere of r. The other terms, $M_{\rm therm}$, $M_{\rm rot}$ and $M_{\rm stream}$,

require the pressure and velocity fields evaluated at r. For that purpose, we use the density, velocity and temperature of gas defined at 520^3 original grid points, and first bin the cluster into 50 logarithmically equal radial intervals between 90–1900 h^{-1} kpc, 10×10 linearly equal angular intervals.

Integrands of equations (5.5), (5.6) and (5.7) are calculated in each bin. Derivatives of the physical variables such as $\partial p/\partial r$ are calculated as follows; first $\partial/\partial x$, $\partial/\partial y$ and $\partial/\partial z$ are computed from the difference of the adjacent the original Cartesian grid points. Then $\partial/\partial r$, $\partial/\partial\theta$ and $\partial/\partial\varphi$ in our spherical coordinates are calculated applying the chain rule.

In this way, $M_{\rm therm}(r)$, $M_{\rm rot}(r)$ and $M_{\rm stream}(r)$ are computed by integrating the corresponding integrands evaluated above. Finally we estimate $M_{\rm accel}$ simply from the residual of $M_{\rm accel} = M_{\rm tot} - M_{\rm therm} - M_{\rm rot} - M_{\rm stream}$, since we have the cluster data at $z = 0$ alone. This estimate for $M_{\rm accel}$ may be different from the original defintion, i.e., equation (5.8). Indeed when we attempted to compute $M_{\rm accel}$ directly from the box mentioned in Section 4.1, it turned out to be too small to obtain a correct gravitational potential for the entire cluster. Thus we go back to a larger simulation box of a side of 22.5 h^{-1} Mpc and the grid length of 29.34 h^{-1} kpc that encloses our cluster. Then we compute the gravitational potential using FFT to obtain the gas acceleration at each grid point. This enables us to directly calculate $M_{\rm accel}$. Figure 5.2 is a comparison of $M_{\rm accel}$ ' s calculated by two methods. The directly calculated $M_{\rm accel}$ (magenta line) is in good agreement with $M_{\rm tot} - M_{\rm therm} - M_{\rm rot} - M_{\rm stream}$ (black line), although there is a large difference between the two within 200 h^{-1} kpc. Also, we make sure that the sum $M_{\rm therm} + M_{\rm rot} + M_{\rm stream} + M_{\rm accel}$ reproduces $M_{\rm tot}$ within ~ 2 % except for the innermost region ($r < 200h^{-1}$ kpc), where it deviates from $M_{\rm tot}$ by up to ~ 9 %. Thus the estimation of $M_{\rm accel}$ by $M_{\rm tot} - M_{\rm therm} - M_{\rm rot} - M_{\rm stream}$ is sufficiently good given the quoted errors of our conclusion below. Although it seems better to use $M_{\rm accel}$ directly calculated from equation (5.8), the grid size of the larger box is so coarse that we cannot take advantage of the high resolution of the simulations in this study. Therefore, we decided to use the smaller box explained in Section 4.1 and $M_{\rm accel}$ is calculated by $M_{\rm tot} - M_{\rm therm} - M_{\rm rot} - M_{\rm stream}$ in the following analysis.

The left panel of Figure 5.1 implies that $M_{\rm therm}$ agrees with $M_{\rm tot}$ reasonably well. Each of the other three terms contributes less than 10 % of the total mass (the dotted curves correspond to the case in which each term becomes negative and its absolute value is plotted instead).

In order to consider the validity of HSE more quantitatively, we plot the fractional contribution of each mass term in the right panel of Figure 5.1. The rotation term, $M_{\rm rot}$, is always positive (by definition) and contributes approximately 10 % almost independently of radius. In contrast, the streaming velocity term, $M_{\rm stream}$, is mostly negative, and varies a lot at different radial bins. As a result, the difference of the total mass $M_{\rm tot}$ and the HSE mass $M_{\rm therm}$ is mostly explained by the acceleration term $M_{\rm accel}$ alone; compare the black and magenta curves in the right panel of Figure 5.1. At $r = r_{500}$ and r_{200}, the deviation from HSE in terms of the mass difference $(M_{\rm therm} - M_{\rm tot})/M_{\rm tot}$ is about 10 %. Nevertheless the value significantly varies at different radii and it is safe to conclude that $(M_{\rm therm} - M_{\rm tot})/M_{\rm tot}$ ranges approximately 10-20 % at $r < r_{200}$. Also there is no systematic trend of the validity of the HSE assumption as a function of radius. Even though the reliability of the simulation is suspicious for $r < 200h^{-1}$kpc due to the excessive stellar concentration (Section 4.1), $(M_{\rm therm} - M_{\rm tot})/M_{\rm tot}$ fluctuates between -10 % and $+25$ % for $300h^{-1}$kpc $< r < r_{500}$. Thus there is no guarantee that HSE becomes a better approximation toward the inner central region.

The sum $M_{\rm rot} + M_{\rm stream} + M_{\rm accel} (= M_{\rm tot} - M_{\rm therm})$ corresponds to the term intergrating the Lagrangian derivative of the gas velocity over the sphere. Therefore the fact that it is small compared with $M_{\rm therm}$ and $M_{\rm tot}$ is simply translated into the condition of HSE that the gas acceleration from a Lagrangian point of view is negligible compared with the pressure gradient

and the total gravity.

Next we divide the AMR cluster into two regions; upper and lower hemispheres with respect to the x-y plane. Then we duplicate each hemisphere into one cluster. We call the synthetic cluster constructed from the $z > 0$ ($z < 0$) hemisphere "z+" ("z-"). Although these clusters are of course not independent of the original cluster and we cannot make a statistical argument on their properties, we can briefly look at the effects of substructures or inhomogeneity of temperature and velocity field.

We repeat the same analysis on these two synthetic clusters, and the results are plotted in Figure 5.4. The amplitudes of the different terms vary significantly between the two clusters, and the degree of the validity of HSE is also very different. Nevertheless the generic trend is clear; the relation of $M_{\rm accel} \approx M_{\rm tot} - M_{\rm therm}$ holds almost independently of r.

It is not clear, however, why the two hemispheres have so different values of $(M_{\rm tot} - M_{\rm therm})/M_{\rm tot}$; HSE holds very well for "z+", while it is not the case for "z-". The visual inspection of Figure 4.1 does not reveal any significant difference between the two. It may be because some local concentrations of dark matter enhance the acceleration/deceleration of gas, and influence the overall non-sphericity of the gas density. Thus the analysis taking account of the ellipticity may provide a deeper insight on the validity of HSE, but is beyond the scope of this thesis.

So far we have shown the results for a single cluster. In order to statistically discuss the validity of HSE, we analyze other simulated clusters. Since the AMR simulation contains only a single cluster, we use ones taken from the SPH simulations explained in Section 4.2. For these clusters, we calculate $M_{\rm accel}$ directly from the gas acceleration data. We also assume spherical symmetry and do not divide the spherical surface at a given radius just for simplicity. Figures 5.5 to 5.10 show the results.

These figures show $M_{\rm therm}$ deviates from $M_{\rm tot}$ by up to 30 %. The large deviation occurs both inside outside r_{500}. The figures also show $|M_{\rm accel}|$ is larger than $M_{\rm rot}$ and $|M_{\rm stream}|$ especially where $M_{\rm therm}$ deviates from $M_{\rm tot}$. There are, however, cases where $M_{\rm accel}$ almost vanishes while $M_{\rm rot}$ explains the difference between $M_{\rm tot}$ and $M_{\rm therm}$ (e.g. inside r_{500} of g3344a). The above results are basically the same for the AMR cluster.

For all the clusters, the sum $M_{\rm therm} + M_{\rm rot} + M_{\rm stream} + M_{\rm accel}$ approximately reproduces $M_{\rm tot}$ within ~ 5 % for most regions. This indicates that the estimate of $M_{\rm accel}$ by $M_{\rm tot} - M_{\rm therm} - M_{\rm rot} - M_{\rm stream}$ is justified, as confirmed for the AMR cluster.

The analysis so far is precise in that it shows the values of the mass terms at each radius, but it does not clarify the overall behavior of the mass terms. Hence we perform the same analysis with much coarser radial bins and compare $M_{\rm tot}$ and $M_{\rm therm}$. We use only the AMR cluster and the central cluster (labeled "a") of each SPH simulation box in order to see the difference between substructure-rich/poor clusters. Figure (5.11) shows the result. With the exception of the cluster g72a (magenta), $M_{\rm therm}$ is smaller than $M_{\rm tot}$ by 10 – 15 % inside r_{500} and the difference becomes larger by up to 20 – 30 % at larger radii. Therefore the HSE mass *systematically underestimates* the total mass by 10 – 15 % inside r_{500} and by 20 – 30 % outside r_{500}. Again, the main reason for the deviation is the gas acceleration toward the center.

Figure (5.11) also indicates that there is no difference between substructure-rich and substructure-poor clusters, or AMR and SPH clusters. Although the number of the analyzed clusters is yet small, the underestimation of $M_{\rm tot}$ by $M_{\rm therm}$ is probably common to simulated clusters.

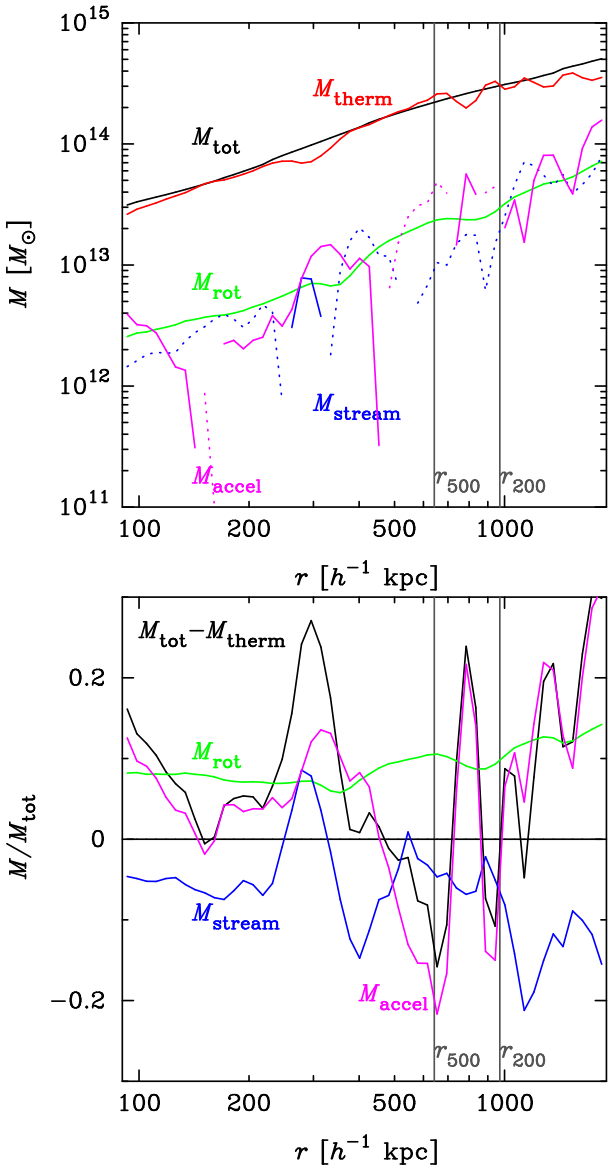

Figure 5.1: The *effective* mass terms in Equation (5.4) for the gas in the simulated cluster are shown in the top panel: $M_{\rm tot}$ (black), $M_{\rm therm}$ (red), $M_{\rm rot}$ (green), $M_{\rm stream}$ (blue) and $M_{\rm accel}$ (magenta). Dotted line means that its sign is inverted. Ratios of mass terms to $M_{\rm tot}$ are shown in the bottom panel. The black line shows $(M_{\rm tot} - M_{\rm therm})/M_{\rm tot}$ and colored lines represent the same things as the left panel. The analysis is performed on the 50 logarithmically equal radial bins and 10 linearly equal bins both in polar and azimuthal angles.

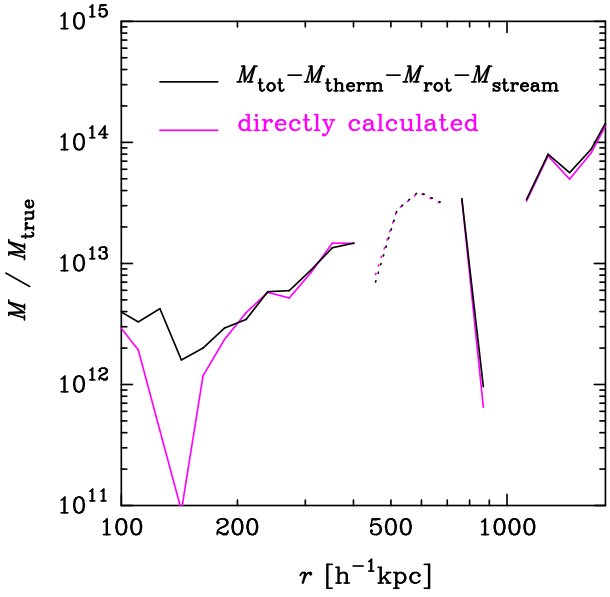
10^{15}
10^{14}
10^{13}
10^{12}
10^{11}
M / M_{true}
100
200
500
1000
r [h^{-1}kpc]
$M_{tot}-M_{therm}-M_{rot}-M_{stream}$
directly calculated

Figure 5.2: s.

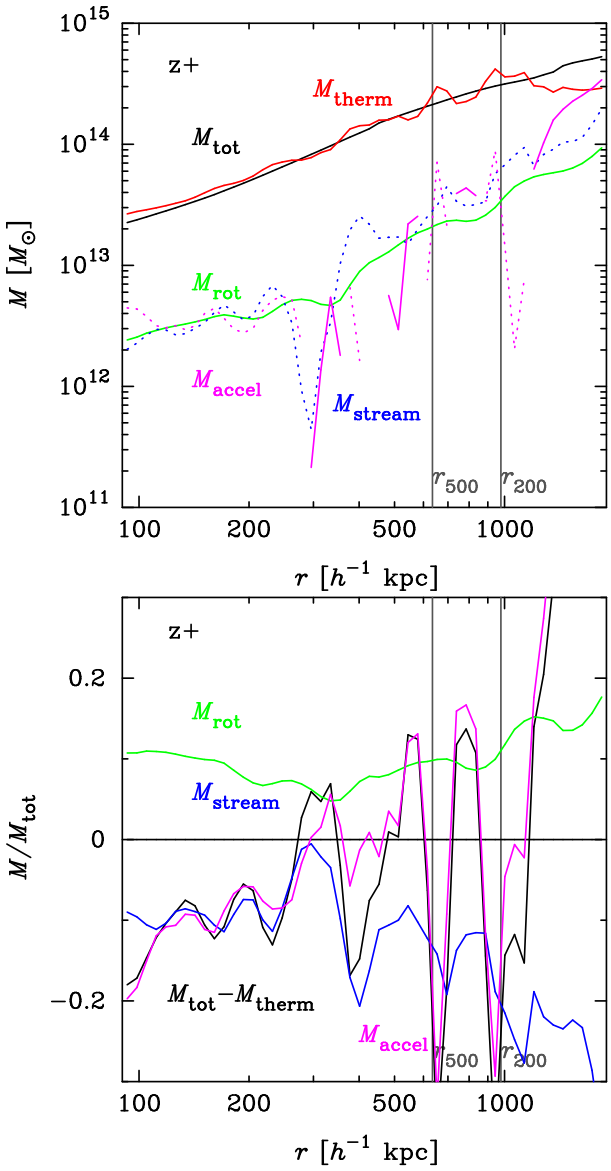

Figure 5.3: Same as Figure 5.1, but for the clusters "z+".

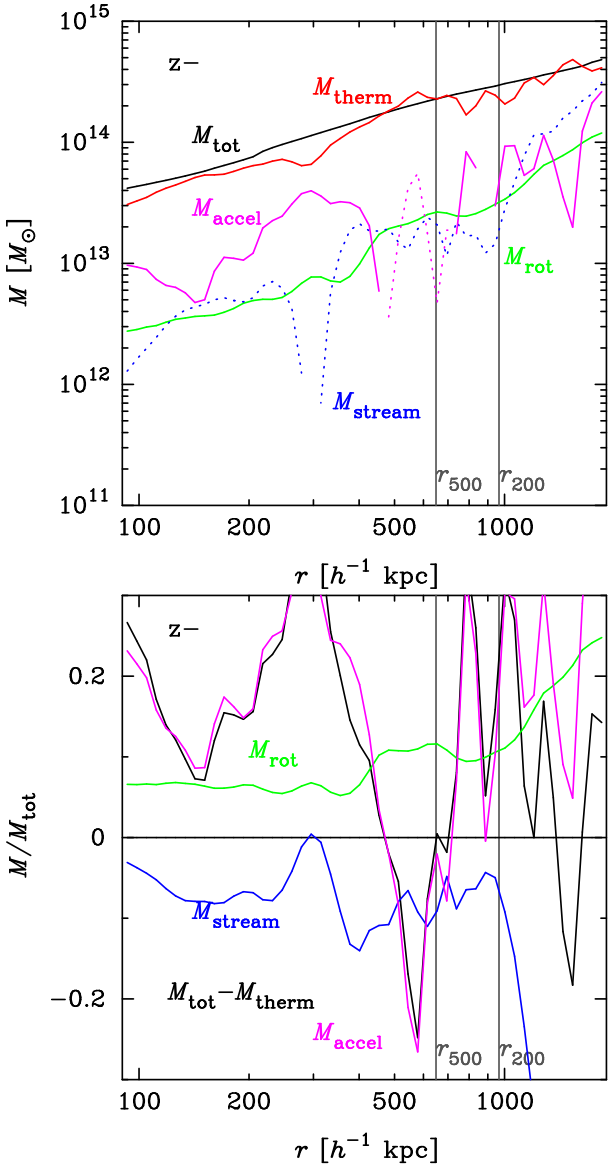

Figure 5.4: Same as Figure 5.1, but for the clusters "z-".

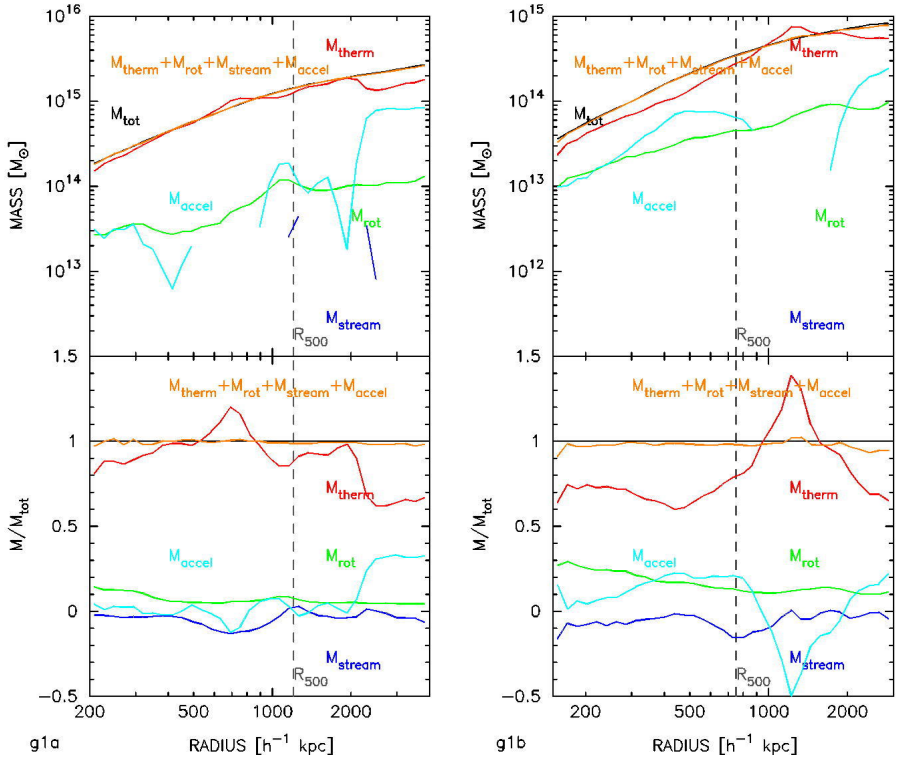

Figure 5.5: The *effective* mass terms in Equation (5.4) for the gas in the simulated cluster g1a (*left*) and g1b (*right*) are shown in the top panel: $M_{\rm tot}$ (black), $M_{\rm therm}$ (red), $M_{\rm rot}$ (green), $M_{\rm stream}$ (blue) and $M_{\rm accel}$ (cyan). The sum $M_{\rm therm} + M_{\rm rot} + M_{\rm stream} + M_{\rm accel}$ is also shown in orange. Dotted line means that its sign is inverted. Ratios of mass terms to $M_{\rm tot}$ are shown in the bottom panel. The colored lines represent the same things as the left panel. The analysis is performed on the 25 logarithmically equal radial bins.

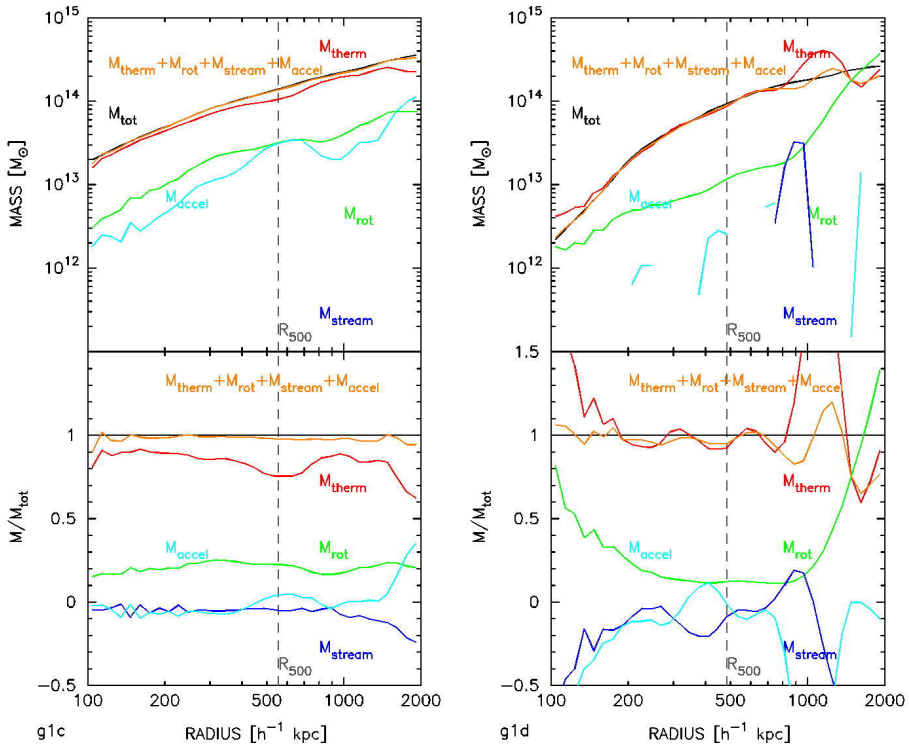

Figure 5.6: Same as Figure 5.5, but for the clusters g1c (*left*) and g1d (*right*).

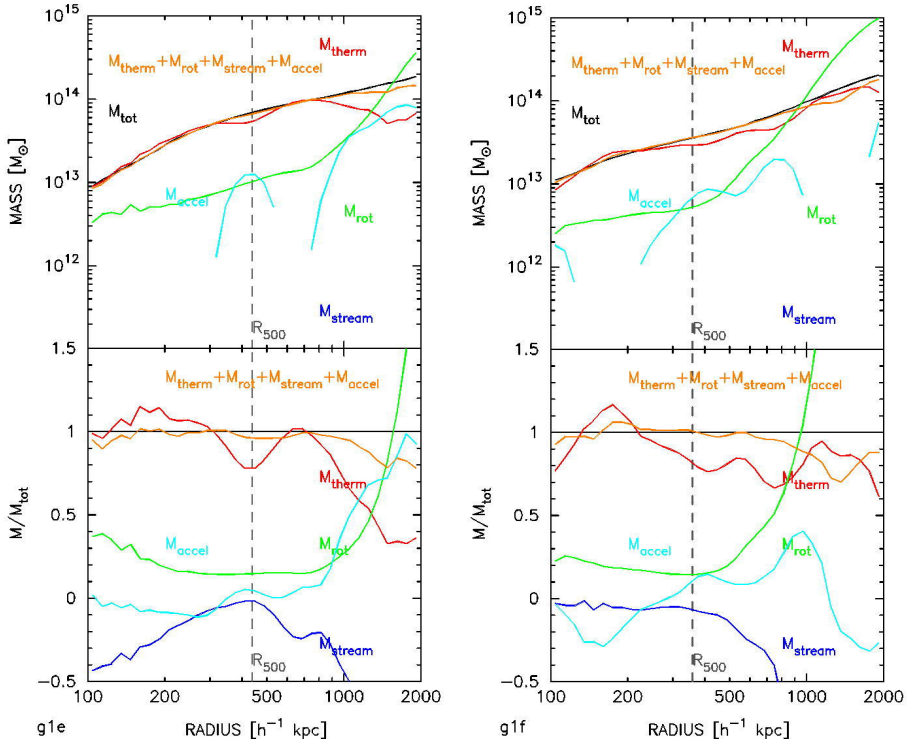

Figure 5.7: Same as Figure 5.5, but for the clusters g1e (*left*) and g1f (*right*).

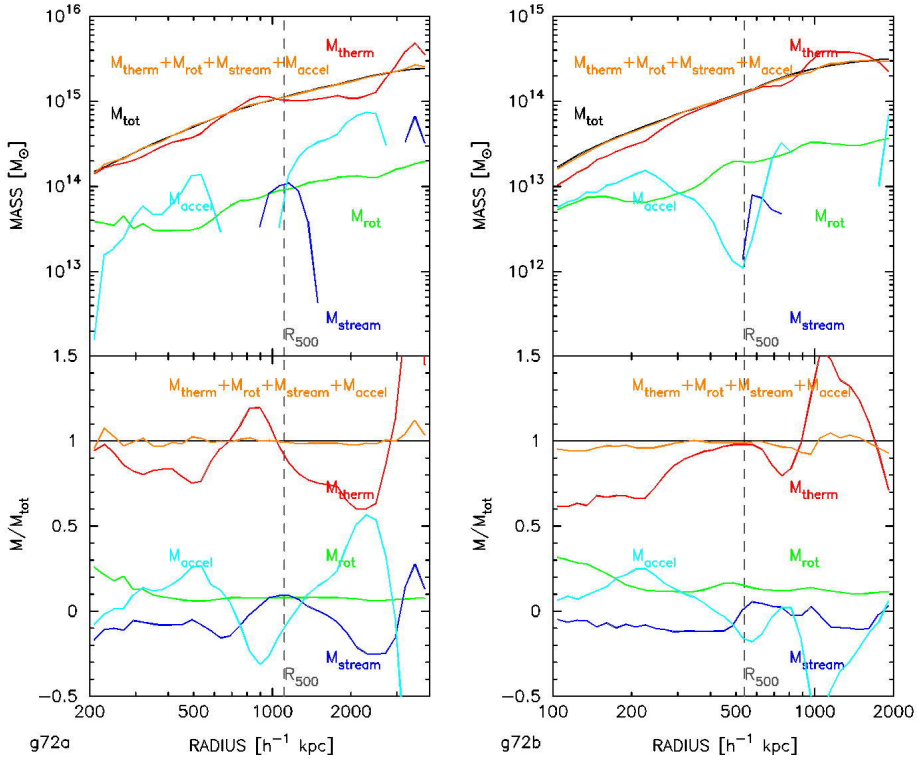

Figure 5.8: Same as Figure 5.5, but for the clusters g72a (*left*) and g72b (*right*).

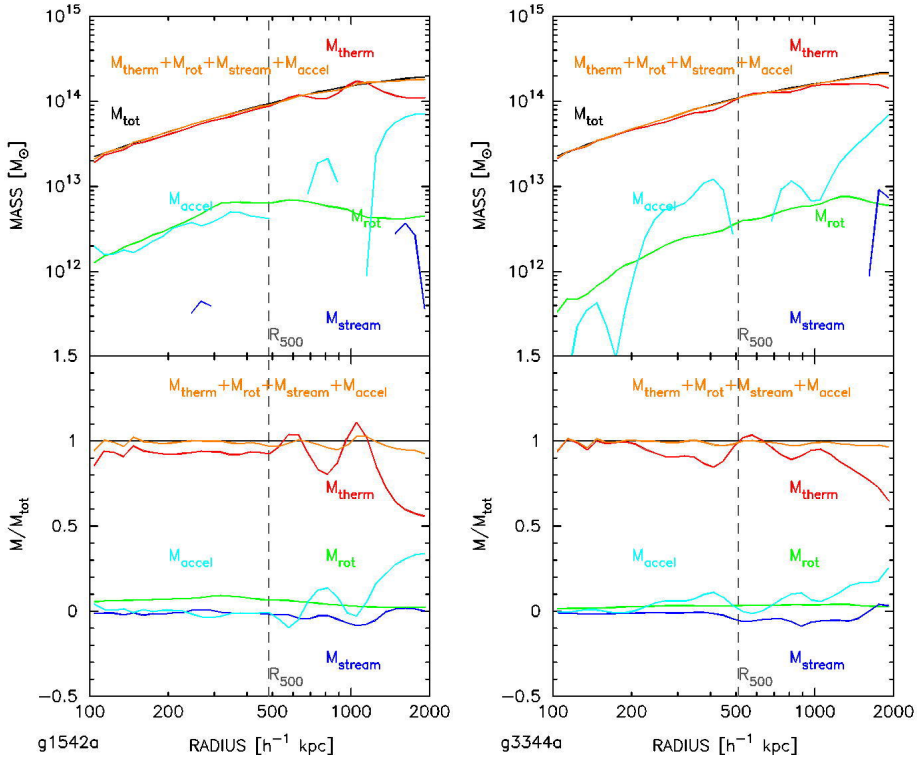

Figure 5.9: Same as Figure 5.5, but for the clusters g1542a (*left*) and g3344a (*right*).

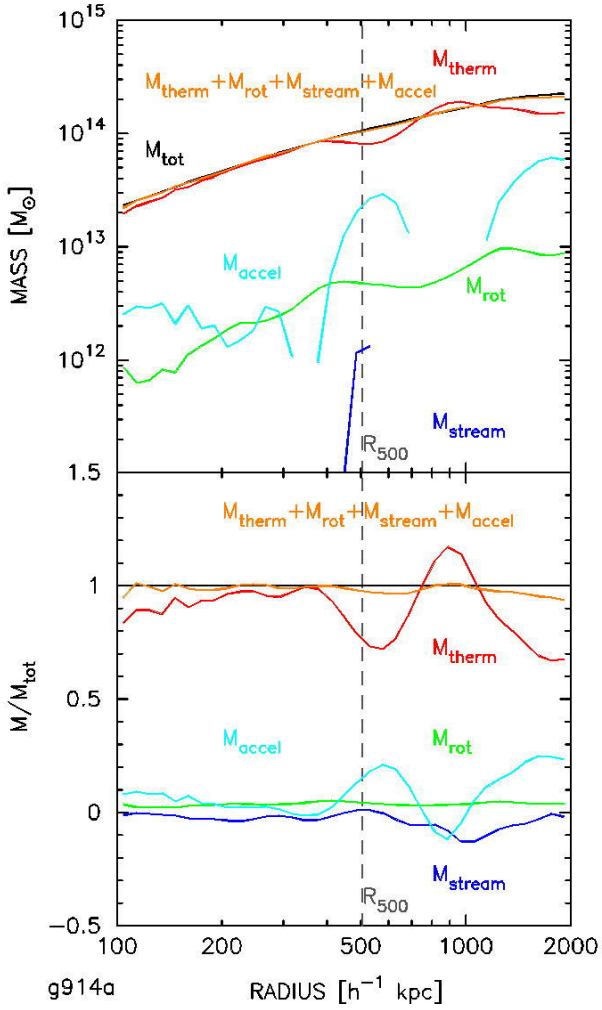

Figure 5.10: Same as Figure 5.5, but for the cluster g914a.

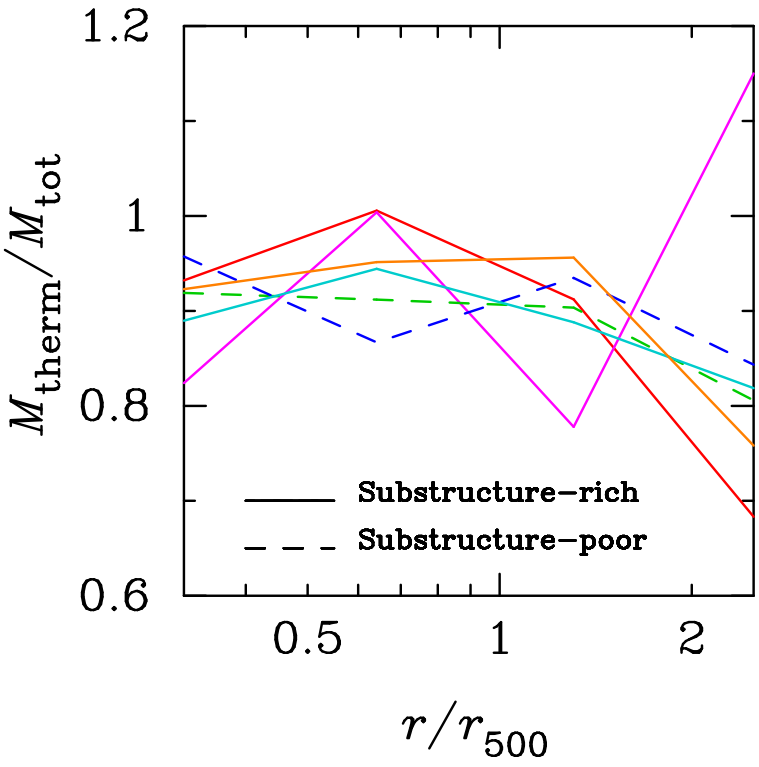

Figure 5.11: The ratio of $M_{\rm therm}$ to $M_{\rm tot}$ for the six simulated clusters: g1a (red), g72a (magenta), g1542a (green), g3344a (blue), g914a (cyan). To see the overall behavior, the radial bins are coarsely provided. The result for a cluster with/without big substructures is shown in solid/dashed line.

Chapter 6

BIASES IN MASS RECONSTRUCTION FROM 2D OBSERVABLES

In the previous chapter, we discussed the validity of the hydrostatic assumption in three-dimensional space. In real observations, however, we can obtain two-dimensional observables alone. The difference between the true mass and the HSE mass estimated from two dimensional observables can be larger (or smaller) than that in three dimensional analyses due to the projection effect, fitting procedures, etc. In this section, we investigate such effects using the same set of simulated clusters in the previous chapter. Throughout this chapter, we *do not* consider the influences of noises of specific observational instruments, since we are interested in the remaining biases even when such influences are removed.

6.1 Method

6.1.1 Simulated Observables

In real observations, the primary observables are the surface brightness I_X and the spectroscopic temperature $T_{\rm spec}$. We calculate the two observables from the simulation data. We use six simulated clusters: one from the AMR simulation in Section 4.1 (the AMR cluster) and five central clusters from SPH simulation in Section 4.2, namely, the clusters g1a, g72a, g1542a, g3344a, g914a.

The surface brightness I_X is defined as the energy loss rate integrated along the line of sight:

$$I_X = \frac{1}{4\pi} \int dl \; n_e n_i \Lambda(T), \tag{6.1}$$

where $\Lambda(T)$ is the cooling function and n_e and n_i are the electron and ion densities (In simulations, $n_e = n_i$). The line of sight is chosen as the z-axis in the simulations. We use the cooling function calculated using SPEX in the X-ray energy band (0.5 - 10 keV) under the assumption of the collisional ionization equilibrium. Figure 6.1 illustrates the bolometric and X-ray cooling curves as a function of temperature. The figure shows that low temperature gases ($T \lesssim 0.1$ keV) do not contribute to the X-ray cooling curve.

The temperature $T_{\rm spec}$ is determined spectroscopically in real observations. Although it is more faithful to real observations if we make mock spectra and estimate the temperature by

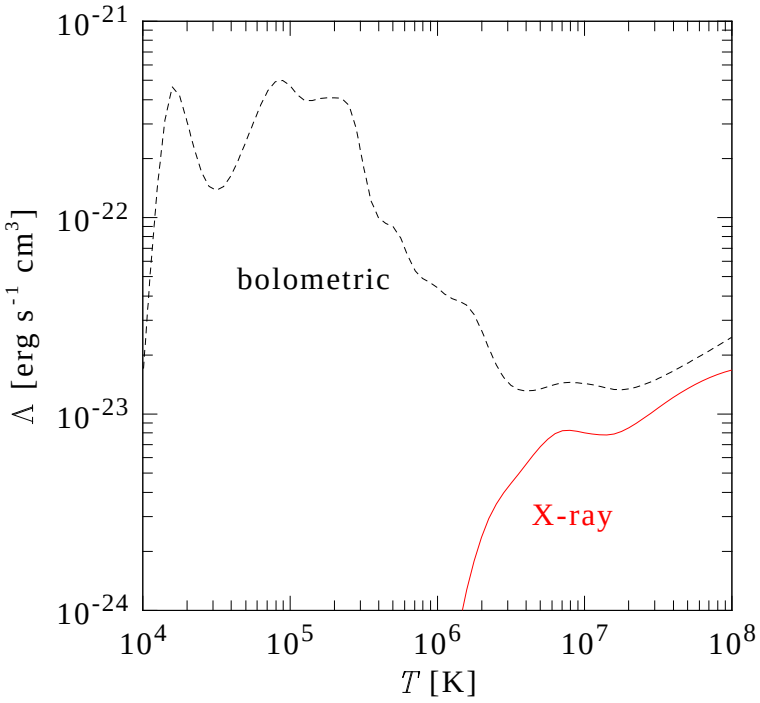

Figure 6.1: Bolometric and X-ray (0.5-10 keV) cooling functions calculated using SPEX. The metallicity is set to 0.3 $Z_\odot$.

spectral fitting, this procedure necessarily becomes dependent on specific observational telescopes and detectors, which we do not take into account in this study. Instead, we use the spectroscopic-like temperature $T_{\rm sl}$ proposed by Mazzotta et al. (2004):

$$T_{\rm sl} = \frac{\int dl\ n^2 T^{1/4}}{\int dl\ n^2 T^{-3/4}}. \tag{6.2}$$

Mazzotta et al. (2004) have shown that $T_{\rm sl}$ reproduces $T_{\rm spec}$ within a few percent for simulated clusters. The approximation is valid for higher temperatures larger than a few keV. Also, low temperature gases probably not contribute to the X-ray spectroscopic temperature, similarly to the surface brightness. Therefore, we remove by hand gases with temperatures lower than 0.1 keV.

Figure 6.2 is a density-temperature plot for gas particles around the cluster g1. The figure supports the validity of the removal of low-temperature gases since most of the particles have temperatures lower than 0.1 keV. Note that a little change of the fiducial temperature of 0.1 keV to, for example, 0.5 keV only slightly affect values of the simulated observables.

6.1.2 Fitting Formulae

Next, we find three-dimensional profiles which reproduce two-dimensional simulated observables. We determine a set of the best-fit parameters for simulated clusters assuming the following

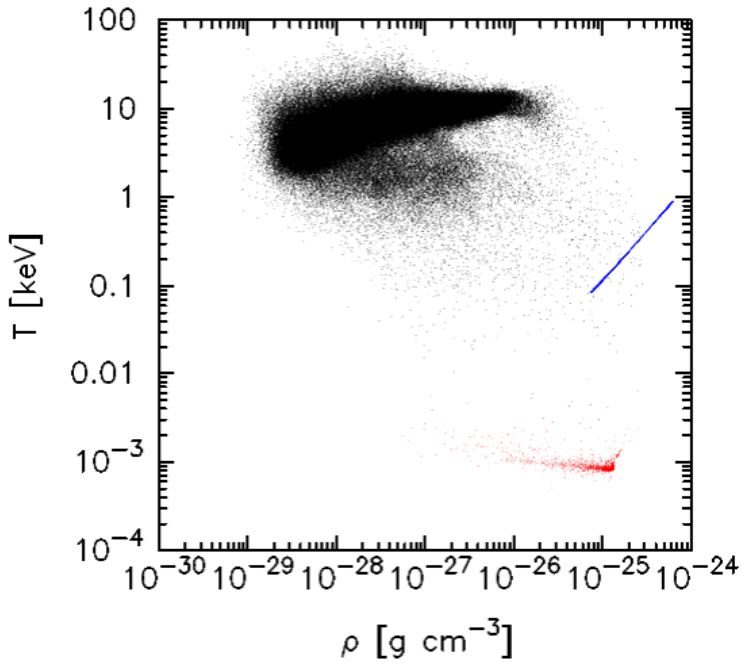

Figure 6.2: A density-temperature plot for SPH particles around the cluster g1a. The red and blue points represent unphysical particles, which are removed before analysis.

spherical profiles:

$$n^2(r) = n_0^2 \frac{(r/r_c)^{-\alpha}}{(1 + r^2/r_c^2)^{3\beta-\alpha/2}}, \tag{6.3}$$

$$T(r) = T_0 \frac{(r/r_t)^{-a}}{(1 + (r/r_t)^b)^{c/b}}. \tag{6.4}$$

These are simplified versions of the models used by Vikhlinin et al. (2006). The total number of parameters is nine. We prepare 25 logarithmically equal bins and calculate the circular averages of the simulated observables for each bin. In real observations, the number of radial bins depends on resolution of observational instruments, which we do not consider as mentioned above. Also, errors in values of observables depend on performance of instruments, thus we define them as ten percent for each value just for simplicity, since there is no error in simulated observables.

We have assumed the squared density profile (Equation (6.3)) since the observables depend on density only in the form n^2. The observables include fluctuations in density and hence easily affected by substructures. Therefore the radial density profile $n(r)$ can be significantly different from the square root of $n^2(r)$.

After the best-fit density and temperature profiles are found, we calculate mass of the cluster from the profiles assuming hydrostatic equilibrium. In this chapter, we call the mass obtained from this process $M_{\rm fit}$. If the three-dimensional density and temperature are correctly estimated by fitting, the mass reproduces the three-dimensional HSE mass $M_{\rm therm}$. Hence the difference between $M_{\rm fit}$ and $M_{\rm therm}$ indicates the bias in mass estimation from the two-dimensional observables. On the other hand, the difference between $M_{\rm fit}$ and $M_{\rm tot}$ means the bias in observationally estimated mass as a combination of the intrinsic violation of HSE and the effects of the two-dimensionality of the observables.

6.2 Results

Figures 6.3 – 6.8 demonstrate the results of the analysis for six simulated clusters. As the contour maps of the surface brightness indicate, the AMR, g1a, g72a and g914a clusters have big substructures, which appear as peaks in the radial profiles of the surface brightness. The density and temperature profiles are, however, well fitted by Equations (6.3) and (6.4). Hence, the mass constructed from the best-fit profiles (the blue line in the bottom-left panel) reproduces the three-dimensional HSE mass (the red line in the bottom-left panel). From these figures, it seems that the mass $M_{\rm fit}$ well reproduces the three-dimensional HSE mass $M_{\rm therm}$, i. e., there is little biases in mass reconstruction from the two-dimensional observables. To see more quantitatively, we compare $M_{\rm fit}$ with $M_{\rm therm}$ or $M_{\rm tot}$ using coarse radial bins.

Figure 6.9 shows the ratio of $M_{\rm fit}$ to $M_{\rm therm}$. This figure reveals a significant difference between substructure-rich/poor clusters which is not seen in three-dimensional analysis in Chapter 5. For substructure-poor clusters, $M_{\rm fit}/M_{\rm therm}$ lies between 0.95 – 1.05 at all radii. This means that there is little biases in mass construction from the two-dimensional observables for substructure-poor clusters. On the other hand, $M_{\rm fit}/M_{\rm therm}$ deviates from unity especially at large radii for substructure-rich clusters. Since it is shown in Chapter 5 that $M_{\rm therm}$ underestimates $M_{\rm tot}$, this results in the further underestimation of mass at large radii as shown in Figure 6.10.

This difference can be qualitatively explained as follows. If there is a substructure with high temperature and density, the surface brightness around the substructure becomes significantly larger than that without the substructure. This leads to overestimate of the density profile in the outermost regions, and hence underestimate of the pressure gradient and temperature (If the density is higher, the temperature must be lower to reproduce the same value of the spectroscopic-like temperature). Hence the HSE mass is underestimated.

To confirm the effect of substructures, we calculate radial profiles of the surface brightness and spectroscopic-like temperature for the cluster g72a only from the domain $x < 0$, $y < 0$ which has no big substructures and the domain $x > 0$, $y < 0$ which has big substructures. We call these domains "SE" (south-east), "SW" (south-west), respectively. Using these radial profiles, we estimate the mass by the same method as above. The results are shown in Figures 6.11 to 6.13. The ratios of $M_{\rm fit}$ to the three-dimensional HSE mass and total mass for "SW" are similar to those of the entire cluster. Meanwhile, the ratio of $M_{\rm fit}$ to $M_{\rm tot}$ for "SE" is closer to unity. This behavior is similar to the clusters with no substructures in Figure 6.10. The ratio of $M_{\rm fit}$ to $M_{\rm therm}$ for "SE" is larger than that of the entire cluster at large radii ($\gtrsim r_{500}$). Although there are still large deviations from unity ($> 50\%$) around $3r_{500}$, the overall behavior is similar to the clusters with no substructures in that it exhibits up-and-down behavior around unity. These results indicate that the large deviations of $M_{\rm fit}$ from the three-dimensional HSE mass and total mass at large radii are due to substructures. It is not, however, that the domain "SW" exhibits larger deviations than the entire cluster. Although this method to investigate the effect of substructures is simple, the result indicates the tendency of substructures to lead underestimation of mass.

The above results indicate that we have to pay attention to substructures when we observationally estimate mass of clusters. Note that conventional observations of clusters is limited to inside the radius r_{500}, so the effect of substructures discussed above would not appear in mass estimates in previous literature (e.g. Vikhlinin et al., 2006).

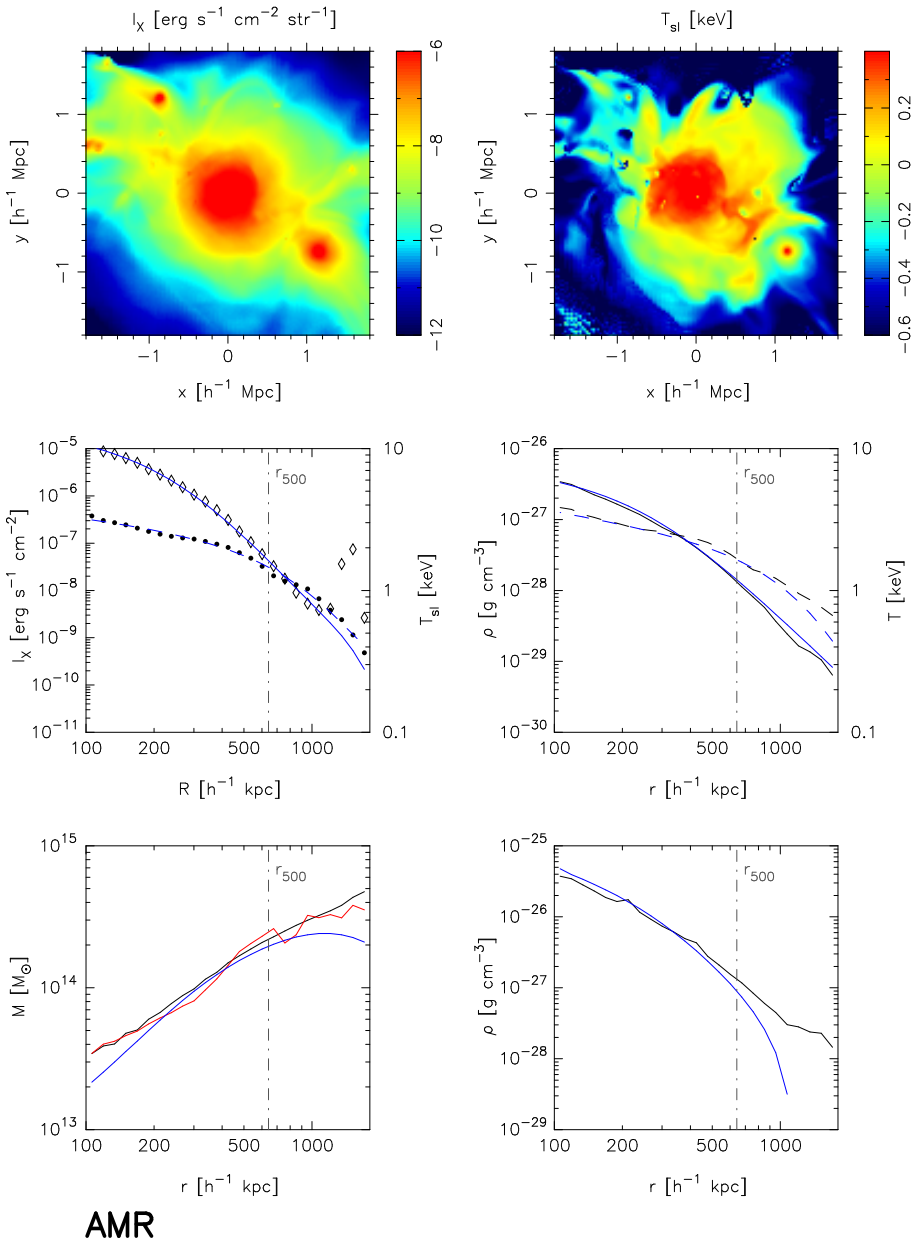

Figure 6.3: Results of the analysis in Chapter 6 for the AMR cluster. Contours for the surface bright ness and the spectroscopic-like temperature are shown at the top-left and the top-right, respectively. The line of sight is chosen as the z-axis of the simulation box. The middle left panel shows the result of fitting. The open diamonds and filled circles represent the circular average values of the surface brightness and spectroscopic-like temperature, respectively. The solid and dashed lines are the best-fit profiles. The density (solid) and temperature (dashed) profiles with the best-fit parameters are shown in blue lines in the middle-right panel. For comparison, the three-dimensional density (solid) and temperature (dashed) profiles are shown in black lines. The HSE mass obtained from the best-fit parameters is the blue line in the bottom-left panel. The bottom-left panel also illustrates the true mass (black) and HSE mass (red) calculated from the three-dimensional data. The bottom-right panel is a comparison of the total density profile with best-fit parameters (blue) with the true profile (black).

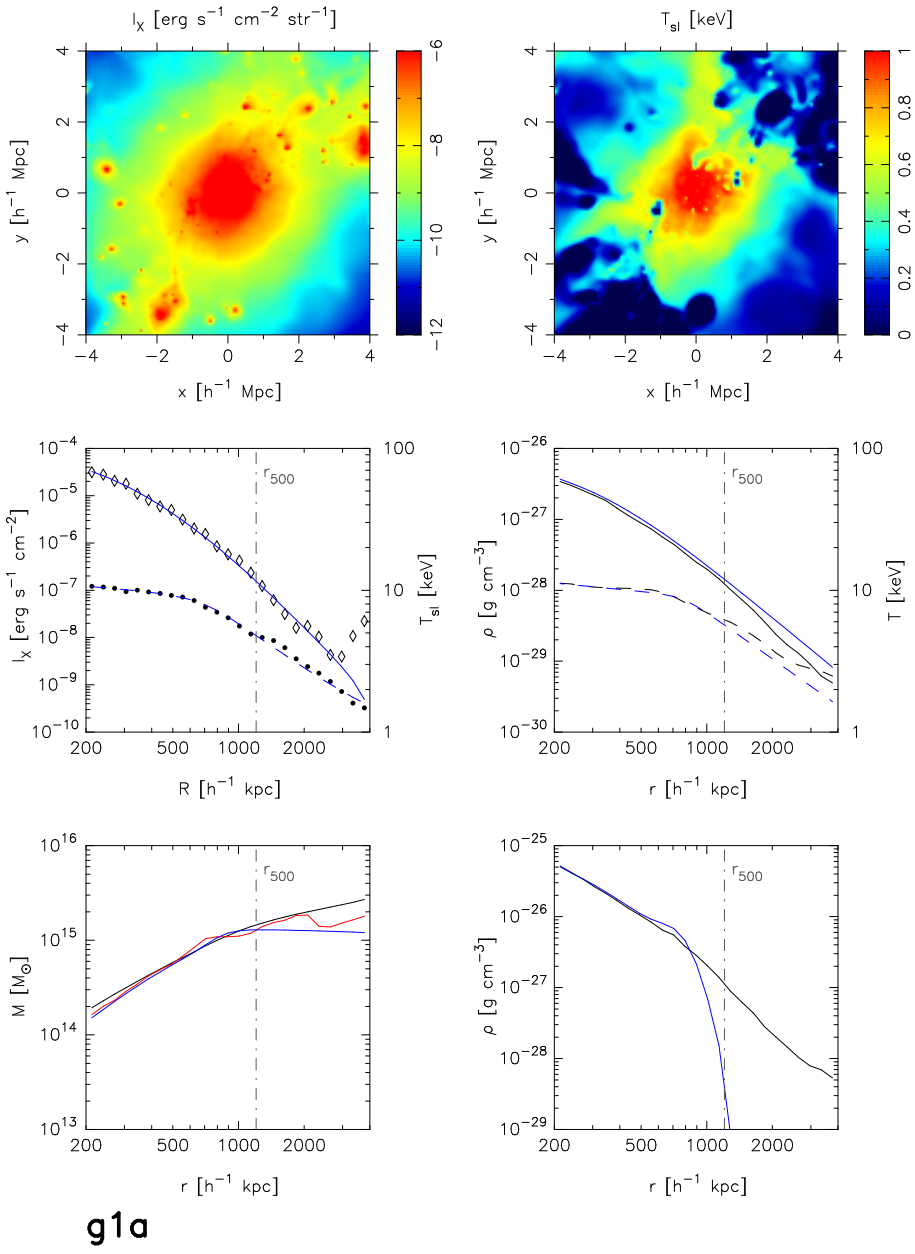

Figure 6.4: Same as Figure 6.3, but for the cluster g1a.

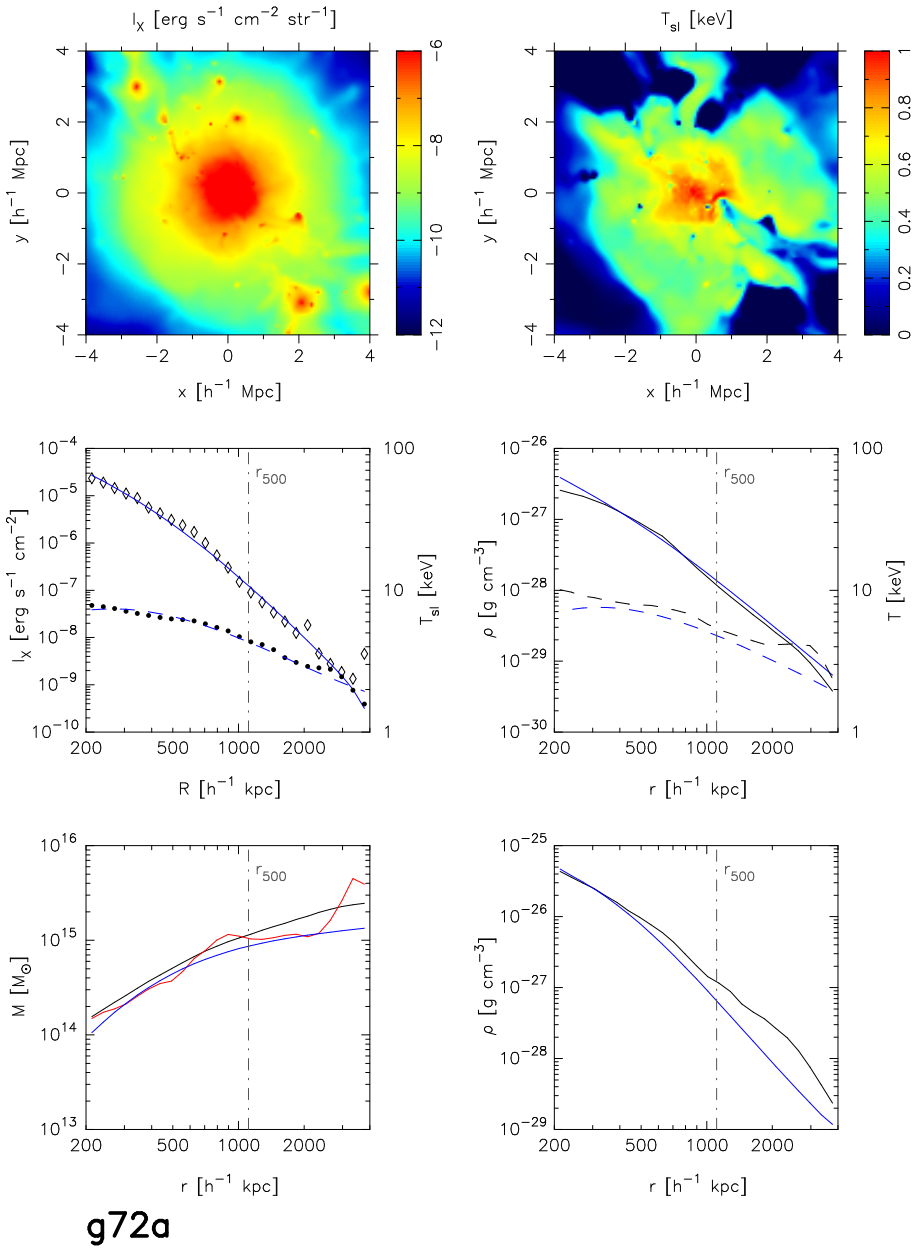

Figure 6.5: Same as Figure 6.3, but for the cluster g72a.

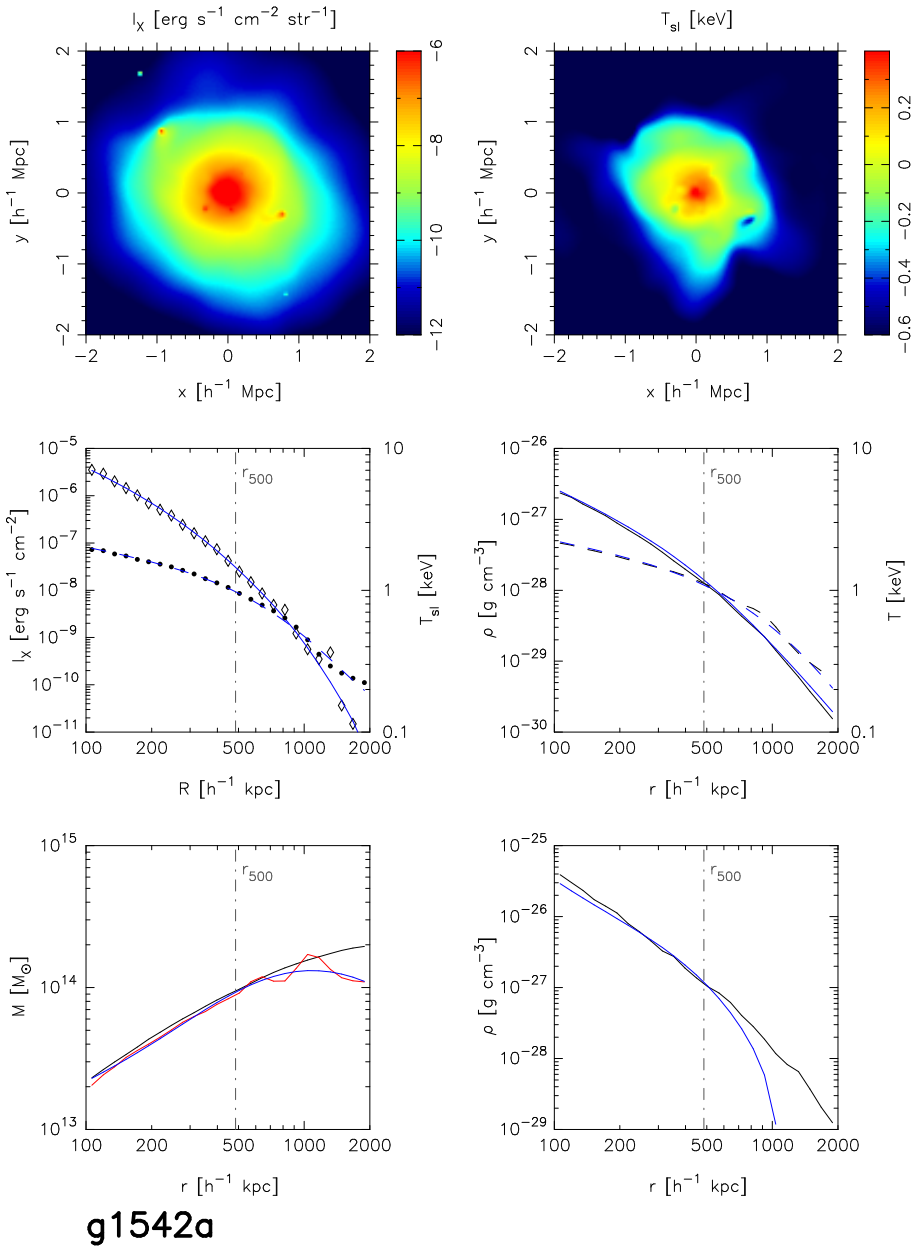

Figure 6.6: Same as Figure 6.3, but for the cluster g1542a.

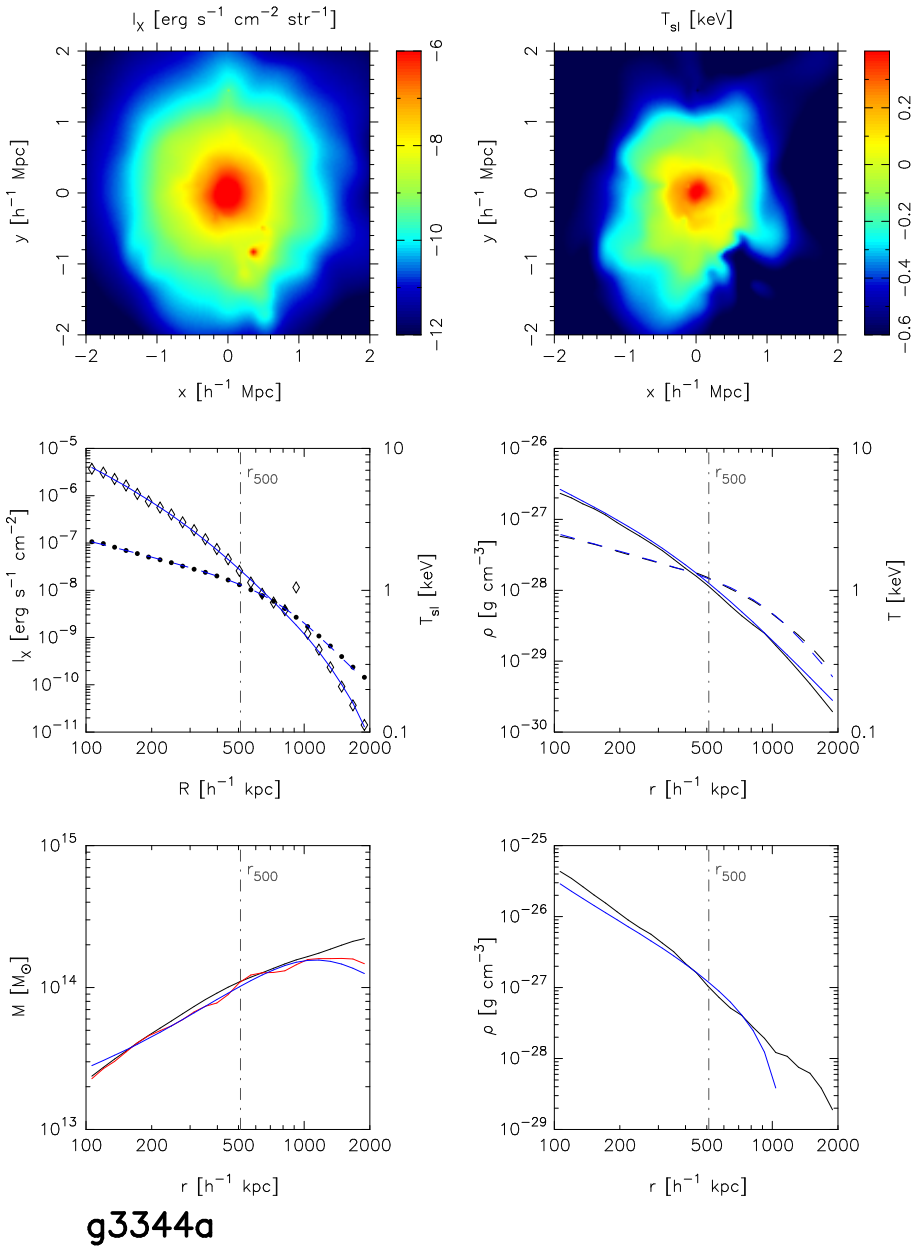

Figure 6.7: Same as Figure 6.3, but for the cluster g3344a.

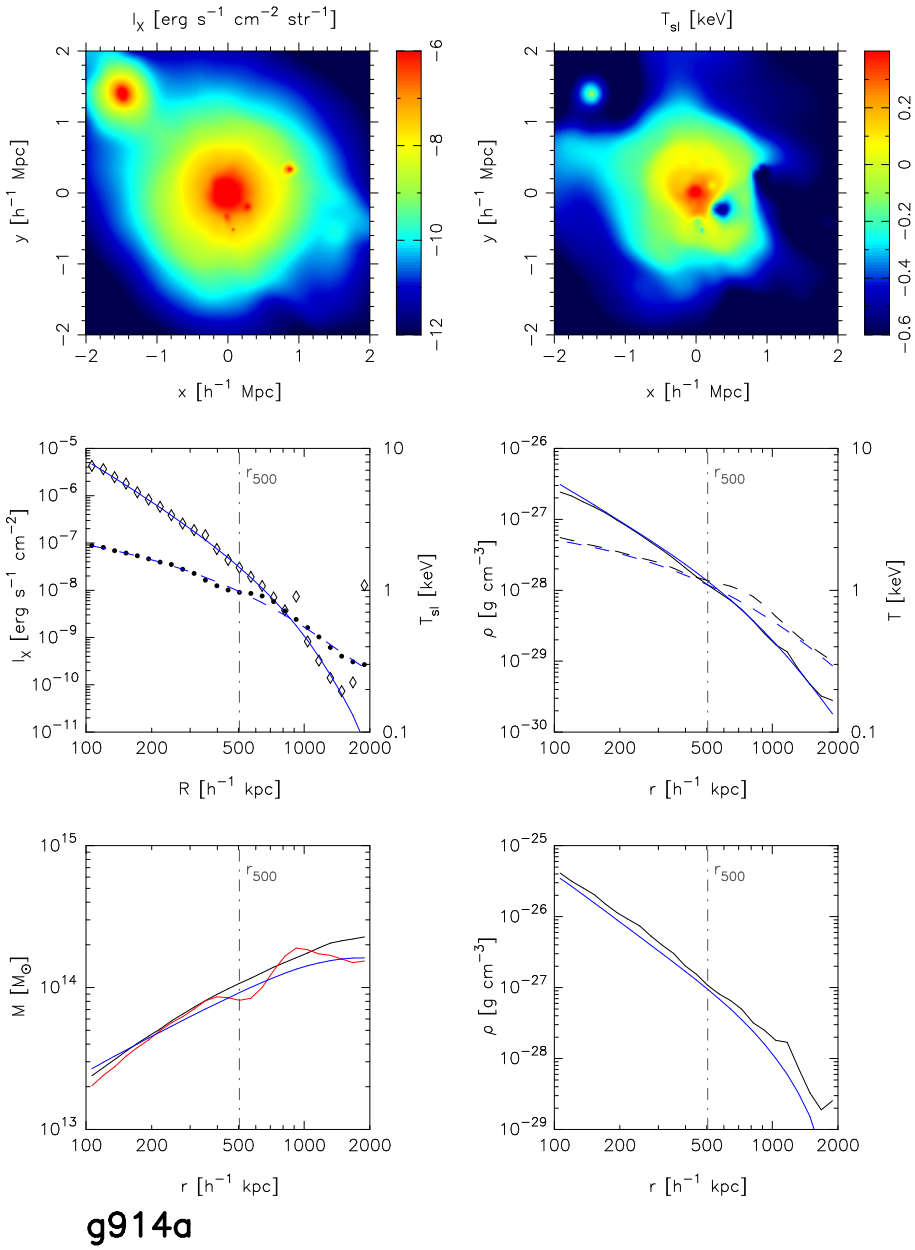

Figure 6.8: Same as Figure 6.3, but for the cluster g914a.

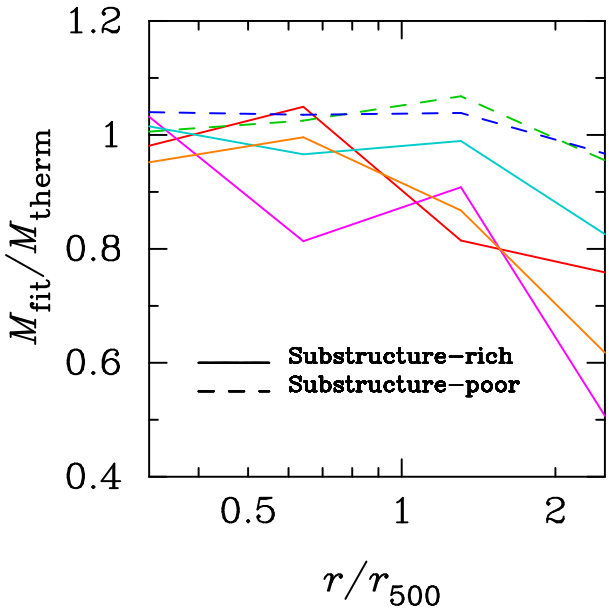

Figure 6.9: The ratio of the mass $M_{\rm fit}$ constructed from the best-fit density and temperature profiles to the HSE mass $M_{\rm therm}$ directly calculated from the three-dimensional data: g1a (red), g72a (magenta), g1542a (green), g3344a (blue), g914a (cyan) and the AMR cluster (orange). The horizontal axis represents radius normalized by r_{500} of each cluster. The solid lines are for substructure-rich clusters, and the dashed lines are for substructure-poor clusters.

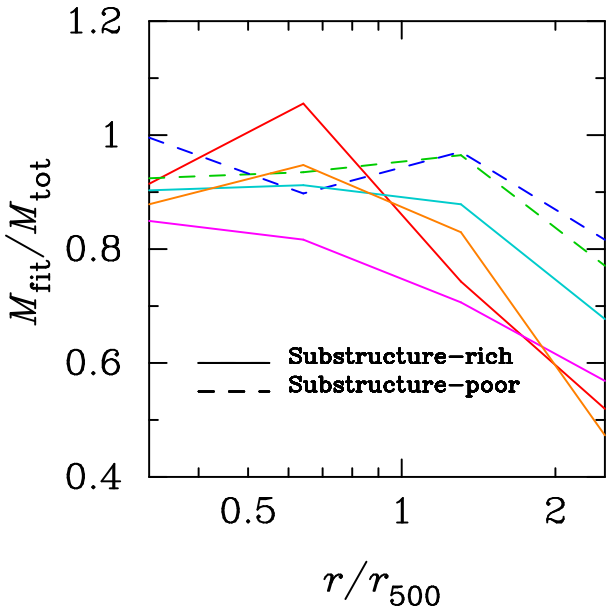

Figure 6.10: The ratio of the mass $M_{\rm fit}$ constructed from the best-fit density and temperature profiles to the total mass $M_{\rm tot}$ directly calculated from the three-dimensional density data: g1a (red), g72a (magenta), g1542a (green), g3344a (blue), g914a (cyan) and the AMR cluster (orange). The horizontal axis represents radius normalized by r_{500} of each cluster. The solid lines are for substructure-rich clusters, and the dashed lines are for substructure-poor clusters.

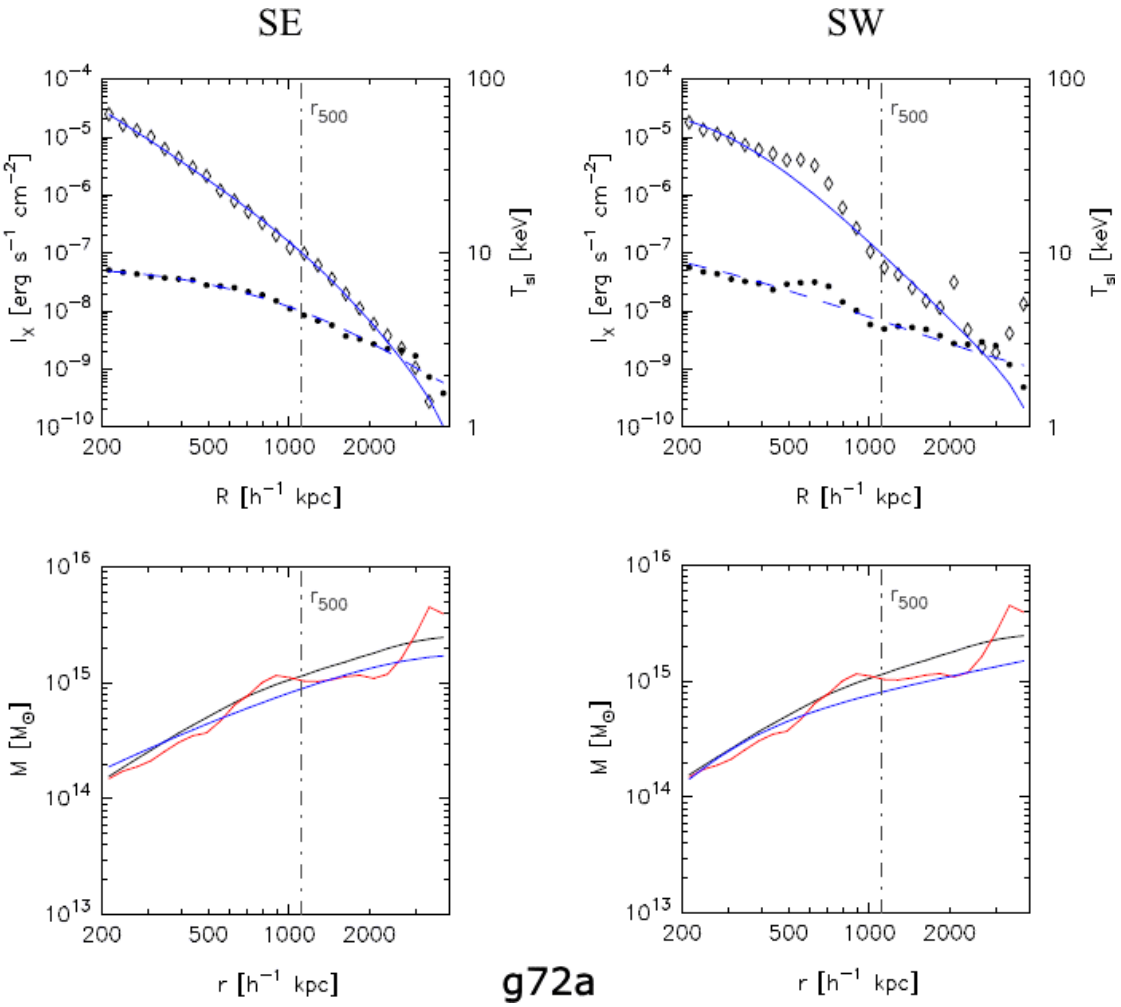

Figure 6.11: The same as the middle-left and bottom-left panels of Figure 6.3, but for the radial profiles calculated from the domains "SE" (left) and "SW" (right) of the cluster g72a.

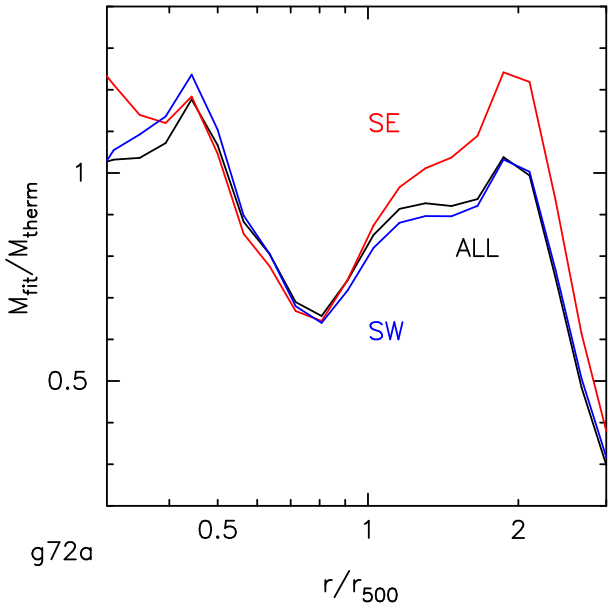

Figure 6.12: The ratio of the mass constructed from the best-fit density and temperature profiles to the HSE mass directly calculated from the three-dimensional data. The black line is for the entire cluster the g72a. The red and blue lines are for the domains "SE" and "SW", respectively.

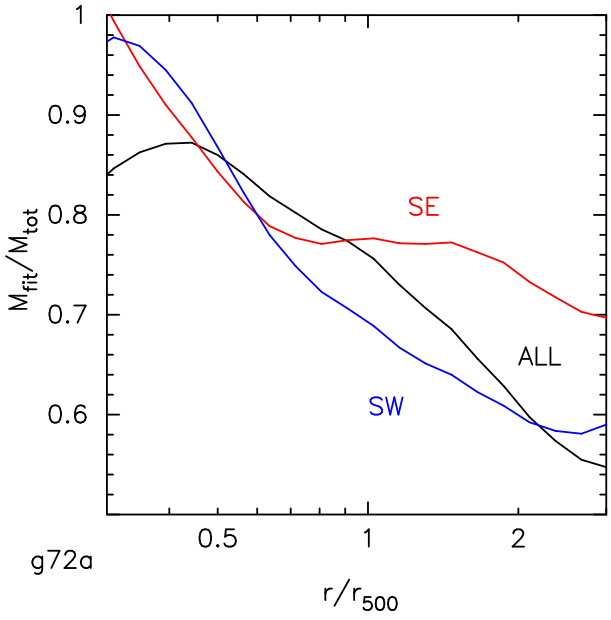

Figure 6.13: The ratio of the mass constructed from the best-fit density and temperature profiles to the total mass directly calculated from the three-dimensional data. The black line is for the entire cluster the g72a. The red and blue lines are for the domains "SE" and "SW", respectively.

Chapter 7

SUMMARY AND CONCLUSION

We have examined the validity of HSE that has been conventionally assumed in estimating mass of galaxy clusters from X-ray observations.

In Chapter 5 we investigated the intrinsic difference between the true and HSE mass using three-dimensional simulation data. We used 12 simulated clusters and evaluate several mass terms directly corresponding to the Euler equations that govern the gas dynamics in numerical simulations. We found that the mass estimated under the HSE assumption, $M_{\rm therm}$ in the present study, deviates from the true mass $M_{\rm tot}$ fractionally by up to 30 %. The deviation can become large both in the inner and outer regions of the clusters. On average (when coarser radial bins are used), $M_{\rm therm}$ is smaller than $M_{\rm tot}$ by $\sim (10--15)$ % on average within r_{500} and by $\sim (20--30)$ % at larger radii. Therefore the the HSE mass obtained in X-ray observations systematically underestimates the true mass even if the density and temperature are correctly estimated.

More importantly, we found that $M_{\rm tot} - M_{\rm therm}$ is nearly identical to $M_{\rm accel}$, in other words, the validity of HSE is controlled by the amount of gas acceleration. We also showed that the estimate of $M_{\rm accel}$ by $M_{\rm tot} - M_{\rm therm} - M_{\rm rot} - M_{\rm stream}$ is a good approximation of $M_{\rm accel}$ calculated directly from gas acceleration data. There are cases where $M_{\rm tot} - M_{\rm therm}$ is explained by $M_{\rm rot}$, i.e., the rotation of the gas, but $M_{\rm tot} - M_{\rm therm}$ is relatively small ($\lesssim 10$ %) there. In other words, the large deviations of $M_{\rm therm}$ from $M_{\rm tot}$ is generally attributed to $M_{\rm accel}$.

The overall conclusion that the HSE mass agrees with the total mass within (10 – 20)% is consistent with previous results by Fang et al. (2009) and Lau et al. (2009). Nevertheless the interpretation of the origin of the departure from HSE is very different. Fang et al. (2009) concluded that the gas rotation term $M_{\rm rot}$ makes a significant contribution and that $M_{\rm therm} + M_{\rm rot}$ well reproduces the total mass, especially for relaxed clusters. It is not the case, however, for our simulated cluster at least. Similarly Lau et al. (2009) found the similar degree of the departure from HSE, but they ascribed the discrepancy to the random gas motion. Their analysis, however, is based on the modification of the Jeans equations, which does not appear to be justified for the analysis of the gas dynamics, and thus their conclusion should be interpreted with caution.

Although we tested the roles of the velocity and acceleration of gases, they are not measured in current observations. Some future satellites, such as ASTRO-H, are expected to be able to obtain information on gas velocity. It is not clear, however, how accurately we can estimate the velocity and how to apply it in mass estimates, which will be discussed somewhere.

In Chapter 6, we investigated biases in the HSE mass estimated from two-dimensional observables. We showed that there is only a little influence of projection and fitting procedure. If a cluster has some significant substructures in outermost regions, the mass at large radii will be

underestimated since the larger surface brightness due to the substructures leads an underestimate of pressure gradient. This would not, however affect mass estimations in previous work because current observations are limited to inside the radius r_{500}. In other words, in future work which includes observations of outer regions of clusters, substructures should be carefully treated.

The analysis using only south-east and south-west parts of the cluster g72a indicates that the use of the substructure-poor region or removal of substructures will provide better estimation of mass. However, whether substructures can be identified and removed depends on the resolution of observational instruments, especially for distant clusters. The discussion including limitations from observational instruments remains as future work.

A relatively small systematic error of the HSE mass inferred from current numerical simulations may be partly ascribed to the assumptions inherent in the Euler equations, i.e., local thermal equilibrium and negligible viscosity (Appendix B). This is supported by the fact that the error in the mass estimated from the random motion of collisionless particles tends to be much greater at large radii (Appendix C) because the relaxation time scale for collisionless particles are appreciably longer than that for collisional gas. We should also note that the HSE mass can be influenced by other physical precesses that are not included in the numerical simulations, such as pressure support from micro-turbulence, the magnetic field, and accelerated particles (e.g., Laganá et al., 2010). The neglected components mentioned above are closely linked with one another (e.g., viscosity can play a role in generating turbulence and the magnetic field can affect both thermalization and acceleration of gas particles) and will be investigated in the near future by X-ray missions such as NuSTAR[1] and ASTRO-H as well as by radio telescopes including EVLA[2] and LOFAR[3].

[1] http://www.nustar.caltech.edu
[2] http://www.aoc.nrao.edu/evla
[3] http://www.lofar.org

Appendix A

SPHERICAL COLLAPSE MODEL IN NON-EINSTEIN-DE SITTER UNIVERSES

In this appendix, we show $\delta_c^{\rm linear}$ in the spherical collapse model (Section 2.5) has only a weak dependence on the model of the universe. The following discussion is based on Nakamura & Suto (1997).

A.1 Open Universe

We consider an open universe, i.e., $\Omega_m + \Omega_K = 1$, $\Omega_m < 1$. For simplicity, we set the scale factor $a(t_v) = a_v = 1$ at the time t_v when the system settles into virial equilibrium. We use in this section Ω as Ω_m, then $\Omega_K = 1 - \Omega$. The time-dependence of the scale factor can be parametrically written as

$$\begin{aligned} H_v t &= \frac{\Omega_v}{2(1-\Omega_v)^{3/2}}(\sinh\eta - \eta), \\ a &= \frac{\Omega_v}{2(1-\Omega_v)}(\cosh\eta - 1), \end{aligned} \tag{A.1}$$

where the subscript v denotes the values at the time t_v. Since $a_v = 1$,

$$\Omega_v = \frac{2}{\cosh\eta_v + 1}, \quad 1 - \Omega_v = \frac{\cosh\eta_v - 1}{\cosh\eta_v + 1}. \tag{A.2}$$

It can also be easily shown that

$$Ht = \frac{\sinh\eta(\sinh\eta - \eta)}{(\cosh\eta - 1)^2}. \tag{A.3}$$

A sphere of mass M and radius $r(t)$ follows the following equation of motion:

$$\frac{d^2 r}{dt^2} = -\frac{GM}{r^2}. \tag{A.4}$$

The curvature of the universe does not change the equation of motion and we include it in the energy of the system. The energy equation is

$$\frac{1}{2}\left(\frac{dr}{dt}\right)^2 - \frac{GM}{r} = E, \tag{A.5}$$

where the energy E is defined at the turn-around time t_t:

$$E = -\frac{GM}{r_t}. \tag{A.6}$$

Integrating the energy equation, one obtains

$$Ht = \frac{H}{\sqrt{2GM}} \int_0^r dr' \left(\frac{1}{r'} - \frac{1}{r_t}\right)^{-1/2} = \xi^{1/2} \int_0^y dx \sqrt{\frac{x}{1-x}}, \tag{A.7}$$

where

$$y = \frac{r}{r_t}, \quad \xi = \frac{r_t^3 H^2}{2GM}. \tag{A.8}$$

Note that ξ has a time-dependence through H. The density contrast δ is given by

$$\begin{aligned} \delta &= \frac{\rho}{\bar{\rho}} - 1 = \frac{3M}{4\pi\bar{\rho}r^3} - 1 \\ &= (\Omega y^3 \xi)^{-1} - 1 = \frac{\cosh\eta + 1}{2} \frac{1}{y^3\xi} - 1. \end{aligned} \tag{A.9}$$

The collapse time is given by

$$H_v t_v = 2\xi_v^{1/2} \int_0^1 dx \sqrt{\frac{x}{1-x}} = \pi \xi_v^{1/2}. \tag{A.10}$$

Using Equation (A.3), one obtains

$$\xi_v = \frac{1}{\pi^2} \frac{\sinh^2\eta_v (\sinh\eta_v - \eta_v)^2}{(\cosh\eta_v - 1)^4}. \tag{A.11}$$

From the virial theorem, $y_v = 1/2$, hence

$$\delta_c = 4\pi^2 \frac{(\cosh\eta_v - 1)^3}{(\sinh\eta_v - \eta_v)^2} - 1. \tag{A.12}$$

This is the density contrast at the collapse time in the non-linear theory.

Next we calculate δ_c in the linear regime. In the early stages, $y \ll 1$ and $\eta \ll 1$, then Equations (A.3) and (A.7) give

$$Ht \simeq \frac{2}{3}\left(1 + \frac{1}{20}\eta^2\right) \tag{A.13}$$

and

$$Ht \simeq \frac{2}{3}\xi^{1/2} y^{3/2} \left(1 + \frac{3}{10} y\right). \tag{A.14}$$

Equating (A.13) with (A.14) gives y iteratively:

$$y \simeq \xi^{-1/3} \left(1 - \frac{1}{5}\xi^{-1/3} + \frac{1}{30}\eta^2\right). \tag{A.15}$$

Combining all the above results, the initial density contrast δ_i is given by

$$\delta_i \simeq \left(1 + \frac{1}{4}\eta^2\right) \frac{1}{y^3\xi} - 1 \simeq \frac{3}{5}\left(\xi^{-1/3} + \frac{1}{4}\eta^2\right). \tag{A.16}$$

Since $\eta^2/4 \simeq (\Omega_v^{-1} - 1)a$ and $\xi \propto H^2$,

$$\delta_i \simeq \frac{3}{10} a(\cosh\eta_v - 1)\left[1 + \left(\frac{2\pi}{\sinh\eta_v - \eta_v}\right)^{2/3}\right], \tag{A.17}$$

showing that $\delta_i \propto a$ as predicted by the linear theory. Since the linear growth rate D_+ in an open universe is given by

$$\begin{aligned} D_+ &= \frac{5}{2}\frac{a\Omega}{1-\Omega}\left[\frac{1+2\Omega}{1-\Omega} - \frac{3\Omega}{(1-\Omega)^{3/2}}\tanh^{-1}\sqrt{1-\Omega}\right] \\ &= \frac{5a}{\cosh\eta - 1}\left[\frac{3\sinh\eta(\sinh\eta - \eta)}{(\cosh\eta - 1)^2} - 2\right], \end{aligned} \tag{A.18}$$

the density contrast $\delta_c^{\rm linear}$ at the collapse time is given by

$$\delta_c^{\rm linear} = \frac{3}{2}\left[\frac{3\sinh\eta_v(\sinh\eta_v - \eta_v)}{(\cosh\eta_v - 1)^2} - 2\right]\left[1 + \left(\frac{2\pi}{\sinh\eta_v - \eta_v}\right)^{2/3}\right]. \tag{A.19}$$

A.2 Flat Universe

Next we consider a flat universe, i.e., $\Omega_m + \Omega_\Lambda = 1$, $\Omega_m < 1$. For simplicity, we set the scale factor $a(t_v) = a_v = 1$ at the time t_v when the system settles into virial equilibrium. We use in this section Ω as Ω_m, then $\Omega_\Lambda = 1 - \Omega$. The time-dependence of the scale factor can be parametrically written as

$$\begin{aligned} H_v t &= \frac{1}{3}(1-\Omega_v)^{-1/2}\cosh^{-1}(1+2\chi), \\ a &= \left(\frac{\Omega_v}{1-\Omega_v}\right)^{1/3}\chi^{1/3}, \end{aligned} \tag{A.20}$$

where the subscript v denotes the values at the time t_v. Since $a_v = 1$,

$$\Omega_v = \frac{1}{1+\chi_v}, \quad 1 - \Omega_v = \frac{\chi_v}{1+\chi_v}. \tag{A.21}$$

It can also be easily shown that

$$Ht = \frac{1}{3}\left(\frac{1+\chi}{\chi}\right)^{1/2}\cosh^{-1}(1+2\chi). \tag{A.22}$$

A sphere of mass M and radius $r(t)$ follows the following equation of motion:

$$\frac{d^2r}{dt^2} = -\frac{GM}{r^2} + \frac{\Lambda}{3}r. \tag{A.23}$$

Integrating Equation (A.23) gives the energy equation:

$$\frac{1}{2}\left(\frac{dr}{dt}\right)^2 - \frac{GM}{r} - \frac{\Lambda}{6}r^2 = E, \tag{A.24}$$

where the energy E is defined at the turn-around time t_t:

$$E = -\frac{GM}{r_t} - \frac{\Lambda}{6}r_t^2. \tag{A.25}$$

Integrating the energy equation, one obtains

$$Ht = \zeta^{1/2}\left(\frac{1+\chi}{\chi}\right)\int_0^y dx\ \left[\frac{1}{x} - (1+\zeta) + \zeta x^2\right]^{-1/2}, \tag{A.26}$$

where

$$y = \frac{r}{r_t}, \quad \zeta = \frac{r_t^3\Lambda}{6GM}. \tag{A.27}$$

Note that ζ is time-independent. In order for the sphere to turn around, i.e., the integrand of Equation (A.26) does not diverge in the range $0 < x < 1$, ζ must satisfy $0 < \zeta < 1/2$. The density contrast δ is given by

$$\delta = \frac{\rho}{\bar{\rho}} - 1 = \frac{3M}{4\pi\bar{\rho}r^3} - 1 = \frac{\chi}{y^3\zeta} - 1. \tag{A.28}$$

The collapse time is given by

$$H_v t_v = 2\zeta^{1/2}\left(\frac{1+\chi_v}{\chi_v}\right)\int_0^1 dx\ \left[\frac{1}{x} - (1+\zeta) + \zeta x^2\right]^{-1/2}. \tag{A.29}$$

Now we replacing the variable x by

$$x = \frac{(2-\zeta-\lambda)t^2}{2[1+2\zeta-(3\zeta+\lambda-1)t^2]}, \tag{A.30}$$

where

$$\lambda = \sqrt{4\zeta+\zeta^2}. \tag{A.31}$$

Then $H_v t_v$ can be expressed as

$$H_v t_v = \frac{4(\zeta+\lambda)}{\sqrt{(\lambda+3\zeta)(\lambda-\zeta)}}\left[\Pi(\nu,k) - K(k)\right], \tag{A.32}$$

where $K(k)$ and $\Pi(\nu,k)$ are the elliptic integrals of the first and third kinds characterized by

$$k^2 = \frac{4\lambda\zeta}{(\lambda+3\zeta)(\lambda-\zeta)}, \quad \nu = \frac{2\zeta}{\lambda+3\zeta}. \tag{A.33}$$

Using Equation (A.22), one obtains

$$\chi_v = \frac{1}{2}\left[\cosh\left(\frac{12(\zeta+\lambda)}{\sqrt{(\lambda+3\zeta)(\lambda-\zeta)}}\left[\Pi(\nu,k) - K(k)\right]\right) - 1\right]. \tag{A.34}$$

From the virial theorem,

$$\langle U_m\rangle_t + \langle U_\Lambda\rangle_t = \frac{1}{2}\langle U_m\rangle_v + 2\langle U_\Lambda\rangle_v, \tag{A.35}$$

which gives

$$4\zeta y_v^3 - 2(1+\zeta)y_v + 1 = 0. \tag{A.36}$$

Equation (A.36) has a solution in the range $0 < y_v < 1$:

$$y_v = \left(\frac{2+2\zeta}{3\zeta}\right)^{1/2}\cos\left[\frac{2}{3}\pi - \frac{1}{3}\cos^{-1}\left\{-\frac{1}{\zeta}\left(\frac{3\zeta}{2+2\zeta}\right)^{3/2}\right\}\right]. \tag{A.37}$$

Combining all the above results,

$$\delta_c = \frac{\chi_v}{y_v^3 \zeta} - 1, \tag{A.38}$$

where w_v and y_v are given by Equations (A.34) and (A.37), respectively. This is considered to be the density contrast at the collapse time in the non-linear theory.

Next we calculate δ_c in the linear regime. In the early stages, $y \ll 1$ and $\eta \ll 1$, then Equations (A.22) and (A.26) give

$$Ht \simeq \frac{2}{3}(1+\chi)^{1/2} \tag{A.39}$$

and

$$Ht \simeq \frac{2}{3}\zeta^{1/2}\left(\frac{1+\chi}{\chi}\right)^{1/2} y^{3/2}\left[1 + \frac{3}{10}(1+\zeta)y\right]. \tag{A.40}$$

Equating (A.39) with (A.40) gives y iteratively:

$$y \simeq \left(\frac{\chi}{\zeta}\right)^{1/3}\left[1 - \frac{1}{5}(1+\zeta)\left(\frac{\chi}{\zeta}\right)^{1/3}\right]. \tag{A.41}$$

Combining all the above results, the initial density contrast δ_i is given by

$$\delta_i \simeq \frac{3}{5}(1+\zeta)\left(\frac{\chi}{\zeta}\right)^{1/3} = \frac{3}{5}a(1+\zeta)\left(\frac{\chi_v}{\zeta}\right)^{1/3}, \tag{A.42}$$

showing that $\delta_i \propto a$ as predicted by the linear theory. Since the linear growth rate D_+ in an open universe is given by

$$D_+ = a\,{}_2F_1\left(1, \frac{1}{3}, \frac{11}{6}; -\chi\right), \tag{A.43}$$

the density contrast $\delta_c^{\rm linear}$ at the collapse time is given by

$$\delta_c^{\rm linear} = \frac{3}{5}\,{}_2F_1\left(1, \frac{1}{3}, \frac{11}{6}; -\chi_v\right)(1+\zeta)\left(\frac{\chi_v}{\zeta}\right)^{1/3}. \tag{A.44}$$

Figures A.1 and A.2 illustrate δ_c and $\delta_c^{\rm linear}$ as functions of the current density parameters. Figure A.2 shows that $\delta_c^{\rm linear}$ is insensitive to cosmology models.

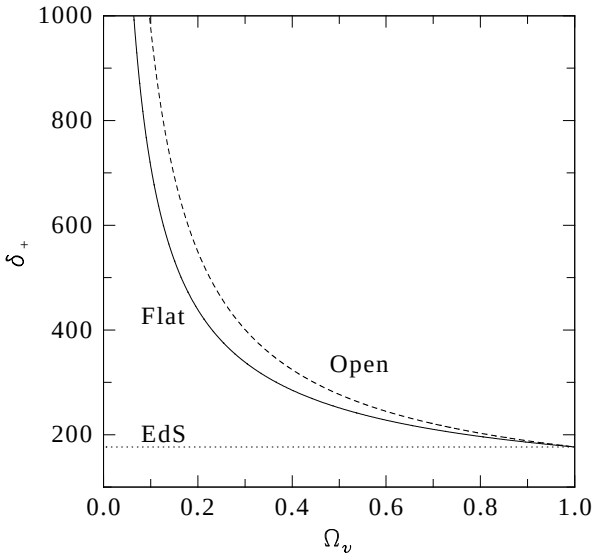

Figure A.1: The density contrast when the system gets into virial equilibrium for three sets of cosmological parameters: ($\Omega_{m,0}$, $\Omega_{\Lambda,0}$)=(0.3, 0.7) (solid), (0.3, 0) (dashed) and (1, 0) (dotted).

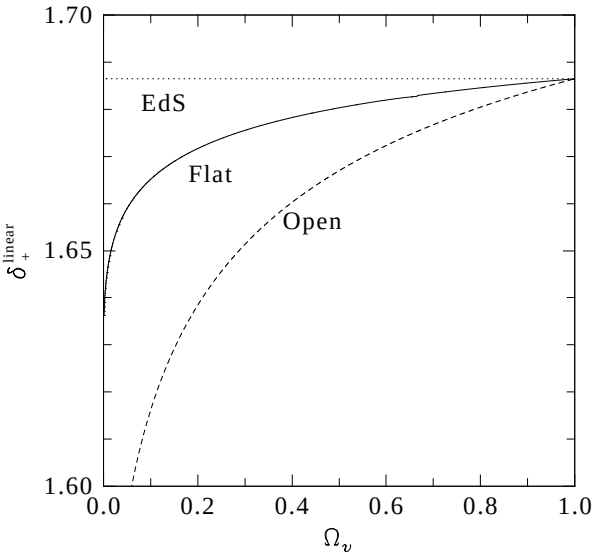

Figure A.2: The density contrast when the sphere collapses in the linear theory for three sets of cosmological parameters: ($\Omega_{m,0}$, $\Omega_{\Lambda,0}$)=(0.3, 0.7) (solid), (0.3, 0) (dashed) and (1, 0) (dotted).

Appendix B

RELATION BETWEEN THE EULER EQUATIONS AND JEANS EQUATIONS

From a microscopic point of view, both the Euler equations and the Jeans equations can be derived from the Boltzmann equation under different assumptions. In the following, we explicitly compare the two sets of equations in both Cartesian and spherical coordinates.

B.1 Cartesian Coordinates

We define the distribution function f such that $f(\boldsymbol{x}, \boldsymbol{v}, t)d^3xd^3v$ is the probability that a randomly chosen particle in the system lies in the phase space volume d^3xd^3v at position $(\boldsymbol{x}, \boldsymbol{v})$ and time t. The motion of such particles under the gravitational potential ϕ is described by the Boltzmann equation:

$$\frac{\partial f}{\partial t} + v^i \frac{\partial f}{\partial x^i} - \frac{\partial \phi}{\partial x_i}\frac{\partial f}{\partial v^i} = \left(\frac{\delta f}{\delta t}\right)_{\rm coll}, \tag{B.1}$$

where the collision term on the right hand side takes account of collisions between particles. Note that v^i $(i = 1, 2, 3)$ represents a coordinate in the phase space and should not be confused with the velocity field at the spatial point x^i. For simplicity, we assume that all particles have the same mass m in the following.

First, we consider a collisionless case with $(\delta f/\delta t)_{\rm coll} = 0$. Multiplying equation (B.1) by m and integrating it over the velocity space yield the continuity equation:

$$\frac{\partial \rho}{\partial t} + \frac{\partial(\rho \bar{v}^i)}{\partial x^i} = 0, \tag{B.2}$$

where

$$\rho(\boldsymbol{x}, t) = \int d^3v \; mf(\boldsymbol{x}, \boldsymbol{v}, t) \tag{B.3}$$

and we introduce the average over the velocity space:

$$\bar{q}(\boldsymbol{x}, t) = \frac{1}{\rho(\boldsymbol{x}, t)} \int d^3v \; mq(\boldsymbol{x}, \boldsymbol{v}, t) f(\boldsymbol{x}, \boldsymbol{v}, t) \tag{B.4}$$

for an arbitrary variable q such as v^i. Multiplying equation (B.1) by mv^j and integrating over the velocity space give the momentum equations:

$$\frac{\partial(\rho\bar{v}^i)}{\partial t} + \frac{\partial\tau_{\rm J}^{ij}}{\partial x^j} = -\rho\frac{\partial\phi}{\partial x_i}, \tag{B.5}$$

where

$$\tau_{\rm J}^{ij} = \rho\overline{v^i v^j} = \rho\sigma^{2,ij} + \rho\bar{v}^i\bar{v}^j \tag{B.6}$$

and $\sigma^{2,ij}$ is the velocity dispersion tensor. Equations (B.2) and (B.5) reduce to the Jeans equations:

$$\frac{\partial\bar{v}^i}{\partial t} + \bar{v^j}\frac{\partial\bar{v}^i}{\partial x^j} = -\frac{1}{\rho}\frac{\partial(\rho\sigma^{2,ij})}{\partial x^j} - \frac{\partial\phi}{\partial x_i} \tag{B.7}$$

Next, we consider a collisional case. Rigorous handling of the collisional term is rather complicated and simplified models are often used. A conventional one is the Bhartnagar-Gross-Krock (BGK) equation, which employs a linearized collisional term:

$$\frac{\partial f}{\partial t} + v^i\frac{\partial f}{\partial x^i} - \frac{\partial\phi}{\partial x_i}\frac{\partial f}{\partial v^i} = -\frac{f - f_0}{\tau}, \tag{B.8}$$

where τ is the relaxation time of the system considered, f_0 is the Maxwellian distribution function characterized by the local temperature $T(\boldsymbol{x}, t)$:

$$f_0(\boldsymbol{x}, \boldsymbol{v}, t) = \left[\frac{m}{2\pi k_B T(\boldsymbol{x}, t)}\right]^{3/2} \exp\left[-\frac{m(\boldsymbol{v} - \bar{\boldsymbol{v}}(\boldsymbol{x}, t))^2}{2k_B T(\boldsymbol{x}, t)}\right], \tag{B.9}$$

and k_B is the Boltzmann constant. If we assume that mean values of conservatives such as mass and momentum are the same as those in local thermal equilibrium, the collision term vanishes in the continuity and momentum equations. In local thermal equilibrium, pressure is defined from the diagonal components of σ_{ij}^2 by $p\delta_{ij} \equiv \rho\sigma_{ij}^2$ and the dispersion tensor can be written as

$$\tau_{\rm E}^{ij} = p\delta^{ij} + \rho\bar{v}^i\bar{v}^j. \tag{B.10}$$

If we replace $\tau_{\rm J}$ in equation (B.5) with $\tau_{\rm E}$ and combine them with equation (B.2), we obtain the Euler equations:

$$\frac{\partial\bar{v}^i}{\partial t} + \bar{v}^j\frac{\partial\bar{v}^i}{\partial x^j} = -\frac{1}{\rho}\frac{\partial p}{\partial x_i} - \frac{\partial\phi}{\partial x_i}. \tag{B.11}$$

The difference between the Euler and the Jeans equations resides only in the form of the dispersion tensor.

If we retain the off-diagonal components of the dispersion tensor, they can be interpreted as viscosity, and the equations reduce to the Navier-Stokes equations (Choudhuri, 1998; Chapman & Cowling, 1970).

B.2 Spherical coordinates

One can rewrite the continuity and momentum equations in the previous section in general coordinates:

$$\frac{\partial\rho}{\partial t} + \nabla_i(\rho\bar{v}^i) = 0 \tag{B.12}$$

and

$$\frac{\partial(\rho\bar{v}^i)}{\partial t} + \nabla_j \tau^{ij} = -\rho g^{ij}\nabla_j \phi, \tag{B.13}$$

by using the *covariant* derivative operator ∇_i . For spherical coordinates ($x^1 = r, x^2 = \theta, x^3 = \varphi$), non-zero components of the metric tensor g^{ij} are

$$g_{11} = 1, \quad g_{22} = r^2, \quad g_{33} = r^2 \sin^2\theta \tag{B.14}$$

and the corresponding non-zero connection coefficients are

$$\begin{aligned} &\Gamma^1_{22} = -r, \quad \Gamma^1_{33} = -r\sin^2\theta, \quad \Gamma^2_{12} = \Gamma^2_{21} = \frac{1}{r}, \\ &\Gamma^2_{33} = -\sin\theta\cos\theta, \quad \Gamma^3_{13} = \Gamma^3_{31} = \frac{1}{r}, \quad \Gamma^3_{23} = \Gamma^3_{32} = \cot\theta. \end{aligned} \tag{B.15}$$

The velocity vector is now given by $\bar{v}^i = (\bar{v}_r, \bar{v}_\theta/r, \bar{v}_\varphi/r\sin\theta)$.

In spherical coordinates, the continuity equation leads

$$\frac{\partial\rho}{\partial t} + \frac{1}{r^2}\frac{\partial(r^2\rho\bar{v}_r)}{\partial r} + \frac{1}{r\sin\theta}\frac{\partial(\sin\theta\rho\bar{v}_\theta)}{\partial\theta} + \frac{1}{r\sin\theta}\frac{\partial(\rho\bar{v}_\varphi)}{\partial\varphi} = 0. \tag{B.16}$$

Setting $\tau^{ij} = \tau^{ij}_{\mathrm{E}} = \rho\bar{v}^i\bar{v}^j + pg^{ij}$ gives the Euler equations:

$$\left[\frac{\partial}{\partial t} + \bar{v}_r\frac{\partial}{\partial r} + \frac{\bar{v}_\theta}{r}\frac{\partial}{\partial\theta} + \frac{\bar{v}_\varphi}{r\sin\theta}\frac{\partial}{\partial\varphi}\right]\bar{v}_r - \frac{\bar{v}_\theta^2 + \bar{v}_\varphi^2}{r} = -\frac{1}{\rho}\frac{\partial p}{\partial r} - \frac{\partial\phi}{\partial r} \tag{B.17}$$

$$\left[\frac{\partial}{\partial t} + \bar{v}_r\frac{\partial}{\partial r} + \frac{\bar{v}_\theta}{r}\frac{\partial}{\partial\theta} + \frac{\bar{v}_\varphi}{r\sin\theta}\frac{\partial}{\partial\varphi}\right]\bar{v}_\theta + \frac{\bar{v}_r\bar{v}_\theta - \bar{v}_\varphi^2\cot\theta}{r} = -\frac{1}{\rho r}\frac{\partial p}{\partial\theta} - \frac{1}{r}\frac{\partial\phi}{\partial\theta}, \tag{B.18}$$

$$\begin{aligned} &\left[\frac{\partial}{\partial t} + \bar{v}_r\frac{\partial}{\partial r} + \frac{\bar{v}_\theta}{r}\frac{\partial}{\partial\theta} + \frac{\bar{v}_\varphi}{r\sin\theta}\frac{\partial}{\partial\varphi}\right]\bar{v}_\varphi + \frac{\bar{v}_r\bar{v}_\varphi + \bar{v}_\theta\bar{v}_\varphi\cot\theta}{r} \\ &\qquad = -\frac{1}{\rho r\sin\theta}\frac{\partial p}{\partial\varphi} - \frac{1}{r\sin\theta}\frac{\partial\phi}{\partial\varphi}. \end{aligned} \tag{B.19}$$

On the other hand, putting $\tau^{ij} = \tau^{ij}_{\mathrm{J}} = \rho\overline{v^i v^j}$ leads to the Jeans equations:

$$\begin{aligned} &\left[\frac{\partial}{\partial t} + \bar{v}_r\frac{\partial}{\partial r} + \frac{\bar{v}_\theta}{r}\frac{\partial}{\partial\theta} + \frac{\bar{v}_\varphi}{r\sin\theta}\frac{\partial}{\partial\varphi}\right]\bar{v}_r + \frac{1}{\rho}\left[\frac{\partial(\rho\sigma^2_{rr})}{\partial r} + \frac{1}{r}\frac{\partial(\rho\sigma^2_{r\theta})}{\partial\theta} + \frac{1}{r\sin\theta}\frac{\partial(\rho\sigma^2_{r\varphi})}{\partial\varphi}\right] \\ &+ \frac{1}{r}\left(2\sigma^2_{rr} - \sigma^2_{\theta\theta} - \sigma^2_{\varphi\varphi} - \bar{v}_\theta^2 - \bar{v}_\varphi^2 + \sigma^2_{r\theta}\cot\theta\right) = -\frac{\partial\phi}{\partial r} \end{aligned} \tag{B.20}$$

$$\begin{aligned} &\left[\frac{\partial}{\partial t} + \bar{v}_r\frac{\partial}{\partial r} + \frac{\bar{v}_\theta}{r}\frac{\partial}{\partial\theta} + \frac{\bar{v}_\varphi}{r\sin\theta}\frac{\partial}{\partial\varphi}\right]\bar{v}_\theta + \frac{1}{\rho}\left[\frac{\partial(\rho\sigma^2_{r\theta})}{\partial r} + \frac{1}{r}\frac{\partial(\rho\sigma^2_{\theta\theta})}{\partial\theta} + \frac{1}{r\sin\theta}\frac{\partial(\rho\sigma^2_{\theta\varphi})}{\partial\varphi}\right] \\ &+ \frac{1}{r}\left(3\sigma^2_{r\theta} - \sigma^2_{\varphi\varphi}\cot\theta + \bar{v}_r\bar{v}_\theta - \bar{v}_\varphi^2\cot\theta + \sigma^2_{\theta\theta}\cot\theta\right) = -\frac{1}{r}\frac{\partial\phi}{\partial\theta} \end{aligned} \tag{B.21}$$

$$\begin{aligned} &\left[\frac{\partial}{\partial t} + \bar{v}_r\frac{\partial}{\partial r} + \frac{\bar{v}_\theta}{r}\frac{\partial}{\partial\theta} + \frac{\bar{v}_\varphi}{r\sin\theta}\frac{\partial}{\partial\varphi}\right]\bar{v}_\varphi + \frac{1}{\rho}\left[\frac{\partial(\rho\sigma^2_{r\varphi})}{\partial r} + \frac{1}{r}\frac{\partial(\rho\sigma^2_{\theta\varphi})}{\partial\theta} + \frac{1}{r\sin\theta}\frac{\partial(\rho\sigma^2_{\varphi\varphi})}{\partial\varphi}\right] \\ &+ \frac{1}{r}\left(3\sigma^2_{r\varphi} + \bar{v}_r\bar{v}_\varphi + \bar{v}_\theta\bar{v}_\varphi\cot\theta + 2\sigma^2_{\theta\varphi}\cot\theta\right) = -\frac{1}{r\sin\theta}\frac{\partial\phi}{\partial\varphi}. \end{aligned} \tag{B.22}$$

Appendix C

SYSTEMATIC ERRORS IN MASS ESTIMATES FOR COLLISIONLESS SYSTEMS

In a similar fashion to Section 5.1, we can compute the gravitational mass using the Jeans equations:

$$\frac{\partial \boldsymbol{v}}{\partial t} + (\boldsymbol{v}\cdot\nabla)\boldsymbol{v} = -\frac{1}{\rho_{\rm dm}}\nabla(\rho_{\rm dm}\boldsymbol{\sigma}^2) - \nabla\phi, \tag{C.1}$$

$$M_{\rm tot} = \frac{1}{4\pi G}\int_{\partial V} d\boldsymbol{S}\cdot\left[-\frac{1}{\rho_{\rm dm}}\nabla(\rho_{\rm dm}\boldsymbol{\sigma}^2) - (\boldsymbol{v}\cdot\nabla)\boldsymbol{v} - \frac{\partial \boldsymbol{v}}{\partial t}\right], \tag{C.2}$$

where $\boldsymbol{v}$ and $\boldsymbol{\sigma}^2$ are the velocity field of particles and the velocity dispersion tensor, respectively. We here represent the collisionless component by dark matter, but the same formulation is readily applicable to galaxies. We decompose the right hand side of equation (C.2) into the following terms by means of equation (B.20):

$$M_{\rm tot} = M_{\rm rand} + M_{\rm aniso} + M_{\rm rot} + M_{\rm stream} + M_{\rm cross} + M_{\rm accel}. \tag{C.3}$$

$$M_{\rm rand} = -\frac{1}{4\pi G}\int_{\partial V} dS\ \frac{1}{\rho_{\rm dm}}\frac{\partial(\rho_{\rm dm}\sigma_{rr}^2)}{\partial r}, \tag{C.4}$$

$$M_{\rm aniso} = -\frac{1}{4\pi G}\int_{\partial V} dS\ \frac{2\sigma_{rr}^2 - \sigma_{\theta\theta}^2 - \sigma_{\varphi\varphi}^2}{r}, \tag{C.5}$$

$$M_{\rm rot} = \frac{1}{4\pi G}\int_{\partial V} dS\ \frac{v_\theta^2 + v_\varphi^2}{r}, \tag{C.6}$$

$$M_{\rm stream} = -\frac{1}{4\pi G}\int_{\partial V} dS\ \left[v_r\frac{\partial v_r}{\partial r} + \frac{v_\theta}{r}\frac{\partial v_r}{\partial \theta} + \frac{v_\varphi}{r\sin\theta}\frac{\partial v_r}{\partial \varphi}\right], \tag{C.7}$$

$$M_{\rm cross} = -\frac{1}{4\pi G}\int_{\partial V} dS\ \left[\frac{1}{\rho_{\rm dm}}\frac{\partial(\rho_{\rm dm}\sigma_{r\theta}^2)}{r\partial\theta} + \frac{1}{\rho_{\rm dm}}\frac{\partial(\rho_{\rm dm}\sigma_{r\varphi}^2)}{r\sin\theta\partial\varphi} + \frac{\sigma_{r\theta}^2\cot\theta}{r}\right]. \tag{C.8}$$

$$M_{\rm accel} = -\frac{1}{4\pi G}\int_{\partial V} dS\ \frac{\partial v_r}{\partial t}. \tag{C.9}$$

Physical interpretation of each mass term is as follows. The term $M_{\rm rand}$ comes from the gradient of velocity dispersion in the r-direction and corresponds to $M_{\rm therm}$ for a collisional gas. The

meaning of $M_{\rm rot}$, $M_{\rm stream}$ and $M_{\rm accel}$ are similar to the corresponding terms for the collisional gas (Equations (5.6) to (5.8)). The terms that have no counterpart in the Euler equations are $M_{\rm aniso}$ and $M_{\rm cross}$; the former represents anisotropy of the velocity dispersion whereas the latter arises from the off-diagonal components of the velocity dispersion tenser and vanishes if velocities of different directions are uncorrelated.

We apply the above formulation to dark matter particles in the simulated cluster described in Section 4.1 to quantify intrinsic systematic errors of the mass estimation using collisionless particles. Note that one can apply the same method to galaxies but with much larger impact of statistical errors. Therefore, we do not do so here because we are interested in intrinsic systematic errors independent of observational complexities. Each term is computed in a similar manner to the case of collisional gas described in Section 5.1.

Figure C.1 shows that the difference between $M_{\rm tot}$ and $M_{\rm rand}$ increases toward the outer envelope mainly owing to the presence of $M_{\rm aniso}$. This is because the relaxation timescale of collisionless particles is much longer than that of the collisional gas. Once this term is subtracted, $M_{\rm tot} - M_{\rm rand} - M_{\rm aniso}$ closely matches $M_{\rm accel}$ whose absolute value is limited to within $\sim 0.3 M_{\rm tot}$. The amount of $M_{\rm accel}$ is similar to that for the collisional gas (Figure 5.1). The other mass terms such as $M_{\rm cross}$ are less important.

The above results imply that proper account of velocity anisotropies is essential for the mass reconstruction using a collisionless component. We stress that $M_{\rm aniso}$ is irrelevant to the collisional fluid as long as local thermal equilibrium is established (Appendix B).

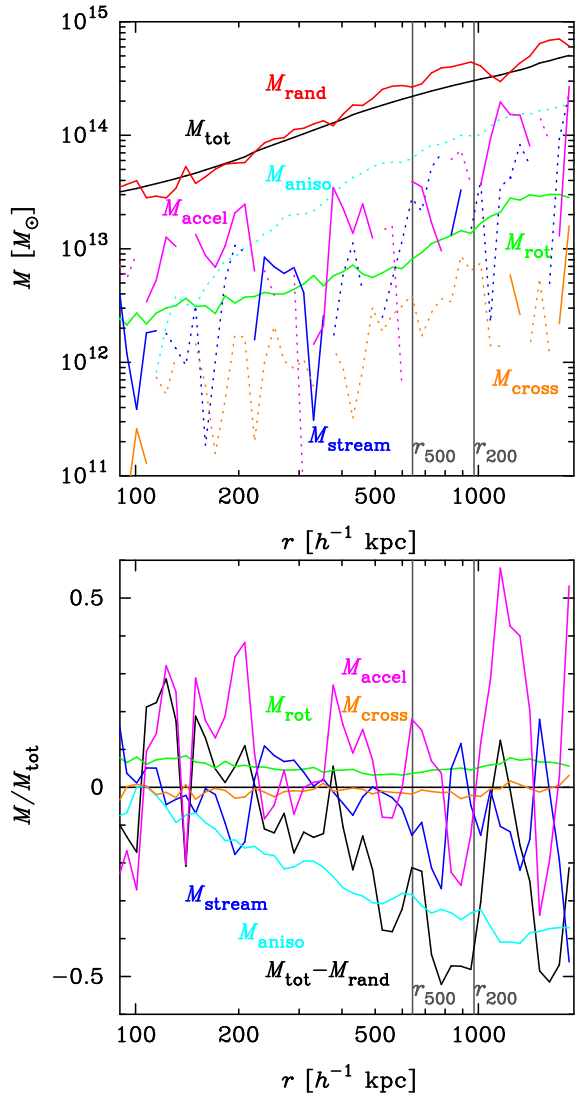

Figure C.1: The *effective* mass terms in Equation (C.3) for the dark matter in the simulated cluster are shown in the left panel: $M_{\rm tot}$ (black), $M_{\rm rand}$ (red), $M_{\rm rot}$ (green), $M_{\rm stream}$ (blue), $M_{\rm aniso}$ (cyan), $M_{\rm cross}$ (orange) and $M_{\rm accel}$ (magenta). Here $M_{\rm accel}$ is calculated by $M_{\rm accel} = M_{\rm tot} - M_{\rm therm} - M_{\rm rot} - M_{\rm stream}$. Dotted line means that its sign is inverted. Ratios of mass terms to $M_{\rm tot}$ are shown in the right panel; The black line shows $(M_{\rm tot} - M_{\rm rand})/M_{\rm tot}$ and other mass terms are colored in the same colors as the left panel.

References

Allen, S. W., Evrard, A. E., & Mantz, A. B. 2011, ARAA, 49, 409, Cosmological Parameters from Observations of Galaxy Clusters

Biffi, V., Dolag, K., & Böhringer, H. 2011, MNRAS, 413, 573, Velocity structure diagnostics of simulated galaxy clusters

Binney, J. & Tremaine, S. 2008, Galactic Dynamics: Second Edition (Princeton University Press)

Bryan, G. L. 1999, Comput. Sci. Eng., Vol. 1, No. 2, p. 46 - 53, 1, 46, Fluids in the universe: adaptive mesh refinement in cosmology.

Bryan, G. L. & Norman, M. L. A Hybrid AMR Application for Cosmology and Astrophysics, ed. N. P. C. S. B. Baden, IMA Volumes on Structured Adaptive Mesh Refinement No. 117, 165

Cen, R. 2012, ApJ, 748, 121, The Nature of Damped Lyα Systems and Their Hosts in the Standard Cold Dark Matter Universe

Cen, R., Kang, H., Ostriker, J. P., & Ryu, D. 1995, ApJ, 451, 436, Background X-Ray Emission from Hot Gas in CDM and CDM+ Lambda Universes: Spectral Signatures

Cen, R., Nagamine, K., & Ostriker, J. P. 2005, ApJ, 635, 86, Quantitative Signatures of Galactic Superwinds on Lyα Clouds and Metal-Line Systems

Cen, R. & Ostriker, J. P. 1992, ApJL, 399, L113, Galaxy formation and physical bias

Chapman, S. & Cowling, T. G. 1970, The mathematical theory of non-uniform gases. an account of the kinetic theory of viscosity, thermal conduction and diffusion in gases (Cambridge University Press)

Choudhuri, A. R. 1998, The physics of fluids and plasmas : an introduction for astrophysicists (Cambridge University Press)

Dolag, K., Borgani, S., Murante, G., & Springel, V. 2009, MNRAS, 399, 497, Substructures in hydrodynamical cluster simulations

Dolag, K., Meneghetti, M., Moscardini, L., Rasia, E., & Bonaldi, A. 2006, MNRAS, 370, 656, Simulating the physical properties of dark matter and gas inside the cosmic web

Fang, T., Humphrey, P., & Buote, D. 2009, ApJ, 691, 1648, Rotation and Turbulence of the Hot Intracluster Medium in Galaxy Clusters

Haardt, F. & Madau, P. 1996, ApJ, 461, 20, Radiative Transfer in a Clumpy Universe. II. The Ultraviolet Extragalactic Background

Hinshaw, G., Larson, D., Komatsu, E., Spergel, D. N., Bennett, C. L., Dunkley, J., Nolta, M. R., Halpern, M., Hill, R. S., Odegard, N., Page, L., Smith, K. M., Weiland, J. L., Gold, B., Jarosik, N., Kogut, A., Limon, M., Meyer, S. S., Tucker, G. S., Wollack, E., & Wright, E. L. 2012, ArXiv e-prints, Nine-Year Wilkinson Microwave Anisotropy Probe (WMAP) Observations: Cosmological Parameter Results

Joung, M. R., Cen, R., & Bryan, G. L. 2009, ApJL, 692, L1, Galaxy Size Problem at z = 3: Simulated Galaxies are too Small

Komatsu, E., Smith, K. M., Dunkley, J., Bennett, C. L., Gold, B., Hinshaw, G., Jarosik, N., Larson, D., Nolta, M. R., Page, L., Spergel, D. N., Halpern, M., Hill, R. S., Kogut, A., Limon, M., Meyer, S. S., Odegard, N., Tucker, G. S., Weiland, J. L., Wollack, E., & Wright, E. L. 2011, ApJS, 192, 18, Seven-year Wilkinson Microwave Anisotropy Probe (WMAP) Observations: Cosmological Interpretation

Laganá, T. F., de Souza, R. S., & Keller, G. R. 2010, A&A, 510, A76, On the influence of non-thermal pressure on the mass determination of galaxy clusters

Lau, E. T., Kravtsov, A. V., & Nagai, D. 2009, ApJ, 705, 1129, Residual Gas Motions in the Intracluster Medium and Bias in Hydrostatic Measurements of Mass Profiles of Clusters

Mahdavi, A., Hoekstra, H., Babul, A., & Henry, J. P. 2008, MNRAS, 384, 1567, Evidence for non-hydrostatic gas from the cluster X-ray to lensing mass ratio

Mazzotta, P., Rasia, E., Moscardini, L., & Tormen, G. 2004, MNRAS, 354, 10, Comparing the temperatures of galaxy clusters from hydrodynamical N-body simulations to Chandra and XMM-Newton observations

Mo, H., van den Bosch, F. C., & White, S. 2010, Galaxy Formation and Evolution

Nagai, D., Vikhlinin, A., & Kravtsov, A. V. 2007, ApJ, 655, 98, Testing X-Ray Measurements of Galaxy Clusters with Cosmological Simulations

Nakamura, T. T. & Suto, Y. 1997, Progress of Theoretical Physics, 97, 49, Strong Gravitational Lensing and Velocity Function as Tools to Probe Cosmological Parameters — Current Constraints and Future Predictions —

O'Shea, B. W., Bryan, G., Bordner, J., Norman, M. L., Abel, T., Harkness, R., & Kritsuk, A. 2004, ArXiv Astrophysics e-prints, Introducing Enzo, an AMR Cosmology Application

Press, W. H. & Schechter, P. 1974, ApJ, 187, 425, Formation of Galaxies and Clusters of Galaxies by Self-Similar Gravitational Condensation

Rasia, E., Tormen, G., & Moscardini, L. 2004, MNRAS, 351, 237, A dynamical model for the distribution of dark matter and gas in galaxy clusters

Springel, V. & Hernquist, L. 2003, MNRAS, 339, 289, Cosmological smoothed particle hydrodynamics simulations: a hybrid multiphase model for star formation

Springel, V., White, M., & Hernquist, L. 2001, ApJ, 549, 681, Hydrodynamic Simulations of the Sunyaev-Zeldovich Effect(s)

Springel, V., White, S. D. M., Jenkins, A., Frenk, C. S., Yoshida, N., Gao, L., Navarro, J., Thacker, R., Croton, D., Helly, J., Peacock, J. A., Cole, S., Thomas, P., Couchman, H., Evrard, A., Colberg, J., & Pearce, F. 2005, Nature, 435, 629, Simulations of the formation, evolution and clustering of galaxies and quasars

Vikhlinin, A., Kravtsov, A., Forman, W., Jones, C., Markevitch, M., Murray, S. S., & Van Speybroeck, L. 2006, ApJ, 640, 691, Chandra Sample of Nearby Relaxed Galaxy Clusters: Mass, Gas Fraction, and Mass-Temperature Relation

Yoshida, N., Sheth, R. K., & Diaferio, A. 2001, MNRAS, 328, 669, Non-Gaussian cosmic microwave background temperature fluctuations from peculiar velocities of clusters

Zhang, Y.-Y., Finoguenov, A., Böhringer, H., Kneib, J.-P., Smith, G. P., Kneissl, R., Okabe, N., & Dahle, H. 2008, A&A, 482, 451, LoCuSS: comparison of observed X-ray and lensing galaxy cluster scaling relations with simulations

ACKNOWLEDGMENT

First I thank Yasushi Suto, my supervisor, for his continuing encouragement and support. encouragement and support. I would like to acknowledge my collaborators: Shin Sasaki, Tetsu Kitayama, Hajime Kawahara for fruitful discussions, and Renyue Cen and Klaus Dolag for providing me with simulation data and their helpful advice. I appreciate my enjoyable college academic life with Atsushi Taruya, Teruyuki Hirano, Yuka Fujii, Toshiya Namikawa, Kensuke Fukunaga, Toshiya Kashiwagi, Akira Oka, Yuxin Xue and Kento Masuda. Finally I thank my family for everything.